Time-Integrated and Time-Resolved Optical Studies of InGaN Quantum Dots

James W. Robinson



The Clarendon Laboratory
University of Oxford

Thesis submitted for the Degree of
Doctor of Philosophy

The Queen's College

Hilary Term 2005

Time-Integrated and Time-Resolved Optical Studies of InGaN Quantum Dots

James W. Robinson
The Queen's College, University of Oxford
Hilary Term 2005
Thesis submitted for the Degree of Doctor of Philosophy

Abstract

The construction of a high-resolution optical microscope system for micro-photoluminescence (μ-PL) spectroscopy is described, and a range of time-integrated and time-resolved experimental work on single InGaN quantum dots (QDs) is presented.

Time-integrated measurements demonstrate the existence of InGaN QDs in three different samples via the presence of sharp exciton recombination lines in the μ-PL spectra. The narrowest peaks display a linewidth Γ of $\sim$230 μeV, implying a decoherence time $T_2 \geq$5.7 ps.

Time-resolved measurements on exciton recombination lines from single self-assembled InGaN QDs reveal typical lifetimes of $\sim$2.0 ns (which decrease with increasing temperature), while typical lifetimes for excitons in single selectively-grown micropyramidal InGaN QDs are found to be $\sim$0.4 ns. The shorter exciton recombination lifetime in selectively-grown QDs is believed to be due to a stronger coupling of these QDs to the underlying quantum well.

Temporal fluctuations (on a timescale of seconds) in the energy, intensity and FWHM of μ-PL peaks arising from the recombination of excitons in single self-assembled InGaN QDs are observed. These are attributed to transient Stark shifts induced by a fluctuating local charge distribution as carriers become trapped in defect states in the vicinity of the QDs.

Time-integrated power-dependent measurements are used to demonstrate the presence of biexciton states in single self-assembled InGaN QDs. The exciton–biexciton energy splitting is found to be $\sim$41 meV, in agreement with values predicted by theoretical calculations. Time-resolved studies of the biexciton and exciton decay curves reveal a coupling as the exciton population is refilled by biexciton decays. The biexciton lifetime is found to be $\sim$1.4 ns, compared to an exciton lifetime of $\sim$1.0 ns.

Lateral electric fields are applied to a single self-assembled InGaN QD using aluminium electrodes lithographically defined on the sample surface. Application of fields of the order of $\sim$0.17 MVcm^{-1} is found to cause both a red-shift and a reduction in the intensity of the exciton recombination peak in the μ-PL spectrum.

Acknowledgements

'The works of the Lord are great,
sought out of all them that have pleasure therein.' (Psalm 111)

I would like to express my gratitude to:

- Prof Roger Cowley and Prof Robin Nicholas for extending to me the facilities of the Clarendon Laboratory.
- Dr Robert Taylor for supervising this work, for taking the time to teach me about experimental Optics, and for his valuable advice, constant encouragement, and unwaning enthusiasm for Physics.
- Dr Jonathan Smith for showing me the ropes.
- Dr James Rice for experimental assistance.
- Prof Andrew Briggs for help with writing papers.
- Prof Andrew Turberfield for useful discussions about various aspects of Physics.
- Prof Yasuhiko Arakawa and Dr Robert Martin for providing InGaN quantum dot samples.
- Dr Rachel Oliver for providing InGaN quantum dot samples and for expert advice on growth.
- Mr Anas Jarjour for enthusiastic help in machining, alignment, experiments and data analysis.
- Mr Kwan Hee Lee for technical assistance and for his Australian sense of humour.
- Mr Jong Ho Na for interesting discussions regarding GaN nanocolumns.
- Mr Robert Harris for his patience in teaching me to use a lathe and a milling machine, and for sorting out my mistakes.
- Mr Nigel Parker for providing liquid helium, all too often at short notice.
- My family for their encouragement.
- EPSRC and the LINK Project for financial support.

Publications

- J. W. Robinson, J. H. Rice, A. Jarjour, J. D. Smith, R. A. Taylor, R. A. Oliver, G. A. D. Briggs, M. J. Kappers, C. J. Humphreys and Y. Arakawa, 'Time-resolved dynamics in single InGaN quantum dots', *Appl. Phys. Lett.* **83**, 2674 (2003).

- J. W. Robinson, J. H. Rice, A. Jarjour, J. D. Smith, R. A. Taylor, R. A. Oliver, G. A. D. Briggs, M. J. Kappers, C. J. Humphreys, S. Yasin and Y. Arakawa, 'Time-integrated and time-resolved photoluminescence studies of InGaN quantum dots', *Phys. Stat. Sol. (c)* **1**, 568 (2004).

- J. H. Rice, J. W. Robinson, A. Jarjour, R. A. Taylor, R. A. Oliver, G. A. D. Briggs, M. J. Kappers and C. J. Humphreys, 'Temporal variation in photoluminescence from single InGaN quantum dots', *Appl. Phys. Lett.* **84**, 4110 (2004).

- R. A. Taylor, J. W. Robinson, J. H. Rice, A. Jarjour, J. D. Smith, R. A. Oliver, G. A. D. Briggs, M. J. Kappers, C. J. Humphreys and Y. Arakawa, 'Dynamics of single InGaN quantum dots', *Physica E* **21**, 285 (2004).

- J. H. Rice, R. A. Oliver, J. W. Robinson, J. D. Smith, R. A. Taylor, G. A. D. Briggs, M. J. Kappers, C. J. Humphreys and S. Yasin, 'InGaN quantum dots grown by MOVPE via a droplet epitaxy route', *Physica E* **21**, 546 (2004).

- J. H. Rice, J. W. Robinson, A. Jarjour, J. D. Smith, R. A. Taylor, R. A. Oliver, G. A. D. Briggs, M. J. Kappers and C. J. Humphreys, 'Studies of exciton recombination and dephasing in single InGaN QDs using photoluminescence spectroscopy', *IEEE Trans. Nanotech.* **3**, 343 (2004).

- P. R. Edwards, R. W. Martin, I. M. Watson, C. Liu, R. A. Taylor, J. H. Rice, J. H. Na, J. W. Robinson and J. D. Smith, 'Quantum dot emission from site-controlled InGaN/GaN micropyramidal arrays', *Appl. Phys. Lett.* **85**, 4281 (2004).

- J. H. Na, R. A. Taylor, J. H. Rice, J. W. Robinson, K. H. Lee, Y. S. Park, C. M. Park and T. W. Kang, 'Time-resolved and time-integrated photoluminescence studies of coupled asymmetric GaN quantum discs embedded in AlGaN barriers', *Appl. Phys. Lett.* **86**, 083109 (2005).

- J. H. Na, R. A. Taylor, J. H. Rice, J. W. Robinson, K. H. Lee, Y. S. Park, C. M. Park and T. W. Kang, 'Two-dimensional exciton behavior in GaN nanocolumns grown by molecular beam epitaxy', *Appl. Phys. Lett.* **86**, 123102 (2005).

- R. W. Martin, P. R. Edwards, R. A. Taylor, J. H. Rice, J. H. Na, J. W. Robinson, J. D. Smith, C. Liu and I. M. Watson, 'Luminescence properties of isolated InGaN/GaN quantum dots', *Phys. Stat. Sol. (a)* **202**, 372 (2005).

- J. W. Robinson, J. H. Rice, K. H. Lee, J. H. Na, R. A. Taylor, D. G. Hasko, R. A. Oliver, M. J. Kappers, C. J. Humphreys and G. A. D. Briggs, 'Quantum-confined Stark effect in a single InGaN quantum dot under a lateral electric field', *Appl. Phys. Lett.* **86**, 213103 (2005).

- R. A. Taylor, J. W. Robinson, J. H. Rice, K. H. Lee, A. Jarjour, J. H. Na, S. Yasin, R. A. Oliver, M. J. Kappers, C. J. Humphreys, G. A. D. Briggs, D. P. Williams, E. P. O'Reilly, A. D. Andreev and Y. Arakawa, 'Time-resolved dynamics in single InGaN quantum dots', *Proc. SPIE* **5725**, 297 (2005).

- D. P. Williams, A. D. Andreev, E. P. O'Reilly, J. H. Rice, J. W. Robinson, A. Jarjour, J. D. Smith, R. A. Taylor, G. A. D. Briggs, Y. Arakawa and S. Yasin, 'Theoretical and experimental investigation of biexcitons and charged excitons in InGaN single quantum dots', *Proc. 27th Int. Conf. Phys. Semicond.*, 695 (2005).

- R. A. Taylor, J. H. Rice, J. H. Na, J. W. Robinson, 'Quantum dot emission from selectively-grown InGaN/GaN micropyramid arrays', *Proc. 27th Int. Conf. Phys. Semicond.*, 865 (2005).

- J. H. Rice, J. W. Robinson, J. H. Na, K. H. Lee, R. A. Taylor, D. P. Williams, E. P. O'Reilly, A. D. Andreev, Y. Arakawa and S. Yasin, 'Biexciton and exciton dynamics in single InGaN quantum dots', *Nanotech.* **16**, 1477 (2005).

- J. H. Rice, M. J. Holmes, J. W. Robinson, R. A. Taylor, D. P. Williams, E. P. O'Reilly, A. D. Andreev and Y. Arakawa, 'Exciton, biexciton, charged exciton complexes in single InGaN quantum dots', submitted to *Appl. Phys. Lett.*

Presentations

Oral presentations by the author:

- J. W. Robinson, J. H. Rice, R. A. Oliver, J. D. Smith, R. A. Taylor, A. Jarjour, M. Kappers, S. Yasin, C. J. Humphreys and G. A. D. Briggs, 'InGaN quantum dots grown by MOVPE employing a post-growth nitrogen anneal', EQUONT-2, Tolédo, Spain (June 2003).
- J. W. Robinson, J. H. Rice, A. Jarjour, J. D. Smith, R. A. Taylor, R. A. Oliver, Y. Arakawa, G. A. D. Briggs and C. J. Humphreys, 'Time-resolved spectroscopy in single InGaN quantum dots', Rank Prize Funds Conference on Optoelectronic Applications of Quantum Dots and Nanoparticles, Grasmere, UK (November 2003).

Other oral presentations:

- J. H. Rice, J. W. Robinson, A. Jarjour, J. D. Smith, R. A. Taylor, R. A. Oliver, G. A. D. Briggs, M. J. Kappers and C. J. Humphreys, 'PL studies of a single InGaN QD', International Workshop on Quantum Dots for Quantum Computing and Classical Size Effect Circuits, Notre Dame, USA (August 2003).
- J. H. Rice, R. A. Oliver, J. W. Robinson, J. D. Smith, R. A. Taylor, M. J. Kappers, S. Yasin, C. J. Humphreys and G. A. D. Briggs, 'InGaN quantum dots grown by MOVPE employing a post-growth nitrogen anneal', MSS11, Nara, Japan (July 2003).
- A. Jarjour, R. A. Taylor, J. W. Robinson, J. H. Rice, J. D. Smith, R. A. Oliver, G. A. D. Briggs, M. J. Kappers and C. J. Humphreys, 'Radiative lifetime measurements on an InGaN single quantum dot by time-resolved photoluminescence', EQUONT-2, Tolédo, Spain (June 2003).

Poster presentations by the author:

- J. W. Robinson, J. H. Rice, A. Jarjour, R. A. Oliver, M. J. Kappers, R. A. Taylor, Y. Arakawa, G. A. D. Briggs and C. J. Humphreys, 'Dynamics of single InGaN QDs', OECS-8, Lecce, Italy (September 2003).

Other poster presentations:

- R. A. Taylor, J. W. Robinson, A. Jarjour, R. A. Oliver, J. H. Rice, J. D. Smith, M. J. Kappers, C. J. Humphreys, G. A. D. Briggs and Y. Arakawa, 'Time-resolved dynamics of single InGaN quantum dots', MSS11, Nara, Japan (July 2003).

- J. H. Rice, J. W. Robinson, A. Jarjour, J. D. Smith, R. A. Taylor, R. A. Oliver, G. A. D. Briggs, M. J. Kappers and C. J. Humphreys, 'PL studies of a single InGaN QD', 4th European QIPC Workshop, Oxford, UK (July 2003).

- D. P. Williams, A. D. Andreev, E. P. O'Reilly, J. H. Rice, J. W. Robinson, A. Jarjour, J. D. Smith, R. A. Taylor, G. A. D. Briggs and Y. Arakawa, 'Theoretical and experimental investigation of biexcitons and charged excitons in InGaN single quantum dots', ICPS-27, Flagstaff, USA (July 2004).

- R. A. Taylor, J. H. Rice, J. H. Na, J. W. Robinson, P. R. Edwards, R. W. Martin, I. M. Watson and C. Liu, 'Quantum dot emission from selectively-grown InGaN/GaN micropyramid arrays', ICPS-27, Flagstaff, USA (July 2004).

to my parents

Contents

1 Introduction **1**

1.1 Excitons in InGaN quantum dots 1

1.2 Thesis layout 3

2 Physics of nitride semiconductors and quantum dots **7**

2.1 Physics of nitride semiconductors 7

2.1.1 GaN 7

2.1.2 InN 9

2.1.3 InGaN 10

2.2 Quantum dots 11

2.2.1 Basic properties of quantum dots 11

2.2.2 Excitons in quantum dots 12

2.2.3 Properties of InGaN quantum dots 13

2.3 Fabrication of InGaN quantum dots 18

2.3.1 Introduction to growth 18

2.3.2 Introduction to growth of InGaN quantum dots by self-assembly . . . 19

2.3.3 Sample A: Self-assembled InGaN quantum dots grown by MOCVD . 21

2.3.4 Sample B: Self-assembled InGaN quantum dots grown by MOCVD with a post-growth nitrogen anneal 22

2.3.5 Introduction to selective growth of InGaN QDs 24

2.3.6 Sample C: Selectively-grown InGaN quantum dots 27

2.4 Summary and conclusion 28

3 Experimental development and techniques 35

3.1 Generation of laser light 35

3.1.1 Introduction 35

3.1.2 Continuous-wave laser source 36

3.1.3 Principles of ultrafast pulse generation 36

3.1.4 Ultrafast pulsed laser sources 39

3.1.5 Frequency upconversion 41

3.1.6 Ultrafast harmonic generation 44

3.2 Micro-photoluminescence spectroscopy 45

3.2.1 Introduction 45

3.2.2 Early micro-photoluminescence measurements of single quantum dots 47

3.2.3 Sample masking 48

3.2.4 Commercial *Renishaw* micro-photoluminescence system 48

3.2.5 High-resolution micro-photoluminescence system 50

3.3 Cryogenic apparatus 54

3.4 Spectrometers 57

3.5 CCD and computerized data acquisition 59

3.6 Time-correlated single photon counting 62

3.6.1 Importance of time-resolved measurements 62

3.6.2 Principle of time-correlated single photon counting 62

3.6.3 Apparatus for time-correlated single photon counting 64

3.7 Summary and conclusion 67

4 Theoretical motivation: quantum information processing 71

4.1 Introduction 71

4.2 The classical bit versus the quantum bit 72

4.3 The Bloch sphere single-qubit visualization 73

4.4 Potential advantages of quantum information processing 75

4.5 Requirements for the physical implementation of quantum information processing 77

4.5.1 Well-characterized qubits and scalability 77

4.5.2 Ability to prepare fiducial initial states 78

4.5.3 Long decoherence times 79

4.5.4 A 'universal' set of quantum gates 80

4.5.5 A qubit-specific measurement capability 80

4.6 Quantum error correction 81

4.7 Practical realizations of quantum information processing 84

4.7.1 Nuclear magnetic resonance schemes 84

4.7.2 Ion-trap schemes 86

4.7.3 Other schemes 87

4.8 Quantum information processing using quantum dots 87

4.8.1 Conventional approaches 87

4.8.2 Experimental realization of a quantum-dot-based quantum logic gate 89

4.8.3 Global addressing 91

4.8.4 Approaches based on nitride quantum dots 92

4.9 Summary and conclusion 96

5 Self-assembled InGaN quantum dots **101**

5.1 Preliminary measurements 101

5.2 Time-resolved measurements . . . 103
5.2.1 Sample A . . . 103
5.2.2 Sample B . . . 108
5.3 Linewidth measurements . . . 112
5.4 Spectral diffusion measurements . . . 115
5.4.1 Introduction . . . 115
5.4.2 Data acquisition . . . 116
5.4.3 Computerized data analysis . . . 117
5.4.4 Measurements and discussion . . . 119
5.5 Summary and conclusion . . . 127

6 Selectively-grown InGaN quantum dots 133

6.1 Introduction . . . 133
6.2 Cathodoluminescence hyper-spectral imaging . . . 133
6.2.1 Introduction to cathodoluminescence and hyper-spectral imaging . . . 133
6.2.2 Measurements using cathodoluminescence hyper-spectral imaging . . . 135
6.3 Micro-photoluminescence spectroscopy . . . 138
6.3.1 Introduction . . . 138
6.3.2 Time-integrated measurements . . . 139
6.3.3 Time-resolved measurements . . . 141
6.4 Summary and conclusion . . . 142

7 Exciton complexes in InGaN quantum dots 147

7.1 Introduction . . . 147
7.2 Exciton complexes in single nitride quantum dots . . . 148

7.2.1 Introduction . . . 148
7.2.2 Theoretical calculations of exciton complex recombination energies . . 148
7.2.3 Time-integrated studies of exciton complexes in a single InGaN quantum dot . . . 150
7.3 Time-resolved studies of exciton complexes in a single InGaN quantum dot . 153
7.3.1 Introduction . . . 153
7.3.2 Identification of exciton and biexciton recombination lines . . . 153
7.3.3 Time-resolved exciton and biexciton measurements . . . 156
7.4 Summary and conclusion . . . 160

8 Electric field measurements **164**

8.1 Introduction . . . 164
8.2 Previous work on electric fields . . . 166
8.3 Sample preparation and estimate of field strength . . . 166
8.4 Preliminary work . . . 168
8.5 Detailed analysis . . . 172
8.6 Summary and conclusion . . . 176

9 Conclusion and suggestions for further research **180**

9.1 Implications for quantum information processing . . . 180
9.2 Further research . . . 182
9.2.1 Quantum correlation spectroscopy . . . 182
9.2.2 Principles of coherent control . . . 186
9.2.3 Experimental implementation of coherent control . . . 187

A First Matlab programme **195**

B Second Matlab programme **199**

Chapter 1

Introduction

1.1 Excitons in InGaN quantum dots

Since the mid 1990s, gallium nitride (GaN) has moved from relative obscurity to centre stage in the world of semiconductor physics. In 1994, Shuji Nakamura used GaN to demonstrate the first successful blue light-emitting diode (LED), revolutionizing LED-based display technology (1).

Considerable research effort over the last decade has brought a much deeper understanding of the properties of bulk GaN, and of the closely-related ternary semiconductor indium gallium nitride (InGaN). The growth and optical properties of GaN and InGaN are now relatively well understood. However, one area in which much work remains to be done is the fabrication and optical characterization of GaN- and InGaN-based nanostructures, including quantum dots (QDs).

An understanding of InGaN QDs is important because the properties of these nanoscale structures differ considerably from those of bulk InGaN. Three-dimensional confinement of electrons and holes leads to markedly different electronic and optical properties which may

offer significant advantages in many applications. For example, the incorporation of InGaN QDs into device active layers in InGaN laser diodes has the potential to enormously improve performance.

Previous work on InGaN QDs has tended to focus on the properties of large *ensembles* of these nanostructures, and few measurements have been made on single InGaN QDs. This is unfortunate since a range of applications has been proposed for single InGaN QDs, including their use as single photon sources and even as a means of embodying quantum bits ('qubits') in quantum information processing (QIP).

The experiments described in this thesis have involved the investigation of fundamental electronic and optical processes in single InGaN QDs. The research has focused on bound structures known as 'excitons' which form when an electron and a hole become trapped in a QD. When an exciton decays through the recombination of the electron and hole, it emits light which can be measured.

Time-integrated micro-photoluminescence (μ-PL) measurements have been used to provide an insight into time-averaged exciton behaviour. By monitoring the PL emitted from very small areas, it has been possible to study excitons in single QDs. The dependence of the exciton recombination μ-PL peak on excitation power density and temperature has been investigated. Further measurements have shown temporal fluctuations in the energy, intensity and full width at half maximum (FWHM) of the μ-PL peak as a result of a fluctuating local charge distribution. This has important consequences for the use of InGaN QDs in various applications.

Time-resolved μ-PL measurements using ultrafast pulses from mode-locked lasers have per-

mitted investigation of exciton recombination behaviour on extremely short timescales. It has been possible to measure the radiative recombination lifetimes of excitons in single InGaN QDs grown via various techniques. Finding values for the lifetime is an important first step in the practical use of single InGaN QDs. It has also been possible to study the dynamics of exciton complexes (made up of several trapped electrons and holes), and to investigate the effect of applying an external electric field to a single QD.

1.2 Thesis layout

Chapter 2 discusses the basic physics of the semiconductors GaN, InN and InGaN. The nature of the wurtzite crystal structure is described, and the concept of the 'built-in' piezoelectric field is introduced. The basic properties of QDs are explained, including carrier confinement, exciton formation and the creation of various exciton complexes. Finally, the growth of InGaN QDs is discussed, both by self-assembly and by selective growth. The growth methodologies for the three samples studied in this thesis are explained in detail.

Descriptions of the experimental apparatus which was used are presented in **Chapter 3**. The laser light sources are described, both the continuous-wave He-Cd laser and the mode-locked Ti:Sapphire lasers. The principles of ultrafast pulse generation (via mode-locking) and frequency upconversion are outlined. The basic concept of μ-PL is introduced, and the two μ-PL systems which were used in this work are described in detail. The Chapter then discusses the liquid-helium cryostat, the three spectrometers and the CCD detector with its computerized control system. Finally, the principle of operation of the time-correlated single photon counting system, used for time-resolved measurements, is explained.

The possibility of using InGaN QDs in a quantum computer provides an important part of the motivation for this work, and **Chapter 4** is an entirely theoretical review of QIP. This Chapter introduces the concept of the qubit, explains the potential advantages of QIP over classical information processing, and looks at a range of physical requirements which must be satisfied by a working quantum computer. Quantum error correction and quantum fault-tolerant computation are discussed, and a number of experimental approaches to realizing QIP are outlined. Finally, various QD-based QIP schemes are considered, including proposed schemes which make use of InGaN QDs.

Chapter 5 describes experimental work on single self-assembled InGaN QDs. First, time-integrated μ-PL measurements which unambiguously demonstrate the presence of InGaN QDs via the existence of sharp peaks in the PL spectra are discussed. Then time-resolved μ-PL measurements are presented, showing the surprising result that exciton decay follows a mono-exponential curve. Values are found for the exciton radiative lifetime, the first time that such measurements have been made. The temperature dependence of the lifetime is investigated. The Chapter then discusses random temporal fluctuations observed in the energy, intensity and FWHM of exciton recombination peaks in the InGaN QD system. This is the first time that this so-called spectral diffusion has been seen in InGaN QDs, and the effect is attributed to the presence of a randomly-fluctuating charge distribution in the vicinity of the QDs. The work presented in Chapter 5 was published in (2) and (3).

Chapter 6 presents experimental work on single selectively-grown micropyramidal InGaN QDs. First, measurements made by co-workers at the University of Strathclyde using cathodoluminescence spectroscopy are described. Then data from our own μ-PL measurements is presented. Time-integrated μ-PL spectroscopy on single micropyramidal InGaN

QDs reveals for the first time the presence of sharp lines in the PL, indicative of strongly-confined carriers. Time-resolved measurements provide the first value for the exciton radiative lifetime in this system. The measured lifetime is found to be much shorter than that observed in self-assembled QDs, and this is believed to be due to the stronger coupling of QDs to the underlying quantum well in the micropyramidal QD system. The work presented in Chapter 6 was published in (4).

In **Chapter 7**, μ-PL measurements on exciton complexes in selectively-grown InGaN QDs are described. Time-integrated work by co-workers unambiguously demonstrating the presence of exciton, biexciton and charged exciton states is briefly discussed. Then data from our own μ-PL measurements is presented. A sharp peak in the PL spectrum resulting from recombination of a biexciton state is observed. The observed energy separation between the biexciton recombination line and the exciton recombination line is in good agreement with results from theoretical calculations by co-workers. Time-resolved measurements allow exciton and biexciton lifetimes to be deduced, and show a clear coupling between exciton and biexciton decay, as previously observed in QDs in other materials systems. The work presented in Chapter 7 was published in (5) and (6).

Chapter 8 deals with the effect of the application of an external electric field to a single InGaN QD. Preparation of electrical contacts on the sample surface by co-workers is briefly discussed. Then time-integrated μ-PL measurements showing the effect of an external electric field upon an exciton recombination peak are presented. The peak is found to red-shift and decline in intensity as the strength of the applied electric field is increased. The work presented in Chapter 8 was published in (7).

References

[1] S. Nakamura and G. Fasol, 'The Blue Laser Diode', Springer-Verlag (1997).

[2] J. W. Robinson, J. H. Rice, A. Jarjour, J. D. Smith, R. A. Taylor, R. A. Oliver, G. A. D. Briggs, M. J. Kappers, C. J. Humphreys and Y. Arakawa, *Appl. Phys. Lett.* **83**, 2674 (2003).

[3] J. H. Rice, J. W. Robinson, A. Jarjour, R. A. Taylor, R. A. Oliver, G. A. D. Briggs, M. J. Kappers and C. J. Humphreys, *Appl. Phys. Lett.* **84**, 4110 (2004).

[4] P. R. Edwards, R. W. Martin, I. M. Watson, C. Liu, R. A. Taylor, J. H. Rice, J. H. Na, J. W. Robinson and J. D. Smith, *Appl. Phys. Lett.* **85**, 4281 (2004).

[5] J. H. Rice, M. J. Holmes, J. W. Robinson, R. A. Taylor, D. P. Williams, E. P. O'Reilly, A. D. Andreev and Y. Arakawa, submitted to *Appl. Phys. Lett.*

[6] J. H. Rice, J. W. Robinson, J. H. Na, K. H. Lee, R. A. Taylor, D. P. Williams, E. P. O'Reilly, A. D. Andreev, Y. Arakawa and S. Yasin, submitted to *Nanotech.*

[7] J. W. Robinson, J. H. Rice, K. H. Lee, J. H. Na, R. A. Taylor, D. G. Hasko, R. A. Oliver, M. J. Kappers, C. J. Humphreys and G. A. D. Briggs, *Appl. Phys. Lett.* **86**, 213103 (2005).

Chapter 2

Physics of nitride semiconductors and quantum dots

2.1 Physics of nitride semiconductors

2.1.1 GaN

GaN has attracted much attention in recent years, particularly following the development in the mid 1990s of GaN-based high-brightness blue LEDs (1) and GaN-based blue lasers with long operating lifetimes (2).

GaN can crystallize in both the zincblende and the wurtzite structures (1), shown in Figure 2.1. In both structures, the bonding to nearest neighbours is tetrahedral. Under ambient conditions, it is the wurtzite structure which is thermodynamically stable (3). The zero-temperature value of the band gap of wurtzite GaN (which is direct) is 3.51 eV (4) (3.43 eV at room temperature (5)).

The hexagonal crystal structure of wurtzite GaN (and of the other nitride semiconductors,

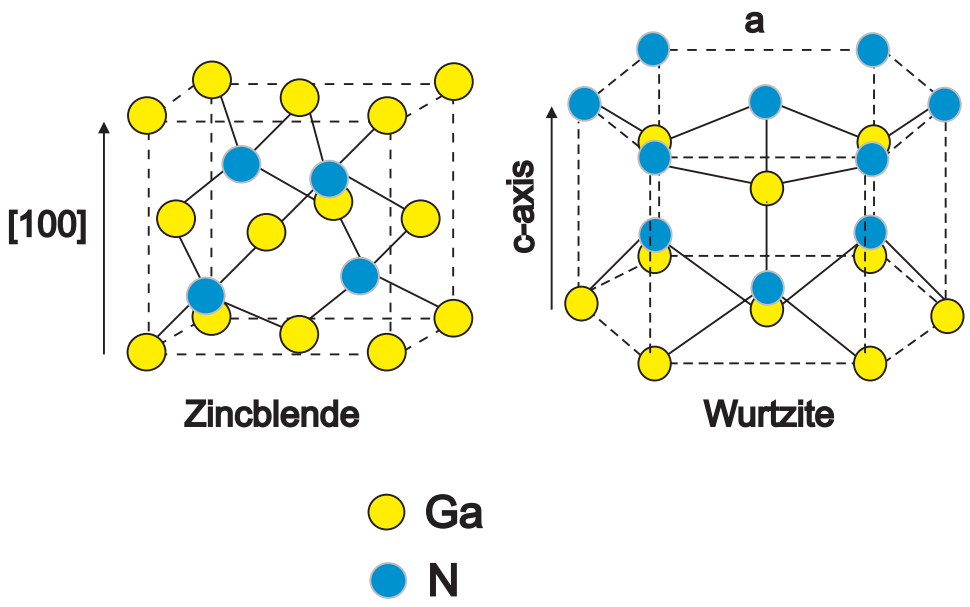


Figure 2.1: The zincblende and wurtzite crystal structures of GaN. The hexagonal wurtzite structure can be described in terms of the edge length a of the basal hexagon and the height c of the hexagonal prism, as shown.

which also crystallize in the wurtzite structure) can be described in terms of the edge length a of the basal hexagon and the height c of the hexagonal prism. The lattice parameters of bulk GaN have been found by x-ray diffractometry to be a=0.3188 nm and c=0.5186 nm (6). In the case of an epitaxial layer (epilayer) of GaN, the value of a depends on the substrate, while the value of c is identical to that in the bulk crystal.

GaN, like other nitride semiconductors, exhibits a 'built-in' electric field, consisting of two components: the spontaneous and piezoelectric fields (7). The spontaneous field occurs because of the wurtzite symmetry of the nitride crystal: there is a spontaneous polarization in the unit cell due to the equilibrium positions of the positive and negative charges. GaN is piezoelectric because the wurtzite crystal structure does not possess a centre of inversion; the (0001) planes differ from the $(000\bar{1})$ planes. In fact, all nitride semiconductors are found to have large negative piezoelectric constants, giving rise to a piezoelectric field under strained

conditions.

In the absence of an external electric field, the total zero-field macroscopic polarization is simply the sum of the spontaneous polarization in the equilibrium lattice and the strain-induced (piezoelectric) polarization. The direction of the spontaneous polarization is determined by the polarity of the crystal, and the direction of the piezoelectric polarization depends on the polarity and whether the material is under tensile or compressive stress (8).

2.1.2 InN

InN is another important nitride semiconductor, but some of its properties are still relatively poorly understood. Like GaN, InN is thermodynamically stable in the wurtzite structure under ambient conditions (3). However, the size of the direct band gap of InN has been a source of some controversy. For many years, the band gap was believed to be ∼1.89 eV (9), but more recent measurements suggest that the band gap may in fact be closer to ∼0.7 eV (10). It now appears that early results were erroneous due to problems in obtaining high-quality InN samples. Recent improvements in epitaxial growth techniques have led to the availability of InN films with considerably lower electron concentrations and much higher electron mobilities.

Pure InN has never been grown as a single crystal, but in epilayers measured values of the lattice parameter a range from 0.3533 nm (11) to 0.3548 nm (12), while measured values of c range from 0.5963 nm (11) to 0.5760 nm (12). This uncertainty in the values of the lattice parameters for InN is likely to hinder attempts to understand self-assembled growth of nitride nanostructures since such growth is dependent upon the mismatch in lattice constants

between the substrate and the epilayer.

In the same way as GaN, InN has a strong 'built-in' electric field due to spontaneous polarization and (under strained conditions) the piezoelectric field.

2.1.3 InGaN

InGaN is a ternary semiconductor whose direct band gap can be varied by adjusting the In:Ga ratio. This band gap tunability makes InGaN very useful for many optoelectronic applications, allowing access to a wide range of wavelengths across much of the visible spectrum.

In general, the band gap of $In_xGa_{1-x}N$ (where x is the In fraction) can be described by an equation of the form

$$E_g^{In_xGa_{1-x}N} = E_g^{GaN}(1-x) + E_g^{InN}x - bx(1-x), \tag{2.1}$$

where $E_g^{In_xGa_{1-x}N}$, E_g^{GaN} and E_g^{InN} are the band gaps of $In_xGa_{1-x}N$, GaN and InN respectively, and where b is known as the *bowing parameter*.

Recent experimental values for the bowing parameter for InGaN alloys range from ∼2.6 eV (13; 14) to ∼4.1 eV (15), for In concentrations $x < 0.2$. Theoretical values are typically around 1.7 eV (16; 17).

Using values for the band gaps of GaN and InN together with the bowing parameter, it is possible to calculate the expected band gap for an InGaN alloy with any In fraction.

As for GaN and InN, InGaN has a strong 'built-in' electric field. This will have important consequences for nanostructures fabricated from InGaN, as will be discussed later.

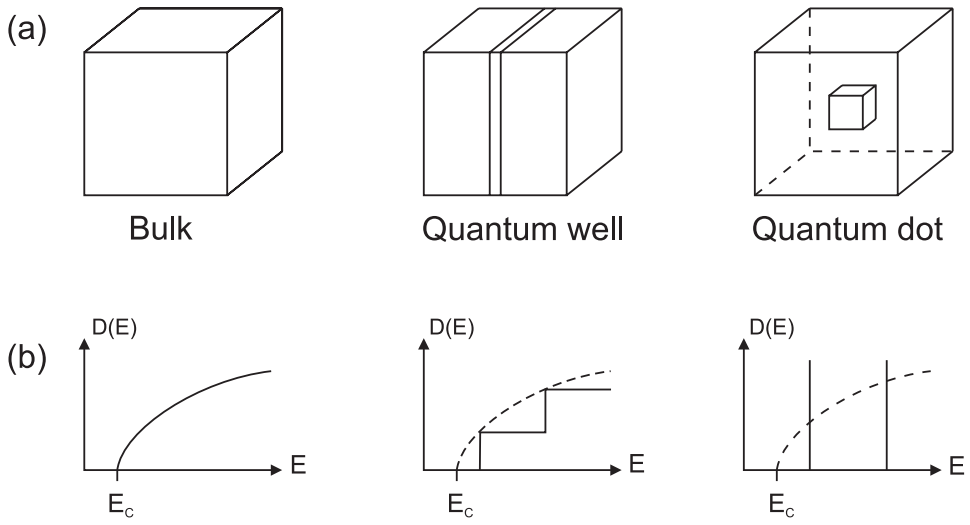


Figure 2.2: (a) Schematic morphology, and (b) density of electronic states in bulk material, quantum wells and quantum dots.

2.2 Quantum dots

2.2.1 Basic properties of quantum dots

In bulk semiconductors, carriers (electrons and holes) can move in all three spatial dimensions. However, it is possible to fabricate semiconductor structures which restrict the number of degrees of freedom by confining carriers in one or more spatial dimensions.

In a quantum well (QW), there is one-dimensional confinement and motion is restricted to a two-dimensional plane (two degrees of freedom). In a quantum wire (QWR), there is two-dimensional confinement and motion is restricted to only one dimension (one degree of freedom). In the quantum dot (QD) structure, first proposed in 1982 (18), confinement is achieved in all three spatial dimensions (zero degrees of freedom) and carriers are completely trapped. This is illustrated in Figure 2.2.

QDs range in size from ∼1 nm to ∼100 nm, and typically contain between 10^3 and 10^6

atoms (19). Three-dimensional confinement in QDs leads to carriers in these structures having certain quantized energy levels. This accounts for the frequent description of QDs as 'artificial atoms': like an atom, a QD has a series of discrete energy levels. However, unlike in atoms, the positions of the energy levels can be selectively 'tuned' by altering the composition or size of the QD. This property is very useful in many optoelectronic applications.

In the simplified case of a cuboid-shaped QD with dimensions (d_x, d_y, d_z) surrounded by infinite potential barriers, it can be shown by solving the Schrödinger equation with appropriate boundary conditions that the energy levels of a carrier trapped in the system will be given by

$$E(n_x, n_y, n_z) = \frac{\pi^2 \hbar^2}{2m^*} \left(\frac{n_x^2}{d_x^2} + \frac{n_y^2}{d_y^2} + \frac{n_z^2}{d_z^2} \right), \tag{2.2}$$

where the quantum numbers n_x, n_y, n_z specify the quantized levels in each spatial direction and where m^* is the effective mass of the carrier (20).

2.2.2 Excitons in quantum dots

If a bulk semiconductor material containing QDs is optically pumped using photons with an energy greater than the bulk band gap, then electrons in the bulk will be excited from the valence band to the conduction band. Each such excitation will generate one free electron in the conduction band and one free hole in the valence band. In general, if the temperature is low, it is possible for both electrons and holes to diffuse through the bulk semiconductor matrix and become trapped in a QD. In the case of cuboid-shaped QDs surrounded by infinite potential barriers, these captured carriers will then be held in the quantized energy levels given by Equation 2.2.

If exactly one electron and one hole become trapped in a single QD, there will be a Coulomb attraction between the electron-hole pair. This will result in the formation of a quasiparticle known as an exciton, or X. The binding energy of the exciton will determined by the separation of the confined carriers, and hence by the size of the QD. Over time, it will be possible for the electron and hole comprising the exciton to radiatively recombine, resulting in the emission of a photon with a characteristic exciton energy.

In addition to the single exciton state, shown in Figure 2.3(a), higher-order processes are also possible. If two electrons and one hole become trapped in a single QD, for example, then a 'charged exciton' known as an X^- will result (Figure 2.3(b)). A charged exciton of the opposite sign known as an X^+ will result from the trapping of one electron and two holes (Figure 2.3(c)). The trapping of two electrons and two holes will give rise to a biexciton, or XX (Figure 2.3(d)).

Coulomb interactions between the various trapped carriers in charged excitons and biexcitons will mean that the recombination energy of an electron-hole pair forming part of one of these quasiparticles will be different from the recombination energy in the single-exciton case. Electron-hole recombination will therefore result in the emission of a photon with a characteristic charged exciton or biexciton energy, enabling the presence of such states to be experimentally detected.

2.2.3 Properties of InGaN quantum dots

Due to the hexagonal symmetry of the wurtzite crystal structure of GaN and InGaN, it would be expected that InGaN QDs grown on a GaN epilayer would also display some sort

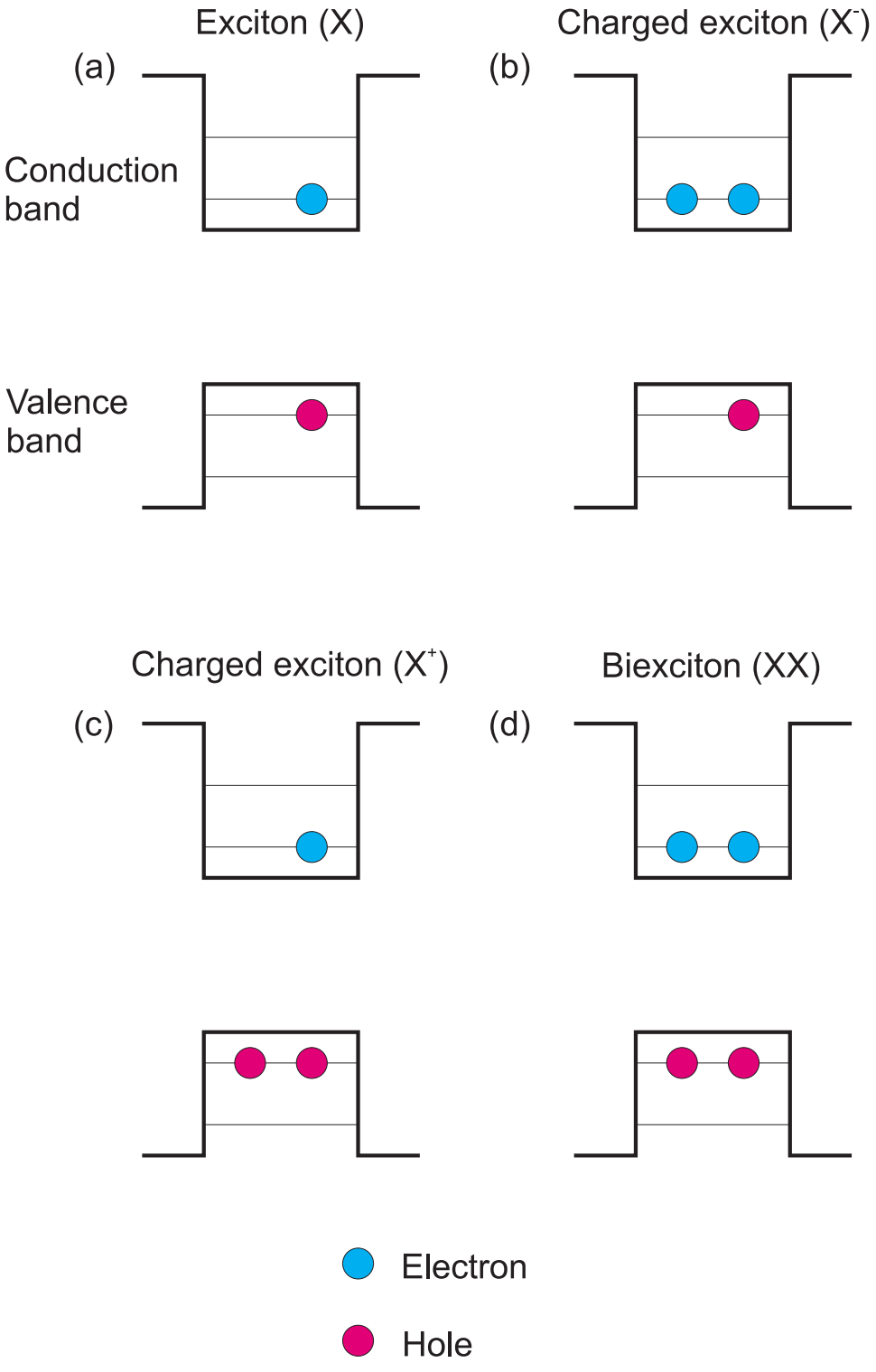


Figure 2.3: An illustration of some of the exciton complexes which can form when carriers become trapped in QDs. (a) The simplest case, where a single electron and a single hole are trapped. This is an exciton (X). (b) Two electrons and one hole form a charged exciton (X^-). (c) One electron and two holes form a charged exciton of the opposite sign (X^+). (d) Two electrons and two holes form a biexciton (XX).

of hexagonal symmetry. Here we will consider two idealized shapes with this symmetry which have been proposed on the basis of experimental measurements and theoretical calculations: the hexagonal truncated pyramidal InGaN QD (Figure 2.4) and the hexagonal prismatic InGaN QD (Figure 2.5) (21). In both cases, the QD may be modelled as a region of InGaN of an appropriate shape completely surrounded by a GaN barrier layer. We now consider the electronic and optical properties of QDs with these shapes.

The first point to consider is the effect of the differing energy positions of the conduction and valence bands in the QD compared to those in the surrounding barrier material. It is the narrower band gap of the InGaN compared to the surrounding GaN which leads to the existence of quantum-confined states within the QD. Theoretical calculations can be used to estimate the energy levels of these states: the single-particle properties can be obtained by solving the Schrödinger equation within the envelope-function and effective-mass approximations, by means of a plane-wave expression with periodic boundary conditions (22). The single-particle states are then used to compute the optical matrix elements within the dipole and rotating-wave approximations.

It is also very important to consider the effect upon the InGaN QDs of the 'built-in' electric field (due to the piezoelectric and spontaneous polarizations). This very strong field will significantly affect the optical properties of the QDs. For epitaxial InN on GaN, the ∼11% difference in lattice constants would be expected to generate a 'built-in' field of as much as ∼16 MVcm^{-1}, using calculated piezoelectric coefficients (23). Clearly, for $In_xGa_{1-x}N$ with $x \sim 0.1$–0.2, the mismatch would be considerably smaller than in the pure InN case, but an extremely strong piezoelectric field of the order of MVcm^{-1} would still be expected.

The main effect of the 'built-in' electric field on a QD is to spatially separate trapped

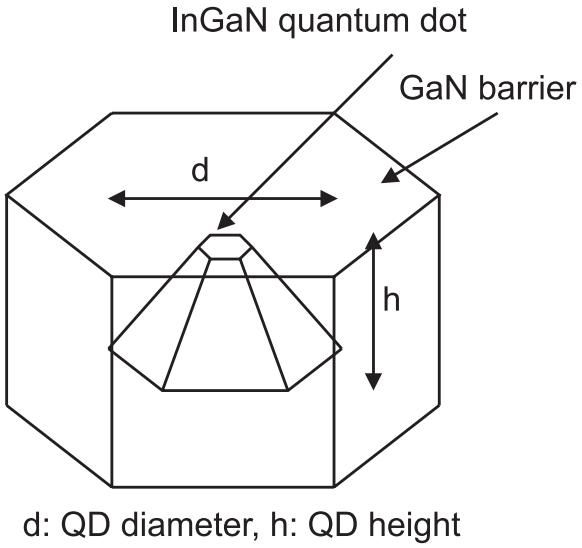


Figure 2.4: An idealized representation of a hexagonal truncated pyramidal InGaN QD surrounded by a GaN barrier.

electrons and holes (22): this is simply the result of the fact that the field gives rise to forces on the electron and hole in opposite directions. The calculated planar-integrated squared wavefunctions for an electron and a hole inside a truncated pyramidal InGaN QD are shown as a function of z (the growth direction) in Figure 2.6; it can be clearly seen that the wavefunctions are spatially separated. This separation will mean that the optical matrix elements for the energetically lowest transitions decrease, which is expected to result in longer exciton lifetimes. Moreover, the separation of the electron and hole will significantly reduce their Coulomb interaction, resulting in the exciton binding energy being significantly reduced. Therefore, there will be a marked reduction in the effective band gap of the QDs (8).

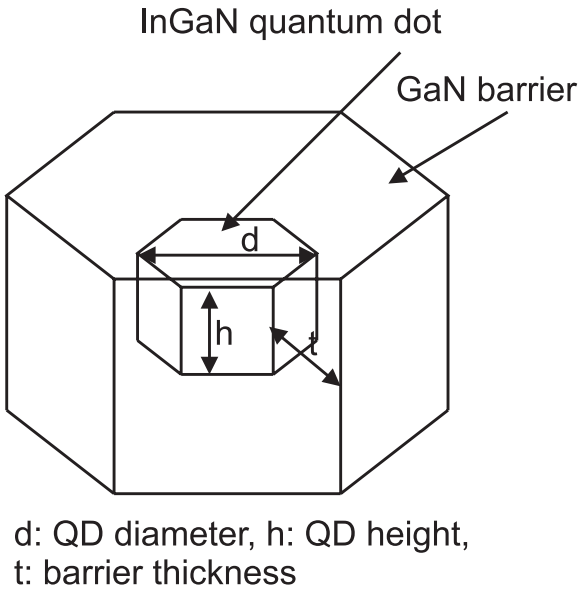


Figure 2.5: An idealized representation of a hexagonal prismatic InGaN QD surrounded by a GaN barrier.

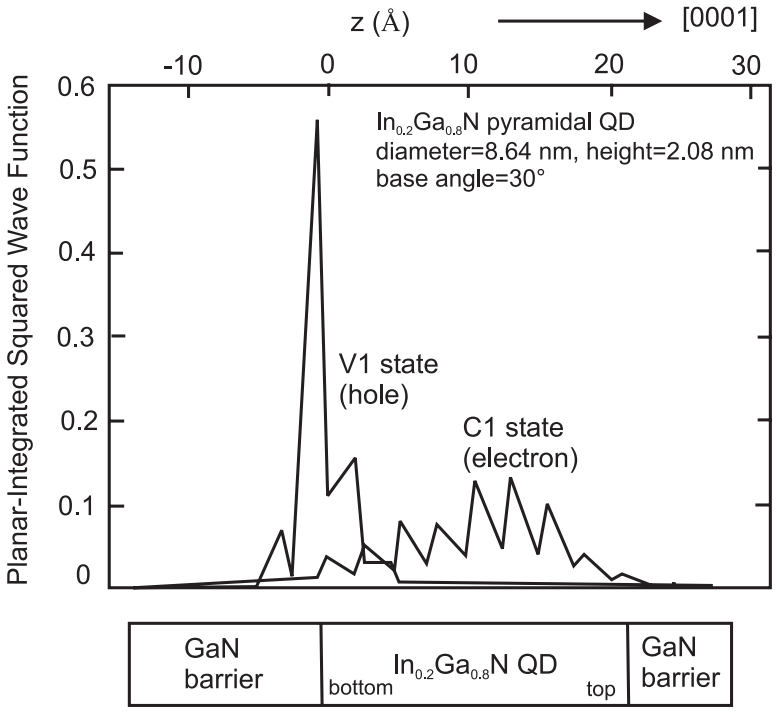


Figure 2.6: A plot showing the calculated planar-integrated squared wavefunctions for the electron and hole as a function of the z-coordinate (the growth direction) in a truncated pyramidal $In_{0.2}Ga_{0.8}N$ QD. The effect of the piezoelectric field in separating the electron and hole wavefunctions is clearly seen. Re-drawn from (21).

2.3 Fabrication of InGaN quantum dots

2.3.1 Introduction to growth

It is possible to form InGaN QD nanostructures in three distinct ways: by self-assembly techniques, by 'selective growth' (involving substrate patterning) or by the formation of interface fluctuations in quantum wells. Self-assembly techniques and selective growth will be considered in more detail later in this Chapter. QDs formed by interface fluctuations are beyond the scope of this work.

The growth of self-assembled QDs can be induced under the correct growth conditions. The QDs form at random locations in a plane parallel to the sample surface. But while the position in the z direction is well-defined, the grower has only statistical control over the in-plane positioning of the QDs (for example, the areal density of the QDs can be varied by changing the growth parameters).

In the case of selective growth, the grower uses photolithographic or ion-beam etching techniques to produce a patterned substrate, causing an array of semiconductor nanostructures then to grow at controlled locations in the plane of the sample surface. The grower has precise control over the locations at which individual QDs will form. This can be important in some applications.

The areal density of self-assembled QDs tends to be high, while it is easier to produce relatively low areal densities using selective growth techniques. While some applications require a high areal density of QDs (e.g. semiconductor lasers), others need a relatively low density and selective growth can be a way of achieving this.

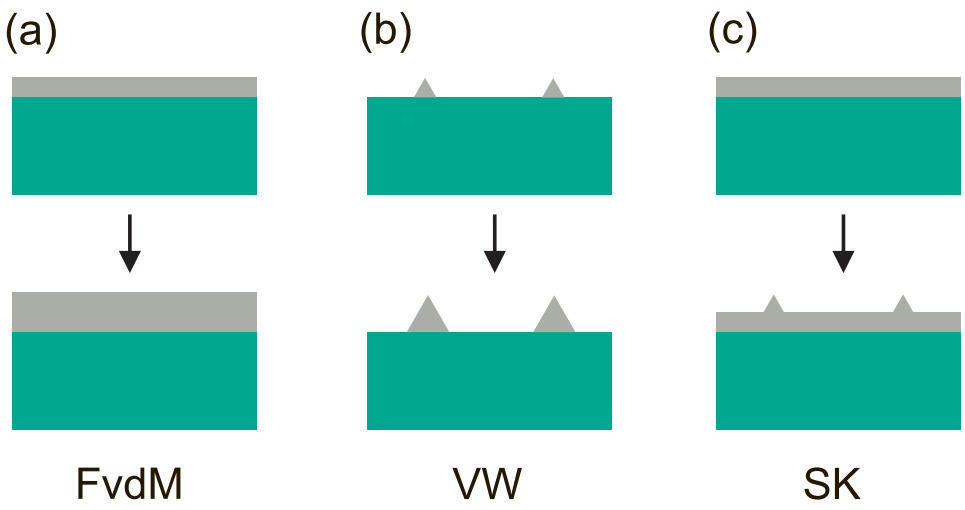


Figure 2.7: A schematic diagram showing the three possible heteroepitaxial growth modes: (a) Frank-van der Merwe (FwdM), (b) Volmer-Weber (VW) and (c) Stranski-Krastanov (SK).

In the rest of this section, the general processes of self-assembly and selective growth of InGaN QDs will be described in more detail. We shall also discuss the particular methods used for the fabrication of the three samples used in this work: Samples A, B and C.

2.3.2 Introduction to growth of InGaN quantum dots by self-assembly

There are three well-known modes of heteroepitaxial growth (24): Frank-van der Merwe (FvdM) (25), Volmer-Weber (VW) (26) and Stranski-Krastanov (SK) (27). They represent layer-by-layer growth (FvdM, 2D), island growth (VW, 3D) and layer-by-layer plus islands (SK), as shown schematically in Figure 2.7. The particular growth mode adopted by a given system depends on the interface energies and on the lattice mismatch.

SK growth relies on the relaxation of a highly mismatched layer by formation of 3D islands rather than misfit dislocations, as is the case for more moderately mismatched layers (FvdM,

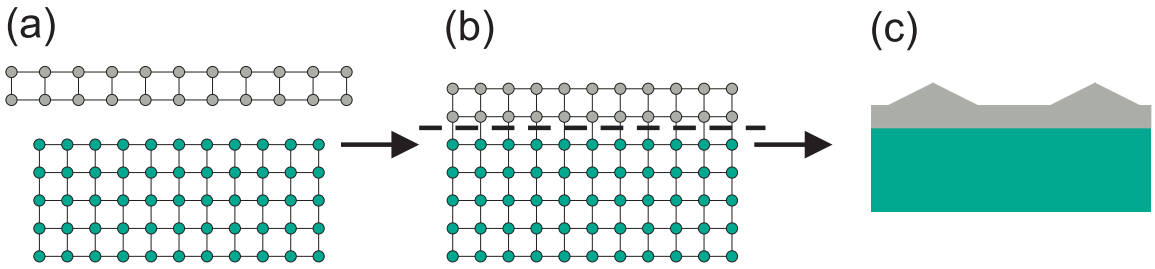


Figure 2.8: An illustration of the SK growth process in InGaN. (a) Under equilibrium conditions, the lattice constant of InGaN is larger than that of GaN. (b) However, a thin layer of InGaN can be successfully grown on a GaN buffer layer. This results in a straining of the InGaN layer. (c) Following further growth, elastic strain is relieved through the formation of coherently-strained self-assembled pyramidal InGaN 'islands': these are QDs. A 2D 'wetting layer' is left in place underneath the QDs.

VW) (28). The growth of a mismatched layer initially forms a thin, homogeneous, and flat film. Further growth builds up strain in the layer, where this strain can be minimized by the formation of 3D islands in the SK growth mode. The 3D islands are coherent with the substrate and generally dislocation free, and they grow on top of a very thin 2D layer, denoted as the 'wetting layer'. They are also of similar shape and size, determined by the growth conditions.

The SK growth mode is of particular interest here since it results in the formation of coherently-strained islands: the absence of defects in such islands is an important factor in determining their optical properties. An illustration of the SK growth process in InGaN is shown in Figure 2.8 (29).

The first observation of SK growth in nitride semiconductor heteroepitaxy was made in 1997, involving growth of GaN on wurtzite AlN (30). Growth of InGaN QDs on AlGaN was reported in the same year (31). SK growth in InGaN/GaN was first demonstrated in 1999 (32).

2.3.3 Sample A: Self-assembled InGaN quantum dots grown by MOCVD

One sample containing self-assembled InGaN QDs was supplied by Prof Yasuhiko Arakawa of the University of Tokyo. This will be referred to as Sample A.

The QDs in Sample A were grown on a sapphire (0001) Al_2O_3 substrate using an atmospheric-pressure two-flow metal-organic chemical vapour deposition (MOCVD) system with a horizontal quartz reactor (32). Trimethylgallium (TMG) and trimethylindium (TMI) were used as group-III sources, while ammonia (NH_3) was used as the nitrogen source. Molecular hydrogen (H_2) and molecular nitrogen (N_2) were the carrier gases.

Initially, a GaN buffer layer with a thickness of 1500 nm was grown at a temperature of 1075°C. InGaN QDs and a wetting layer (WL) were formed at a reduced growth temperature of 700°C by depositing a thin InGaN epilayer on top of the buffer layer, the In fraction being ∼0.2. Finally, a GaN capping layer with a thickness of 14 nm was grown at 770°C. A cross-section through the sample is shown schematically in Figure 2.9. The In composition of the QDs was estimated from the PL spectrum to be between 0.2 and 0.4 (33). However, it should be noted that, since the PL energy is affected not only by the In composition but also by the strain energy, a precise determination of the In fraction is very difficult.

Following growth, the samples were characterized using an atomic force microscope (AFM). The QDs are believed to be truncated-pyramid structures with properties as follows (34): average height 5 nm, average diameter 23 nm, density $\sim 1.0 \times 10^{10}$ cm^{-2}.

For these samples, growth is believed to take place either via the SK process or by a mechanism linked to phase separation.

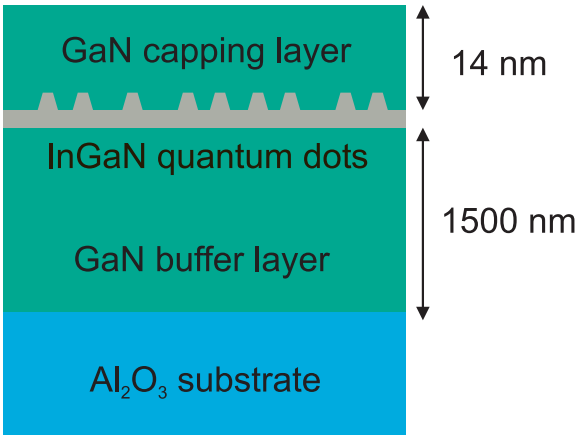


Figure 2.9: A schematic cross-sectional view of Sample A.

2.3.4 Sample B: Self-assembled InGaN quantum dots grown by MOCVD with a post-growth nitrogen anneal

A second sample containing self-assembled InGaN QDs was grown by Dr Rachel Oliver (35) who, at the time, was based at the Department of Materials at the University of Oxford. This will be referred to as Sample B.

The QDs in Sample B were grown by MOCVD in a *Thomas Swan* close-coupled showerhead reactor. The substrate was sapphire (0001) Al_2O_3. TMG and TMI were used as group-III sources, while NH_3 was used as the nitrogen source. Molecular nitrogen (N_2) was the carrier gas.

InGaN epilayers were grown on GaN templates at a temperature of 700°C, followed by a 7 nm GaN capping layer also grown at 700°C.

The growth process for these QDs was novel in that the samples were annealed at 700°C for 30 s in N_2 following InGaN epilayer growth but prior to the growth of the capping layer. Annealing in N_2 is much easier than annealing *in vacuo* because of the growth methodology

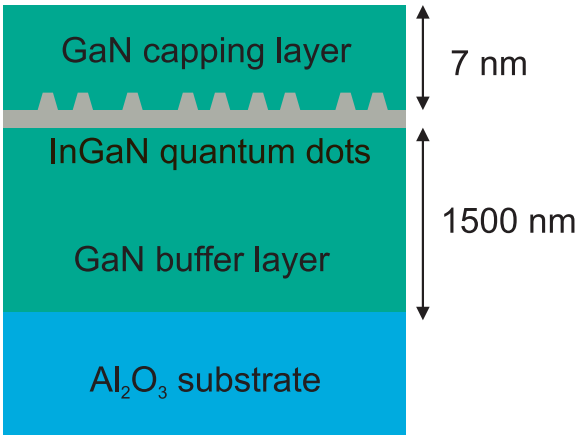


Figure 2.10: A schematic cross-sectional view of Sample B.

and the type of reactor used (36). It is known that N_2 is not reactive under these conditions since the growth temperature is far too low for dissociation to occur. A control sample annealed in NH_3 did not show evidence of QD formation. A cross-section through Sample B is shown schematically in Figure 2.10.

Following growth, the samples were characterized by AFM. The QDs were believed to be of the truncated-pyramid shape, and were found to have a density of $\sim 1\times 10^{10}$ cm^{-2}, an average height of 0.93 nm and an average diameter of 21.6 nm. The average aspect ratio was therefore $\sim$0.05 (36). An AFM scan of the surface of the sample is shown in Figure 2.11 (37).

QD formation is believed to take place via a complicated 'modified droplet epitaxy' process, as shown in Figure 2.12 (35; 37). According to the proposed mechanism, spinodal decomposition (38) causes In-rich regions to form in the InGaN epilayer on a short timescale. During the N_2 anneal stage, the In-rich regions are unstable and decompose into In and N_2. The In thus released is believed to form a thin layer on the surface of the sample; surface tension effects then cause the formation of nanoscopic In droplets. During the final growth stage, in

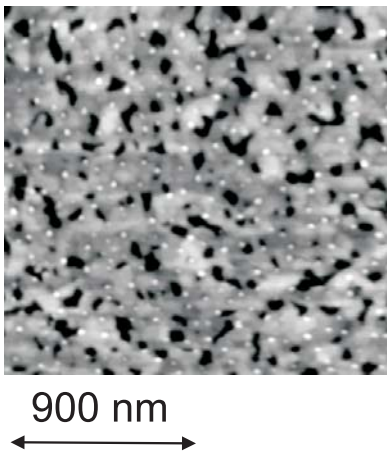


Figure 2.11: An AFM scan of the surface of Sample B. The small light patches are QDs; the dark areas represent 'pitting' on the surface, believed to be due to decomposition of In-rich regions following spinodal decomposition.

which the GaN capping layer is formed, the In droplets combine with N and Ga from the precursor gases and become InGaN QDs. The remaining empty parts of the epilayer are filled with GaN, and the capping layer is formed on top.

2.3.5 Introduction to selective growth of InGaN QDs

The basic methodology of selective growth of InGaN QDs is as follows. A GaN buffer layer (on a sapphire substrate) is covered with a silica (SiO_2) masking layer, in which well-defined apertures are then etched at locations determined by the grower. Further deposition of GaN on top of the masking layer results in growth of GaN only in the unmasked areas. The GaN which grows in these areas will do so in accordance with its wurtzite symmetry, causing hexagonal micropyramids to form in the early stages. Provided that growth is halted before these structures coalesce, an array of pyramidal 'plinths' can be formed. Deposition of further material of the correct composition then allows alternating layers GaN and InGaN to be grown on top of the pyramids, forming 'side wells' on the pyramid facets. These

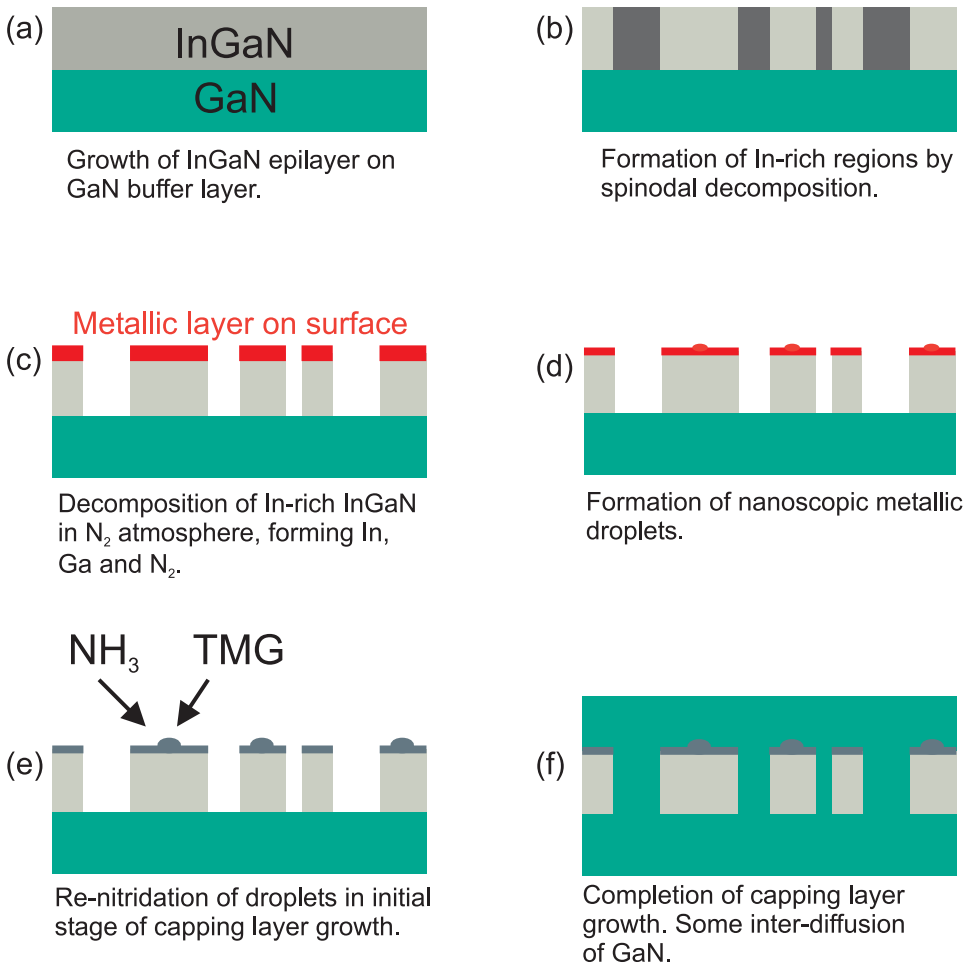


Figure 2.12: The proposed 'modified droplet epitaxy' process by which growth of InGaN QDs is believed to take place for Sample B.

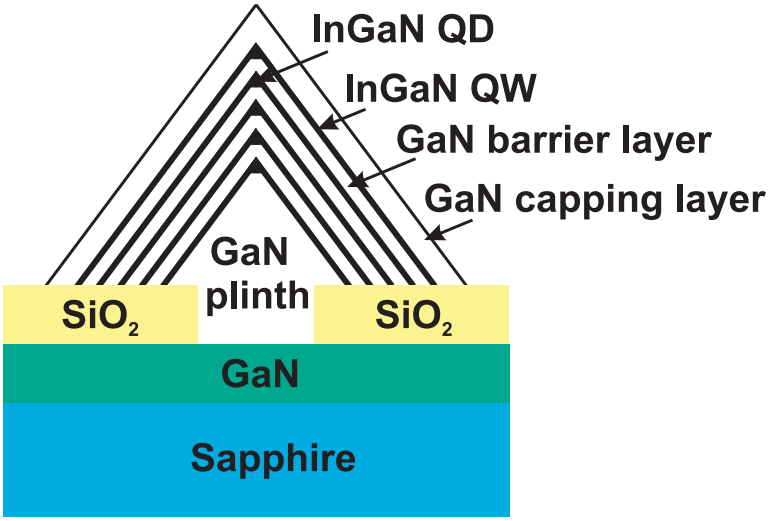


Figure 2.13: A schematic cross-sectional view through a single selectively-grown GaN micropyramid, showing the InGaN and GaN side wells grown on top of the pyramidal GaN plinth. An InGaN QD is believed to form at the sharp apex of each InGaN layer, as indicated.

quantum wells are able to confine electrons and holes in one spatial dimension. Additional confinement appears to occur at the apex of each layer, which means that QDs may form there. A schematic cross-sectional view through a single micropyramid of this type is shown in Figure 2.13.

In early experimental work on selectively-grown GaN micropyramids with InGaN/GaN side wells (39), low-temperature ensemble cathodoluminescence (CL) measurements showed a blue-shift in the emission, indicating that carriers were being confined in three dimensions in the sample. It was suggested that QDs had formed at the apex of each InGaN layer. However, direct experimental confirmation of this claim was not possible without being able to spatially-resolve the photoluminescence originating from individual pyramids.

Later work (40; 41) used high-resolution room-temperature μ-PL spectroscopy to investigate the μ-PL arising from single pyramid structures. The μ-PL was found to originate only from the tops of the pyramids, indicating the presence of strongly-localized states there,

as previously demonstrated in a GaAs system (42). This suggested that InGaN quantum dots may indeed have been formed in these locations. Moreover, the FWHM of the spatial distribution of the intensity was comparable to the spatial resolution of the μ-PL intensity images, indicating that the emitting structures were very small, as would be expected for QDs. However, sharp lines were not observed in the μ-PL, so it was not possible to directly prove that InGaN QDs had actually been formed. It was clear that further work was required to conclusively demonstrate that the structures formed at the apices of InGaN pyramids of this type really are QDs.

2.3.6 Sample C: Selectively-grown InGaN quantum dots

In addition to Samples A and B, a third sample was grown by Dr Robert Martin of The University of Strathclyde. This sample contained selectively-grown InGaN QDs, and will be referred to as Sample C.

Sample C consisted of an array of site-controlled InGaN/GaN QDs, positioned at the apices of GaN micropyramids. The pyramids were formed by MOCVD growth of GaN through an array of circular holes lithographically patterned into a silica mask on a GaN-on-sapphire substrate. The crystal symmetry of the wurtzite GaN results in the formation of hexagonal-based pyramidal structures, with facets formed by $(10\bar{1}1)$ planes. The structures were $\sim$8 μm in height, with base edges of $\sim$5 μm, and were repeated in a hexagonal array with 10 μm pitch to give an areal density of 2×10^6 cm^{-2}. A 5-period InGaN QW structure was subsequently grown on the top surface in order to form QDs at the sharp apices. The QWs were grown using conditions calibrated for non-selective planar growth, for which InGaN wells of 2.0 nm and GaN barriers of 6.0 nm gave a structure emitting at 2.75 eV.

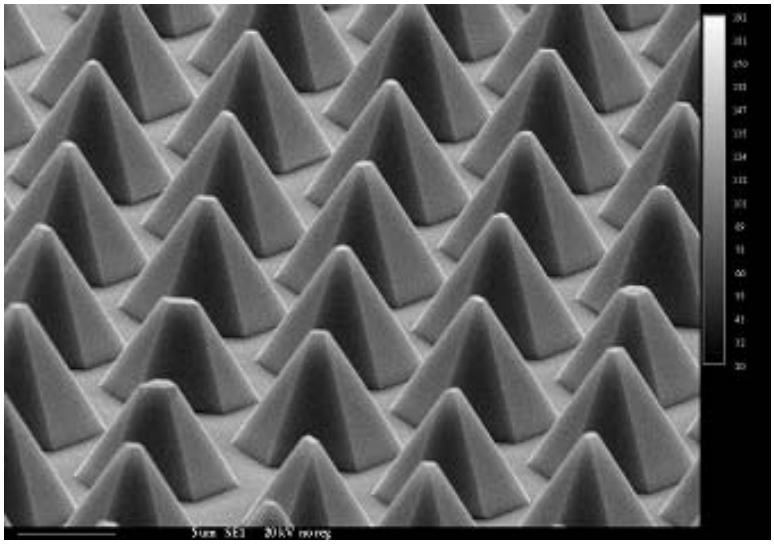


Figure 2.14: A scanning electron microscope image of Sample C, showing part of the regular array of micropyramids (43). The image tilt angle is 70°, and the micropyramid pitch is 10 μm.

A scanning electron microscope (SEM) image of Sample C is shown in Figure 2.14, and an *in-situ* white-light microscope contrast image is shown in Figure 2.15. In both cases, the array of micropyramids can be clearly seen. A high resolution FEG-SEM image of a single micropyramid is shown in Figure 2.16.

2.4 Summary and conclusion

The nitride semiconductors GaN, InN and InGaN are in many respects still relatively poorly understood. Nevertheless, they are an interesting area for study, especially because of their wide direct band gaps which promise interesting optoelectronic applications. These materials exhibit strong 'built-in' electric fields due to spontaneous polarization and piezoelectric effects.

QDs are semiconductor nanostructures in which carriers are confined in all three spatial

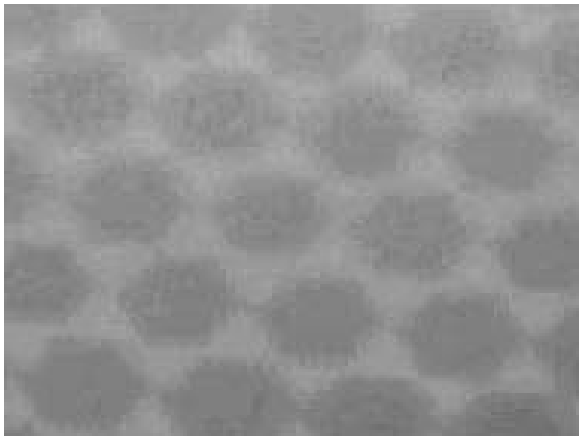


Figure 2.15: An *in-situ* white-light microscope image of Sample C. The contrast is relatively poor, but the regular array of selectively-grown hexagonal micropyramids of GaN can nevertheless be seen.

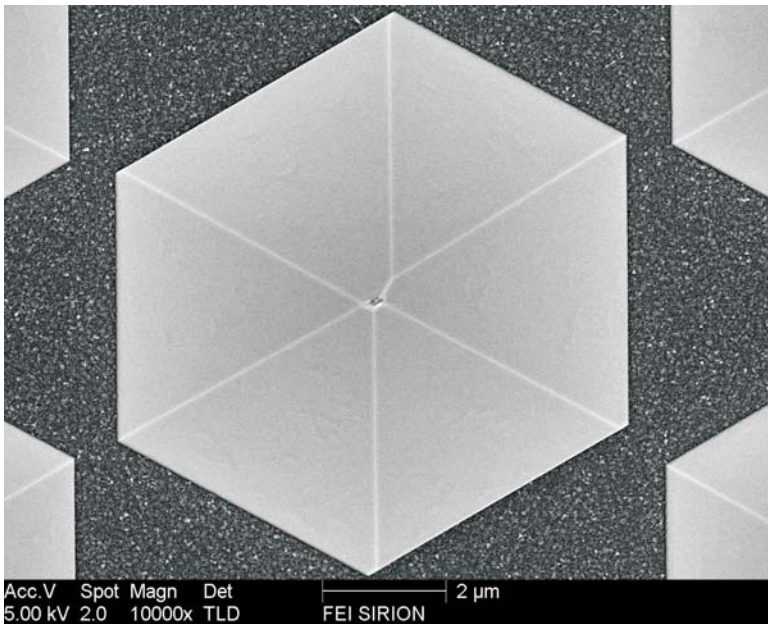


Figure 2.16: A high-resolution FEG-SEM image of a single micropyramid in Sample C (43; 44).

dimensions. Excitons are quasiparticles consisting of bound electron-hole pairs; these can become trapped inside QDs at sufficiently low temperatures. In nitride semiconductors, the strong 'built-in' electric field causes a red-shift of the exciton energy relative to the zero-field case.

The InGaN QDs studied in this work were of three types. Sample A contained self-assembled InGaN QDs grown by MOCVD, probably involving an SK growth process. Sample B contained self-assembled InGaN QDs grown by MOCVD with a post-growth nitrogen anneal, probably formed via a 'modified-droplet epitaxy' process. Sample C contained QDs formed on the apexes of InGaN/GaN pyramids grown by a selective growth route.

References

[1] S. Nakamura and G. Fasol, 'The Blue Laser Diode', Springer-Verlag (1997).

[2] S. Nakamura, M. Senoh, S. Nagahama, N. Iwasa, T. Yamada, T. Matsushita, H. Kiyoku and Y. Sugimoto, *Appl. Phys. Lett.* **68**, 3269 (1996).

[3] R. A. Oliver, *Mat. Sci. and Tech.* **18**, 1257 (2002).

[4] I. Vurgaftman and J. R. Meyer, *J. Appl. Phys.* **94**, 3675 (2003).

[5] A. Trampert, O. Brandt and K. H. Ploog, 'Gallium nitride (GaN) I', (ed. J. I. Pankove and T. D. Moustakas), *Semiconductors Semimetals* **50**, 167 (1998).

[6] M. Leszczynski, T. Suski, H. Teisseyre, P. Perlin, I. Grzegory, J. Jun, S. Porowski and T. D. Moustakas, *J. Appl. Phys.* **76**, 4909 (1994).

[7] F. Bernardini, V. Fiorentini and D. Vanderbilt, *Phys. Rev. B* **56**, R10 024 (1997).

[8] J. J. Shi and Z. Z. Gan, *J. Appl. Phys.* **94**, 407 (2003).

[9] T. L. Tansley and C. P. Foley, *J. Appl. Phys.* **59**, 3241 (1986).

[10] J. Wu, W. Walukiewicz, K. M. Yu, J. W. Ager III, E. E. Haller, H. Lu, W. J. Schaff, Y. Saito and Y. Nanishi, *Appl. Phys. Lett.* **80**, 3967 (2002).

[11] T. L. Tansley and C. P. Foley, *J. Appl. Phys.* **60**, 2092 (1986).

[12] A. Wakahara and A. Yoshida, *Appl. Phys. Lett.* **54**, 709 (1989).

[13] C. Wetzel, T. Takeuchi, S. Yamaguchi, H. Katoh, H. Amano and I. Akasaki, *Appl. Phys. Lett.* **73**, 1994 (1998).

[14] H. P. D. Schenk, P. de Mierry, M. Läugt, F. Omnès, M. Leroux, B. Beaumont and P. Gibart, *Appl. Phys. Lett.* **75**, 2587 (1999).

[15] C. A. Parker, J. C. Roberts, S. M. Bedair, M. J. Reed, S. X. Liu, N. A. El-Masry and L. H. Robins, *Appl. Phys. Lett.* **75**, 2566 (1999).

[16] Z. Dridi, B. Bouhafs and P. Ruterana, *Semicond. Sci. Technol.* **18**, 850 (2003).

[17] M. van Schilfgaarde, A. Sher and A.-B. Chen, *J. Crystal Growth* **178**, 8 (1997).

[18] Y. Arakawa and H. Sakaki, *Appl. Phys. Lett.* **40**, 939 (1982).

[19] D. Gammon, *Nature* **405**, 899 (2000).

[20] M. Fox, 'Optical Properties of Solids', Oxford University Press (2001).

[21] T. Saito and Y. Arakawa, *Physica E* **15**, 169 (2002).

[22] U. Hohenester, R. Di Felice, E. Molinari and F. Rossi, *Appl. Phys. Lett.* **75**, 3449 (1999).

[23] R. W. Martin and K. P. O'Donnell, *Phys. Stat. Sol. (b)* **216**, 441 (1999).

[24] D. Bimberg, M. Grundmann and N. Ledentsov, 'Quantum Dot Heterostructures', John Wiley & Sons (1999).

[25] F. C. Frank and J. H. van der Merwe, *Proc. Roy. Soc. Lond. A* **198**, 205 (1949).

[26] M. Volmer and A. Weber, *Z. Phys. Chem.* **119**, 277 (1926).

[27] I. N. Stranski and L. Krastanov, *Sitzungsberichte d. Akad. d. Wissenschaften in Wien*, Abt. IIb, Band 146, 797 (1937).

[28] A. Gustafsson, M.-E. Pistol, L. Montelius and L. Samuelson, *J. Appl. Phys.* **84**, 1715 (1998).

[29] From R. A. Oliver (private communication).

[30] B. Daudin, F. Widmann, G. Feuillet, Y. Samson, M. Arley and J. L. Rouviere, *Phys. Rev. B* **56**, 7069 (1997).

[31] H. Hirayama, S. Tanaka, P. Ramvall and Y. Aoyagi, Proceedings of the 2nd International Conference on Nitride Semiconductors (ICNS97), Tokushima, Japan, 472 (1997).

[32] K. Tachibana, T. Someya and Y. Arakawa, *Appl. Phys. Lett.* **74**, 383 (1999).

[33] O. Moriwaki, T. Someya, K. Tachibana, S. Ishida and Y. Arakawa, *Appl. Phys. Lett.* **76**, 2361 (2000).

[34] Y. Arakawa (private communication).

[35] R. A. Oliver, G. A. D. Briggs, M. J. Kappers, C. J. Humphreys, J. H. Rice, J. D. Smith and R. A. Taylor, *Appl. Phys. Lett.* **83**, 755 (2003).

[36] R. A. Oliver, DPhil Thesis, University of Oxford (2003).

[37] From R. A. Oliver (private communication).

[38] D. A. Porter and K. E. Easterling, 'Phase Transformations in Metals and Alloys' (2nd ed.), Chapman and Hall, London (1993).

[39] J. Wang, M. Nozaki, M. Lachab, Y. Ishikawa, R. S. Qhalid Fareed, T. Wang, M. Hao and S. Sakai, *Appl. Phys. Lett.* **75**, 950 (1999).

[40] K. Tachibana, T. Someya, S. Ishida and Y. Arakawa, *J. Cryst. Growth* **221**, 576 (2000).

[41] K. Tachibana, T. Someya, S. Ishida and Y. Arakawa, *Appl. Phys. Lett.* **76**, 3212 (2000).

[42] Y. Nagamune, M. Nishioka, S. Tsukamoto and Y. Arakawa, *Appl. Phys. Lett.* **64**, 2495 (1994).

[43] Image supplied by Dr Robert Martin of the University of Strathclyde.

[44] This image was acquired using equipment provided as part of an FEI tender evaluation.

Chapter 3

Experimental development and techniques

3.1 Generation of laser light

3.1.1 Introduction

An important means of probing the properties of semiconductor materials, including QDs, is the use of *luminescence* techniques. Luminescence is a general term for the light which is emitted when carriers (electrons and holes) radiatively recombine. In order to generate luminescence, some means of exciting carriers is required. In this work, such excitation was normally provided optically: this technique is known as photoluminescence (PL) spectroscopy.

Optical excitation for PL is often provided through the use of laser radiation, which has the advantages of being highly monochromatic and of allowing easy access to high power densities. In this work, both continuous-wave (CW) and ultrafast pulsed laser sources were

used. A CW laser emits a continuous wave train, whereas an ultrafast pulsed laser produces short (∼fs), well-separated pulses.

3.1.2 Continuous-wave laser source

The CW laser used in this work was a *Kimmon Electric Co.* 'IK3151R-E' He-Cd laser, operating at a wavelength of 325.0 nm. The output power was ∼16 mW, and the beam diameter (to $1/e^2$ intensity points) was ∼0.9 mm (1). The He-Cd is a gas laser. The discharge tube contained He gas at a pressure of several torr and a partial pressure of Cd ∼1% of that of the He. The excitation mechanism was the transfer of energy via Penning ionization from He metastable levels to the Cd upper laser levels (2).

3.1.3 Principles of ultrafast pulse generation

As discussed in Section 3.1.1, laser light can be used to excite carriers in a semiconductor system, thus generating PL which provides data about electronic processes. CW excitation, however, can only provide 'time-integrated' (averaged over time) information. In order to be able to resolve short-duration processes, fast laser pulses are required. These must be of comparable length to the events under study. Since many of the processes which occur in semiconductors (e.g. carrier recombination) take place on very short timescales, ultrafast laser pulses (in the fs range) are needed to time-resolve them.

One approach to achieving short laser pulses is the use of *Q-switching*, where the gain of a laser cavity is modulated on a short timescale (2). Unfortunately, Q-switched pulses are limited to minimum pulse durations of a few ns. Another technique which allows the

generation of ultrafast laser pulses is known as *mode-locking*. This has been successfully used to generate pulses in the fs range.

Mode-locking relies on the fact that a laser cavity generally supports a number of different 'cavity modes' of slightly different frequency. These are different longitudinal modes of lasing, each satisfying the cavity boundary conditions and for each of which the gain in the cavity exceeds the losses. The number of these modes can vary from just a few (in a He-Ne laser, for example) to $\sim 10^4$ (in a Ti:Sapphire laser) (3). Normally, the various cavity modes would oscillate with a random phase relationship, and their sum (the laser output) would show a random intensity fluctuation with time as shown in Figure 3.1(a). However, if the cavity modes are somehow brought into phase with each other, then their sum will no longer show random intensity fluctuations. Instead, the laser output will display a well-defined repeating pattern of intensity maxima and minima, consisting of repetitive short pulses as shown in Figure 3.1(b). As the number of cavity modes is increased, the mode-locked pulses become sharper and the laser output intensity between pulses falls off towards zero.

In practice, mode-locking can be achieved either *passively* or *actively*. An example of a passive mode-locking technique is the insertion of a saturable absorber into the laser cavity. The absorber normally appears as a high-loss element, but will 'bleach' when a high-intensity pulse reaches it. This allows a high-intensity mode-locked pulse to be transmitted while strongly inhibiting transmission at other times. In active mode-locking, a shutter is inserted in the laser cavity which must be actively opened at exactly the right time when the laser pulse arrives. One way of achieving this is through the use of an acousto-optic modulator, consisting of a quartz crystal with a piezoelectric transducer attached to one side. The crystal is located at one end of the laser cavity near the laser mirror, typically with crystal surfaces

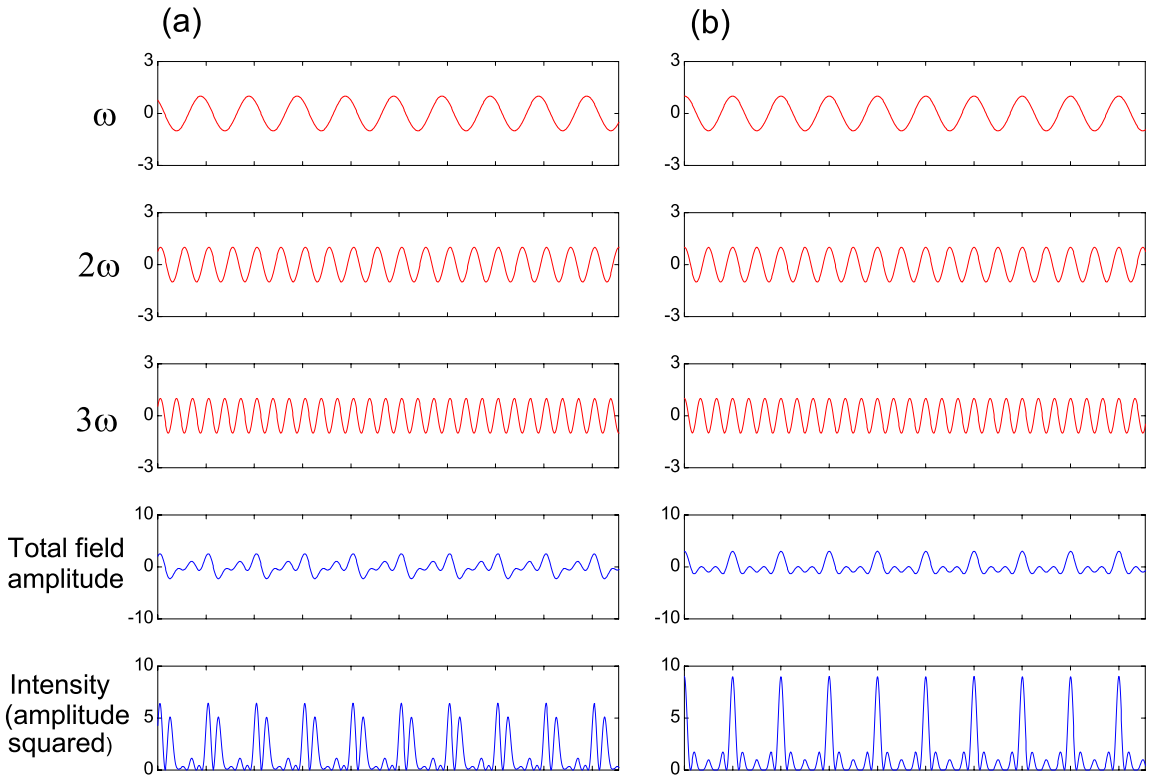


Figure 3.1: An illustration of the principle of mode-locking. (a) Amplitude and intensity of the sum of three out-of-phase waves added together, and (b) amplitude and intensity of the sum of three in-phase waves added together. In (a), the output is periodic but random. In (b), the output consists of regular peaks together with a small amount of output between the peaks. If a larger number of modes is added together in phase, the output will show sharper pulses with an even smaller inter-pulse intensity.

positioned at Brewster's angle to minimize reflective losses from the quartz surfaces. A radio-frequency (rf) signal (typically 25–50 MHz) applied to the transducer causes a periodic loss within the crystal due to Bragg reflection (at twice the frequency of the rf signal). When the loss is not present (when the rf signal is at zero electric field), the shutter is 'open', the mode phases are locked and the short pulse passes through the shutter (2).

In the right circumstances, it is possible for a laser to become mode-locked spontaneously, a situation known as *self mode-locking* (3). One way in which this can occur is through *Kerr lens mode-locking* (KLM). The process of KLM can occur in a non-linear amplifying medium which has a refractive index that is a function of intensity: $n = n_0 + n_2 I$. This is the Kerr effect (4). If n_2 is positive, the refraction is stronger on the axis of the beam than away from it. Thus the amplifying medium behaves like a converging lens and focuses the beam. Since the change in refractive index becomes larger with increasing intensity, the focusing effect becomes stronger as the beam intensity rises. This means that high-intensity beams will be reduced in diameter, occupying less volume in the cavity and therefore suffering lower losses than low-intensity beams. Since high-intensity beams are favoured at the expense of low-intensity beams, the cavity will naturally tend to bring about mode-locking, which results in short, high-intensity pulses.

3.1.4 Ultrafast pulsed laser sources

Two separate pulsed laser systems were used in this work for time-resolved experiments. These were a *Spectra-Physics* 'Mai Tai' and a *Coherent* 'Mira'. Both were high-power Ti:Sapphire devices which generated ultrafast pulses in the fs range using mode-locking.

In Ti:Sapphire systems, the gain medium is a rod of sapphire (Al_2O_3) doped with ∼0.05% titanium by weight. The doped crystal is made by introducing Ti_2O_3 into a melt of Al_2O_3. Ti^{3+} ions are randomly substituted for Al^{3+} ions, giving rise to a wide absorption band of excited states (5). The Ti:Al_2O_3 rod must be optically pumped to induce a population inversion.

The 'Mai Tai' consisted of two laser systems. The first was a CW pump laser (based on the *Spectra Physics* 'Millennia'), and the second was a mode-locked Ti:Sapphire laser (based on the *Spectra Physics* 'Tsunami') (6). The pump laser was a neodymium yttrium vanadate (Nd:YVO_4) device, itself pumped by the output from two fibre-coupled CW laser diode bars. A lithium triborate (LBO) crystal placed in the cavity frequency-doubled the intracavity light from its wavelength of 1064 nm to a wavelength of 532 nm. The pump laser generated 5 W of power which was then used to optically pump the mode-locked laser, the gain medium for which was a Ti:Al_2O_3 crystal.

The 'Mai Tai' was tunable over the wavelength range 750–850 nm and operated at a repetition rate of 80 MHz. The pulse width was less than 100 fs and the mean power was ∼630 mW. Initial mode-locking in the 'Mai Tai' was achieved actively using an acousto-optic modulator. Mode-locking was then maintained via KLM.

The 'Mira' was in many ways similar to the 'Mai Tai', but exhibited a larger tunability range and higher maximum output power. The 'Mira' was optically pumped by a separate free-standing CW system, the *Coherent* 'Verdi'. This was a Nd:YVO_4 laser (7), pumped by the output from two fibre-coupled CW laser diode bars. Intracavity frequency doubling from 1064 nm to 532 nm was achieved using an LBO crystal. The 'Verdi' produced 10 W of power which was then used to optically pump the 'Mira', the gain medium for which was a

Ti:Al_2O_3 crystal.

The 'Mira' was tunable over the wavelength range 720–990 nm (using three different sets of optics) and operated at a repetition rate of 76 MHz (8). The pulse width was 200 fs, and the mean power at 800 nm was >1 W. Mode-locking in the 'Mira' was achieved via KLM, the system being initially perturbed into the mode-locked state using a pair of intra-cavity oscillating rhombi.

3.1.5 Frequency upconversion

Since the energy of the photons produced by a Ti:Sapphire laser (∼1.55 eV at λ=800 nm) was much less than the bandgap of GaN (3.51 eV), it was necessary to increase the photon energy in order to be able to carry out above-bandgap optical pumping for PL experiments. This was done using *frequency upconversion* via parametric interactions in a birefringent, highly non-linear crystal.

In the process of frequency upconversion, two photons with frequencies ω_1 and ω_2 incident upon a non-linear crystal can generate a single photon of frequency $\omega_3 = \omega_1 + \omega_2$ via a second-order process. This is illustrated in Figure 3.2(a). In the special case that $\omega_1 = \omega_2$, we have $\omega_3 = 2\omega_1$: this is known as *frequency doubling* (Figure 3.2(b)). It is also possible to carry out *frequency tripling*: in this process, a doubled photon of frequency $2\omega_1$ is combined with a photon at the original frequency ω_1, giving rise to a tripled photon of frequency $\omega_3 = 3\omega_1$ (Figure 3.2(c)).

Frequency upconversion is possible in non-linear materials because these materials have a non-linear relationship between applied electric field E and induced polarization P. In a

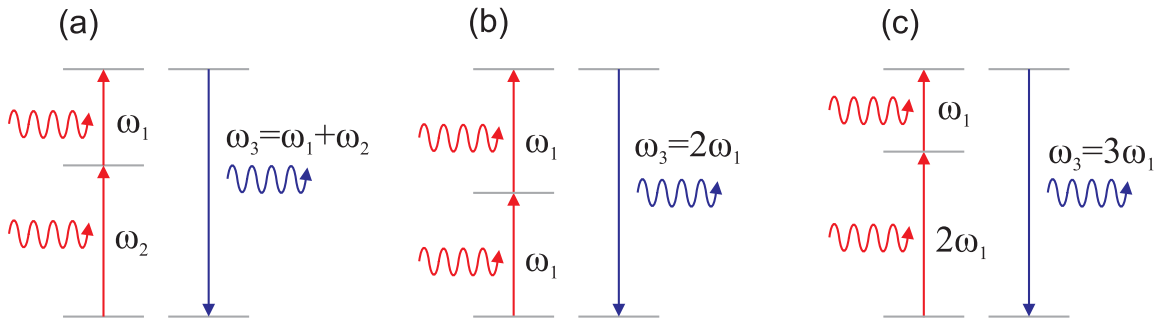


Figure 3.2: An illustration of the principle of frequency upconversion (energies not shown to scale). (a) In the general case, two incoming photons of frequency ω_1 and ω_2 can be used to generate a single photon of frequency ω_3, where $\omega_3 = \omega_1 + \omega_2$. (b) In the special case $\omega_1 = \omega_2$, we have $\omega_3 = 2\omega_1$. This is *frequency doubling*. (c) It is also possible to carry out *frequency tripling* by combining a photon of frequency $2\omega_1$ (from (b)) with an additional photon of frequency ω_1, thus generating a photon of frequency $\omega_3 = 3\omega_1$.

linear dielectric medium, the induced polarization P is proportional to the electric field E at that point, and the two are related by the expression $P = \varepsilon_0 \chi E$, where χ is the *electric susceptibility*. In a non-linear material, the induced polarization can be written as

$$P = \varepsilon_0 \chi_1 E + \varepsilon_0 \chi_2 E^2 + \varepsilon_0 \chi_3 E^3 + ..., \tag{3.1}$$

where χ_1, χ_2 and χ_3 are the linear, second-order and third-order susceptibilities (9). The coefficients decrease rapidly for higher-order terms and these are not shown in Equation 3.1. The importance of the second-order and third-order terms depends on the field strength E, and in fact only when E becomes very large are the non-linear effects observable.

It is the presence of the higher-order terms in the susceptibility which makes upconversion possible. Consider frequency doubling. In this case, an intense beam of light of frequency ω_1 is incident on a non-linear crystal. The electric field associated with the optical field will induce a polarization in the crystal. Since the intensity is high, this induced P will be non-linear in electric field. P can therefore be written as the sum of an oscillation at the fundamental frequency ω_1 together with smaller components at higher frequencies. It can be

shown that the most intense oscillation apart from that at the fundamental frequency will be the *second harmonic* at $2\omega_1$.

The second harmonic ($2\omega_1$) oscillation of local dipole moments generates secondary second harmonic waves in the crystal. However, these second harmonic waves will not necessarily interfere constructively, as is required for the generation of a second harmonic *beam*. The crystal will normally possess different refractive indices $n(\omega_1)$ and $n(2\omega_1)$ for frequencies ω_1 and $2\omega_1$, which means that the ω_1 and $2\omega_1$ waves will propagate with different phase velocities. Constructive interference of the second harmonic waves to form a beam will only occur if the second harmonic waves propagate with the same phase velocity as the fundamental wave. This condition is called *phase matching* and requires $n(\omega_1) = n(2\omega_1)$.

Phase matching can be achieved in practice using a birefringent crystal since such a material has two refractive indices: the ordinary index n_o, and the extraordinary index n_e. Suppose that along a certain crystal direction, at an angle θ to the optic axis, $n_e(2\omega_1)$ is the same as $n_o(\omega_1)$. This is known as *index matching* and the angle θ is the *phase matching angle*. The fundamental wave then would propagate as an ordinary wave and the second harmonic would propagate as an extraordinary wave, and both would be in phase. Thus a second-harmonic beam at $2\omega_1$ would be generated.

After exiting the crystal, the second harmonic beam can be separated from the residual fundamental beam using a diffraction grating, prism or optical filter.

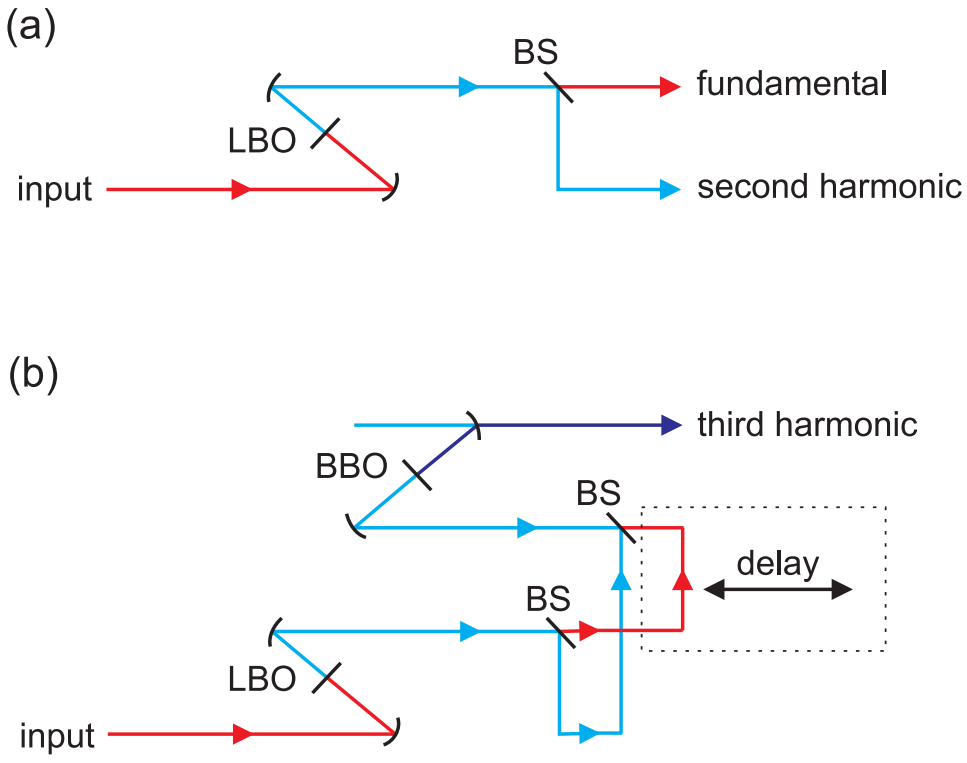


Figure 3.3: A schematic diagram of the optical layout of the *INRAD*, showing (a) second-harmonic generation and (b) third-harmonic generation. In (a), frequency doubling is achieved using an LBO crystal and the frequency-doubled beam is separated from the residual fundamental beam using a dichroic beamsplitter (BS). In (b), the frequency-doubled beam is combined with the residual fundamental beam (with appropriate temporal overlap) and third-harmonic generation is achieved using a BBO crystal.

3.1.6 Ultrafast harmonic generation

Frequency doubling and tripling of the pulsed Ti:Sapphire laser output at 800 nm was carried out in this work using an *INRAD* '5-050 Ultrafast Harmonic Generation System' (10). This made it possible to generate ultrafast beams with wavelengths of 400 nm or 266 nm respectively. The optical layout of the *INRAD* is shown schematically in Figure 3.3.

Frequency doubling or *second-harmonic generation* (SHG) in the *INRAD* was achieved using a non-linear birefringent lithium triborate (LiB_3O_5 or LBO) crystal. The fundamental beam was focused into the LBO crystal, generating a blue beam of twice the frequency. The crystal

could be tilted to achieve angle phase matching and could be translated in the focusing direction to the exact focal point of the fundamental beam.

Frequency tripling or *third-harmonic generation* (THG) in the *INRAD* was achieved using a non-linear birefringent beta-barium borate (β-BaB_2O_4 or BBO) crystal. The blue beam generated using SHG was separated from the residual red fundamental beam. The two beams were then recombined at another beamsplitter, with correct temporal overlap of pulses being achieved using a micrometer-positioned linear translation stage. (Temporal overlap was essential, since without it there can be no upconversion.) The two beams were then focused into the BBO crystal, with phase matching again ensured through rotation of the crystal. The resulting THG beam was then separated off from the residual SHG beam and fundamental, and the two components were directed out of the system.

A typical 1 W input at 800 nm into the *INRAD* could be used to generate ∼100 mW of light at 400 nm via frequency-doubling, or ∼40 mW of light at 266 nm via frequency-tripling.

3.2 Micro-photoluminescence spectroscopy

3.2.1 Introduction

In Section 3.1.1, the use of PL spectroscopy for studying the electronic properties of semiconductor systems (including QDs) was discussed. In many cases, such as the study of QDs for use in laser gain media, the experimenter is mainly interested in making PL measurements on large *ensembles* rather than single QDs. However, there are some potential applications, such as single photon sources and quantum information processing, for which single-QD

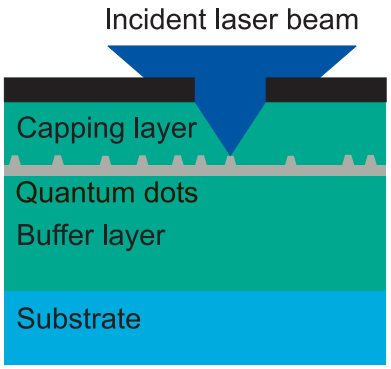


Figure 3.4: A schematic diagram showing the principle of μ-PL spectroscopy. The laser beam used for optical excitation is focused so that it has only a small spot size on the sample surface. An opaque metallic mask (shown here in black) may be deposited on the surface of the sample, allowing laser light to reach only a small area in the QD layer.

measurements are necessary.

It is generally difficult to perform single-QD spectroscopy since the areal density of QDs is typically very high, of the order of $\sim 10^{10}$ cm^{-2}. However, this problem has recently been overcome through the use of *μ-PL spectroscopy*.

The term μ-PL was originally used to describe PL excitation through an optical microscope where the laser spot was focused to a size of ~ 1 μm, thus illuminating only a small number of QDs. It is now used to describe any PL set-up where high spatial resolution is obtained. Instead of (or as well as) focusing the laser spot, it is possible to use an optically opaque metal mask (typically aluminium, silver or gold) on the sample surface to limit the number of QDs illuminated. Another approach is to etch 'mesas': these are raised areas on the sample surface on which QDs form (with no QDs forming on the rest of the sample surface). The principle of μ-PL spectroscopy is illustrated in Figure 3.4.

3.2.2 Early micro-photoluminescence measurements of single quantum dots

The first μ-PL measurement on a single QD was made in 1992 (11). The GaAs/AlGaAs QD which was studied was made by focused-laser-beam-induced local interdiffusion of a GaAs/AlGaAs single-quantum-well structure.

The first μ-PL measurement on a single *self-assembled* QD was made in 1994 (12). This early work looked at an InAs QD grown on GaAs, and involved the use of a microscope to focus the exciting laser beam to a spot size of $\sim$2 μm. High spatial resolution was achieved through the etching of mesas with lateral dimensions as small as 200 nm. Sharp lines were observed in the PL, a clear indication of single QD emission.

The use of masking instead of mesas to select a small area of the sample surface was first demonstrated in 1995 (13). A gold mask was used, where holes were defined by bonding and subsequently removing a gold wire, which took with it some of the mask. The use of lithography, followed by metallization and lift-off, to define mask holes was first demonstrated in 1996 (14) with InP QDs on GaInP.

The first μ-PL measurement of a single InGaN QD on GaN was made in 2000 (15). An aluminium mask with a thickness of 100 nm was used to restrict the number of QDs being illuminated. The PL was found to contain very sharp lines, clearly indicative of single QD emission.

3.2.3 Sample masking

As already discussed in Section 3.2.1, masking can be used to reduce the area of the sample from which light is collected, thus reducing the number of QDs from which luminescence will be observed.

Sample masking was used in this work. The masking and lithography were carried out by Dr Shazia Yasin and Dr Mohammad Khalid of the Microelectronics Research Centre at the University of Cambridge.

A 100-nm-thick aluminium layer was evaporated onto the surfaces of Samples A and B and a mask pattern was fabricated using electron-beam lithography and reactive ion etching by $SiCl_4$. Square apertures were produced with side lengths between 100 nm and 2 μm, together with markers to indicate the position of each aperture. Numbers were also etched into the mask, allowing each aperture to be readily identified.

Microscope images of part of one of the sample masks are shown in Figure 3.5.

3.2.4 Commercial *Renishaw* micro-photoluminescence system

For preliminary μ-PL measurements, at relatively low resolution and only using the CW laser source, a commercial *Renishaw* μ-PL system was used. Although offering lower spectral and spatial resolution than the high-resolution system later constructed by the author (see Section 3.2.5), this commercial system was considerably easier to use and did not require time-consuming manual alignment.

The *Renishaw* was ideal for making initial measurements on new samples in order to quickly

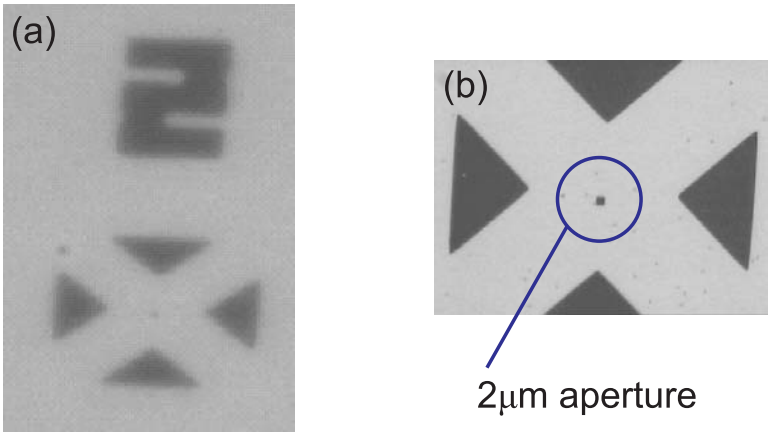


Figure 3.5: White-light microscope images showing part of the aluminium mask on one of the samples. These images were recorded using the *Renishaw* μ-PL system which is described in Section 3.2.4. (a) An image at 15× magnification. The square aperture is located at the centre of the triangular position indicators. The large '2' indicates the aperture number. (b) The same region of the sample at a higher magnification (50×). The square aperture (with a side length of 2 μm in this case) is clearly visible.

determine their overall PL characteristics. It could also be used in experimental work for which high spectral resolution was not a critical factor.

The system comprised several main sections (16; 17), as follows:

- The **laser**. This was an external He-Cd device, operating CW at 325.0 nm and delivering an output power of ∼16 mW. More details about this laser are given in Section 3.1.2.

- The main **spectrometer** section, based on a standard *Renishaw* 'RM-series' spectrometer. This was fully motorized and controlled by an external PC. A single reflection grating covered the entire wavelength range using an 'extended scanning' method.

- The **CCD detector**, mounted on the main spectrometer section. The CCD was used to detect the light dispersed by the spectrometer, and was Peltier-cooled to -70°C in order to reduce thermal noise.

- The **optical microscope** section, based on a standard *Leica* microscope. This was used in confocal geometry, such that the same **objective lens** was used both to focus the laser light on to the sample and to collect and collimate the resulting PL. The spot size of the laser beam on the sample surface was $\sim$2 μm. The microscope could be switched between laser-beam illumination and white-light illumination. When using white-light illumination, a **video camera** could be used to view the sample surface, allowing alignment over the required position. **Binocular eyepieces** were also fitted for direct sample observation. The microscope was equipped with a manual *xyz* micrometer **translation stage**, allowing the sample to be moved so that the desired part could be studied.

- The **personal computer (PC)**, running *Renishaw's* 'WiRE' software. This was used to acquire data from the CCD and from the video camera fitted to the optical microscope. The PC also allowed the user to control the reflection grating and neutral density (ND) filters inside the main spectrometer section, giving control of the wavelength monitoring range and of the intensity of the laser beam reaching the sample.

A diagram indicating the main elements comprising the system is shown in Figure 3.6, and Figure 3.7 shows two photographs.

3.2.5 High-resolution micro-photoluminescence system

For higher-resolution measurements than could be obtained using the *Renishaw*, a second μ-PL system was constructed by the author. This is shown in outline in Figure 3.8. The

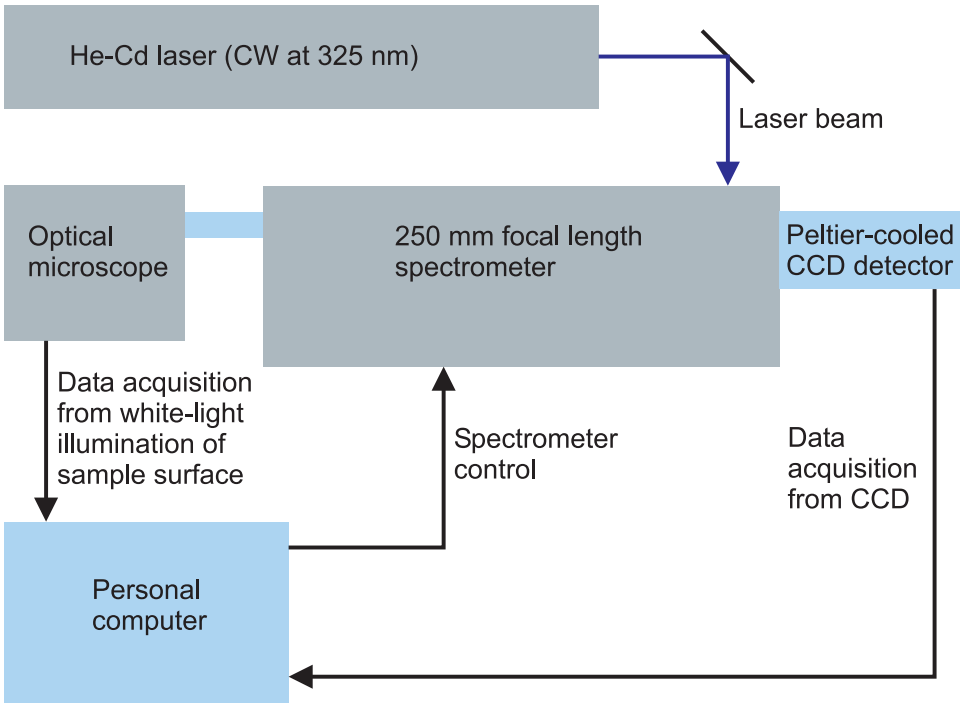


Figure 3.6: A diagram showing the basic elements of the *Renishaw* μ-PL system, as described in more detail in the text.

second μ-PL set-up reproduced the main elements of the *Renishaw*, but alignment and optimization had to be carried out manually.

Since the new μ-PL system could be used with a range of spectrometers, it was possible to achieve considerably higher spectral resolution with this system than was possible with the *Renishaw* (which had a fixed 0.25 m single-grating spectrometer). Moreover, unlike the *Renishaw*, the new system was equipped with a piezoelectric *xyz* translation stage so that the objective lens could be precisely positioned (to within $\sim$5 nm) over the desired position on the sample. Thus the new system also had much higher spatial resolution than the *Renishaw*.

The new μ-PL system used an *Ealing* '25-0522' 36$\times$ reflecting objective lens in confocal geometry. This had a working distance of 8.0 mm and was held immediately above the cryostat. Since the objective exclusively employed reflecting surfaces (rather than lenses) it

(a)



(b)



Figure 3.7: Photographs of the commercial *Renishaw* μ-PL set-up. (a) A view of the whole system, showing the main spectrometer section on the right and the *Leica* optical microscope on the left. (b) A close-up view of the microscope. Part of the main spectrometer section is visible on the right. The *Oxford Instruments* cryostat is clearly seen, mounted on a manual *xyz* translation stage below the microscope. The cable connected to the cryostat runs to the temperature-control unit. Liquid helium enters the cryostat through the vertical metal tube to the right.

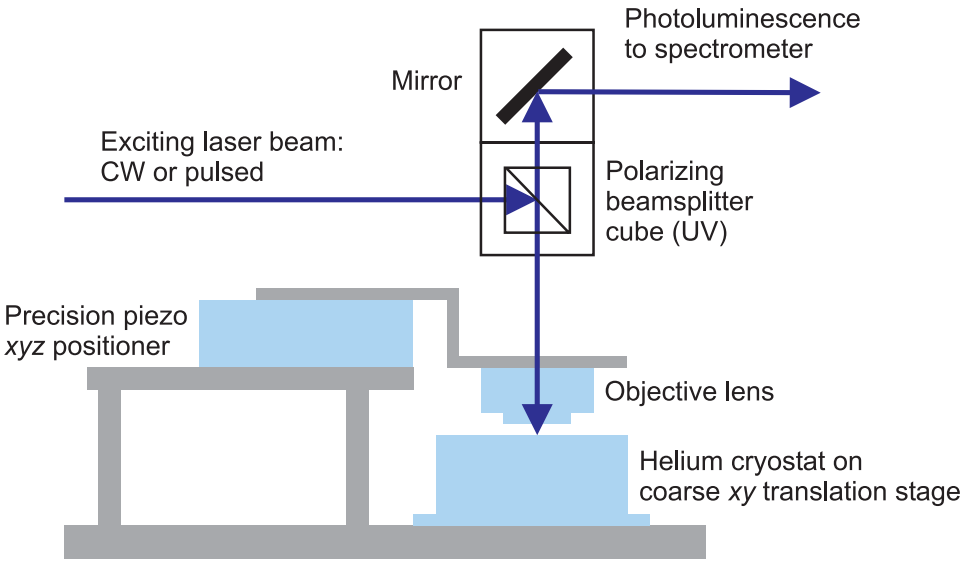


Figure 3.8: A schematic diagram of the high-resolution microscope system used for μ-PL measurements. This was constructed by the author.

was achromatic and could be used successfully in the blue visible and near-ultraviolet (UV) regions of the spectrum. As for the *Renishaw*, the spot size of the laser beam on the sample surface was $\sim$2 μm.

In order to achieve precise positioning relative to the sample, the objective was attached to a *Melles Griot* 'NanoMax TS' piezoelectric translation stage, with feedback on all three channels. In this device, small changes in the potential difference applied across bars of a piezoelectric material led to small expansions or contractions of the bars. Using three mutually-orthogonal bars, the translation stage allowed small displacements to be independently made in the x, y and z directions. The position of the stage was stabilized with high accuracy using a feedback system. In this way, the objective could be positioned to within a resolution of 5 nm in all three spatial directions. Such fine control of the objective position, together with the high mechanical stability of the cryostat against vibrations, was essential in allowing the PL from a single QD to be monitored over an extended period of time.

Light from the laser used for excitation was directed to the objective by a polarizing beam-splitter cube. Because of the wavelength response of the dielectric coating on the internal interface of the cube, most of the incident laser light was directed downwards, while most of the luminescence (which lay at a longer wavelength, being at a lower energy) passed back up through the cube without deviation. The luminescence was then directed into a spectrometer using a system of mirrors and lenses. Various spectrometers were used in the course of this work, and these are discussed in more detail in Section 3.4.

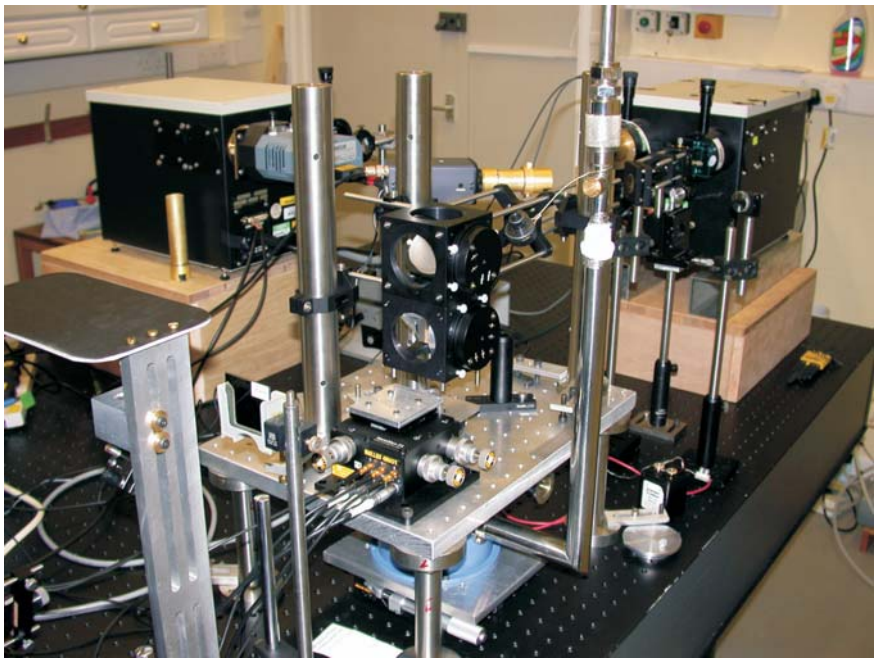
It was important to be able to determine the position of the objective above the sample relative to the pattern of apertures on the mask. In order to achieve this, a blue LED was placed inside the cryostat, directly underneath the sample. Light from the LED was transmitted upwards only through the unmasked areas. This transmitted light passed through the objective and could be directed as required to a CCD video camera using a removable mirror. The CCD video camera was connected to a monitor, which then displayed an image of the apertures on the sample mask. When making μ-PL measurements, the extra mirror was removed and the LED was switched off.

Two photographs of a typical experimental arrangement are shown in Figure 3.9.

3.3 Cryogenic apparatus

μ-PL measurements were made at low temperatures. The sample was cooled to the desired temperature using an *Oxford Instruments* 'Microstat-HiRes' continuous-flow liquid-helium cryostat (18), shown schematically in Figure 3.10. The sample was mounted in vacuum on a heat exchanger, and was cooled by conduction. It was held close to a thin UV-transparent

(a)



(b)

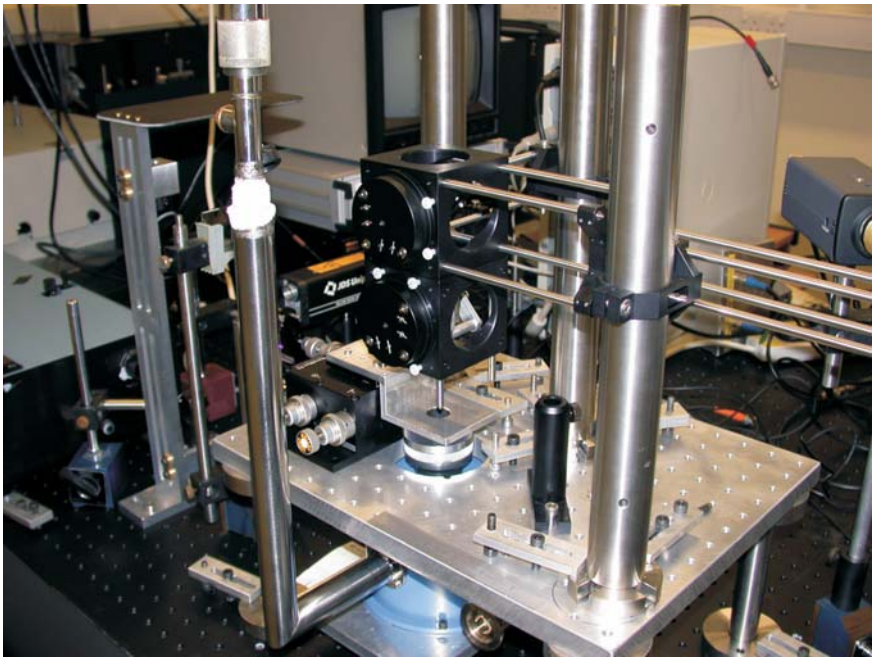


Figure 3.9: Photographs showing the high-resolution μ-PL set-up constructed by the author. (a) The cryostat and piezo-mounted objective lens are seen in the foreground. The laser beam enters from the left via the periscope, and the resulting PL is sent to one of the two single-grating spectrometers for either time-resolved or time-integrated measurements. The video camera used for sample positioning can seen between the spectrometers. (b) Close-up view of the piezo-mounted objective and μ-PL collection system.

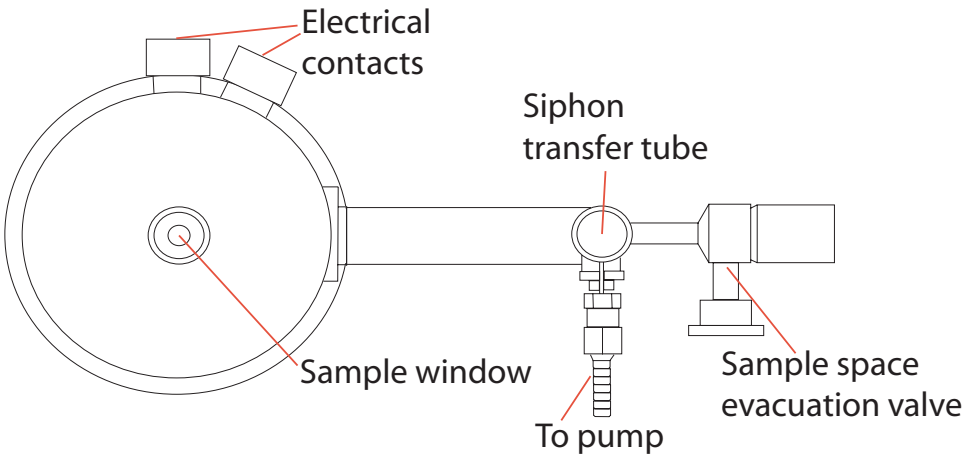


Figure 3.10: A schematic overhead view of the *Oxford Instruments* cryostat. Liquid helium enters through the vertical transfer tube towards the right of the diagram. The cryostat can be evacuated using the valve to the right of the liquid helium inlet. Electrical contacts to the interior are made via the two ports on the body of the cryostat.

window at the top of the cryostat, such that its surface was only a short distance below the cryostat lid; this allowed the sample to be brought close to the objective lens of the microscope. The sample space was thermally isolated from the room-temperature surroundings by an outer vacuum chamber.

The cryostat was highly stable against vibrations in all three axial directions, an important requirement for sensitive spatially-resolved μ-PL measurements.

The cryostat did not have an internal reservoir to store a supply of helium. Instead, helium was supplied from a separate dewar through an insulated transfer tube. The transfer tube delivered the liquid helium to a heat exchanger close to the sample space, thus cooling the sample. The cold gas returning from the heat exchanger then cooled the radiation shield used to protect the heat exchanger and flowed out of the cryostat. A 'Cernox' thermometer (a thin-film resistance temperature sensor) and electrical heater were mounted on the heat exchanger, and these could be used together with an electronic temperature controller to

determine the temperature of the sample.

An 'ITC 503' electronic temperature controller was used to control the heater, allowing the temperature of the sample to be varied between room temperature and ∼4.2 K, with a stability of ±0.1 K. The temperature control could be optimized by setting the optimum values for various parameters: Proportional band (P); Integral action time (I); and Derivative action time (D).

The transfer tube used to convey the liquid helium from the storage dewar to the cryostat was an *Oxford Instruments* 'LLT' vacuum-insulated model. The flow was drawn through the cryostat using an *Oxford Instruments* 'GF3' gas flow pump. This was an oil-free diaphragm pump with a nominal displacement of 42 litres per minute. A 'VC31' gas flow controller was used to control the flow of gas. It included a flow meter (calibrated for helium gas) and a pressure gauge, so that the flow rate could be monitored.

Electrical connections could be made to devices inside the cryostat using the contacts on one of the two external sockets fitted to the cryostat.

3.4 Spectrometers

Three types of free-standing spectrometers were used in this work to disperse the PL collected using the high-resolution μ-PL system described in Section 3.2.5. The choice of spectrometer for a particular experiment depended on the spectral resolution which was required, since higher resolution inevitably came at the cost of reduced light throughput.

The *reciprocal linear dispersion* of a spectrometer of focal length l equipped with a reflection

grating whose lines are separated by distance d can be calculated using the standard result

$$\frac{\mathrm{d}\lambda}{\mathrm{d}x} = \frac{d}{l}, \tag{3.2}$$

where $d\lambda$ is a small change in wavelength and where dx is the corresponding small change in the position of the light reaching the focal plane.

The first type of spectrometer was a *Spex* 'Minimate' 0.34 m single-grating device, equipped with a 1200-grooves/mm grating. Using Equation 3.2, the reciprocal linear dispersion is found to be 2.46 nm/mm. With a 35 μm slit, the spectral resolution was a relatively poor $\sim$650 μeV at a wavelength of 400 nm (as confirmed by calibration measurements), but the light throughput was high. The high throughput was important for low-intensity signals, and this spectrometer was used when very high resolution was not necessary. The grating could be driven using an external electronic control system (based on a stepper motor), allowing the desired wavelength to be selected. Calibration with a spectral lamp was always required before making experimental measurements.

The second type of spectrometer was a higher-resolution 0.85 m double-grating device, the *Spex* '1404'. This was equipped with two 1200-grooves/mm gratings. Using Equation 3.2 (and allowing for the two gratings), the reciprocal linear dispersion is found to be 0.49 nm/mm. The spectral resolution with a 35 μm slit was therefore $\sim$130 μeV at a wavelength of 400 nm (as confirmed by calibration measurements), but the throughput was lower than for the 0.34 m single-grating device. This spectrometer could also be driven to the desired wavelength position using an external electronic control system, and calibration using a spectral lamp was required.

The third type of spectrometer was the *Andor* 'Shamrock SR-303i', a pre-aligned 0.3 m

single-grating device. This spectrometer was fully automatic, and was considerably easier to use than either of the other two spectrometers. Since the 'Shamrock' was self-calibrated, time-consuming spectral-lamp calibration was not required. The 'Shamrock' was equipped with three interchangeable gratings with 1200, 600, and 300 grooves/mm, giving (from Equation 3.2) reciprocal linear dispersions of 2.78 nm/mm, 5.57 nm/mm and 11.1 nm/mm respectively.

The 'Shamrock' was controlled by an external PC via a USB interface. The PC allowed computer control of the motorized entrance slit and of the rotating triple-grating 'turret' (fitted with the three gratings), so that the desired monitoring wavelength and spectral resolution could be easily selected. This spectrometer also featured a computer-controlled flipper mirror. Normally (when the flipper was in position in 'P1'), light bypassed this mirror and fell directly onto a CCD detector. However, when the flipper mirror was in position 'P2', light was directed out of the spectrometer (via an exit slit fitted on a side exit port) to another instrument. This arrangement was very useful since it permitted the spectrometer to be aligned with an intense single-QD signal (using the CCD detector) before the light from this QD was simply switched out of the spectrometer for further study.

3.5 CCD and computerized data acquisition

For time-integrated measurements using the high-resolution μ-PL system constructed by the author, an *Andor* CCD detector (Model DU 420-BR-DD) was used to detect the light dispersed by one of the spectrometers described in Section 3.4.

The CCD chip was a silicon-based device with an array of 1024×256 pixels, the pixel size

being 26 μm. The unit was equipped with a three-stage Peltier-effect cooler in order to reduce thermal noise, and was typically operated at a temperature of -80°C. Figure 3.11 shows the quantum efficiency of the detector at room temperature and at -100°C. It also shows the dark current as a function of temperature. Cooling the CCD to its operating temperature is seen to have little effect upon the quantum efficiency, but the dark current is reduced by several orders of magnitude.

The CCD was controlled by a PC running the programme *Andor* MCD. This gave control over data acquisition, allowing the user to specify the integration time, and to start and stop accumulations. The programme also allowed for the subtraction of 'background' counts (consisting of 'dark counts' and of counts coming from light sources in the laboratory other than the experiment). Background subtraction was always carried out. First, the user blocked the laser beam used for excitation so that the sample was not excited and no PL was emitted. Then a 'background' spectrum was recorded. Finally, the laser was unblocked and the background spectrum which had been recorded was automatically subtracted from subsequent experimental spectra (each recorded over the same period of time as the background).

The MCD software also allowed for the automatic subtraction of cosmic ray events. These were short-duration, very high-intensity peaks sometimes seen in the CCD spectrum. They were caused by high-energy particles from outside the Earth's atmosphere striking the detector. In order to achieve subtraction of cosmic ray events, the desired total integration time for a particular measurement could be divided into a number of equal-length sections. MCD then automatically compared the data obtained in the various sections, and deduced which events were due to cosmic rays: these would be sharp peaks that only appeared in one of the spectra. The cosmic ray events were automatically removed.

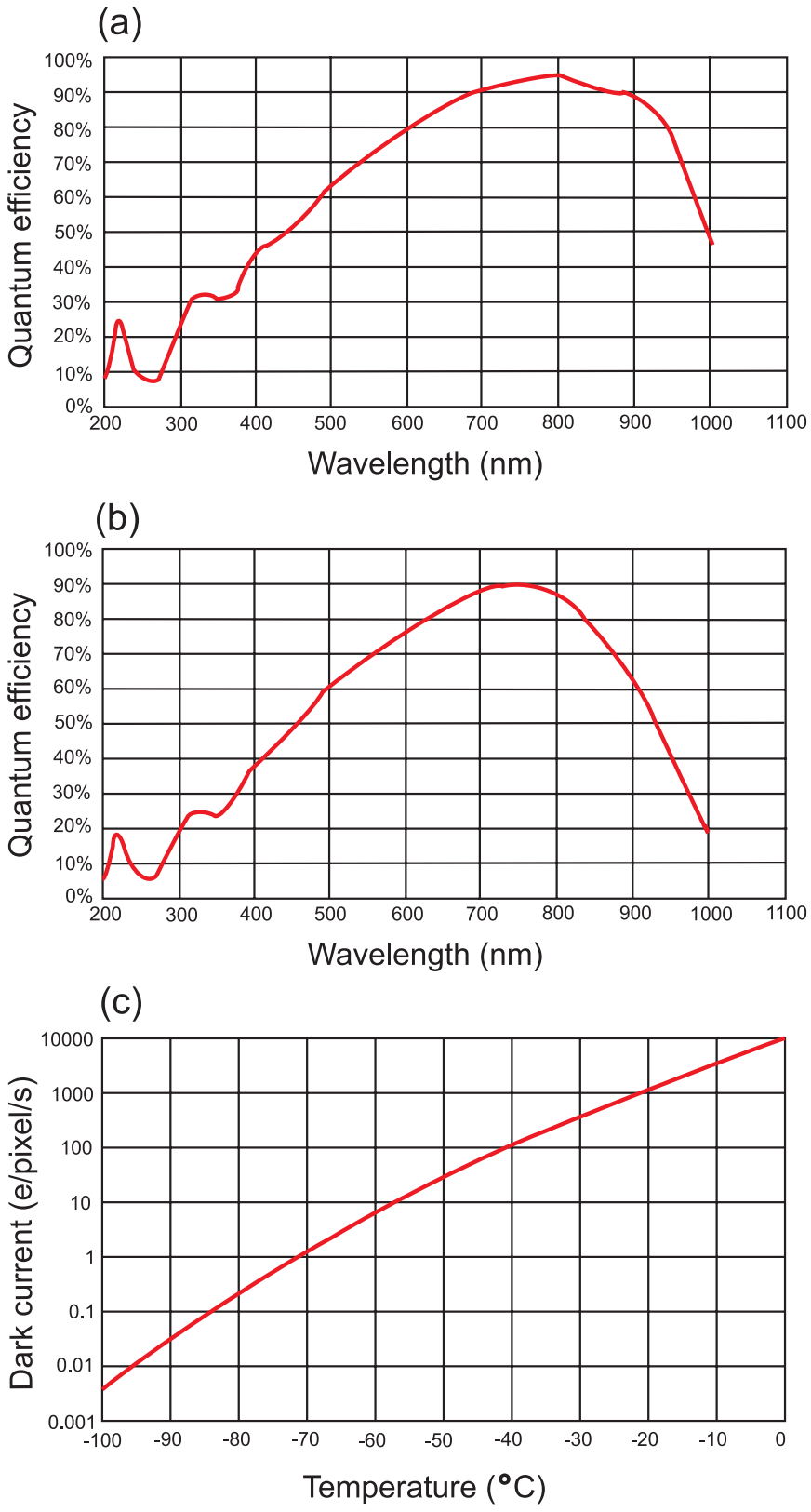


Figure 3.11: The quantum efficiency of the *Andor* CCD detector (a) at room temperature, and (b) at -100°C. (c) The dark current as a function of temperature. Re-drawn from (19).

3.6 Time-correlated single photon counting

3.6.1 Importance of time-resolved measurements

As well as the time-integrated measurements made using the CCD detector, it was also necessary (as previously discussed) to be able to carry out time-resolved measurements in order to determine the dynamics of short-timescale processes occurring in InGaN QDs. Time-resolved measurements required a pulsed laser source (as mentioned in Section 3.1.3), but a sufficiently fast detector and readout electronics were also necessary. The detector and readout system had to be able to operate on the timescale of the interval between laser pulses. In this work, time-resolved measurements were made using time-correlated single photon counting.

3.6.2 Principle of time-correlated single photon counting

Time-correlated single photon counting (TCSPC) works upon the basis of the detection of single photons from a periodic light signal (20). By measuring the detection times of the individual photons, it is possible to indirectly reconstruct the original time-dependent waveform.

Detection is carried out over a consecutive series of very short time periods. For low-intensity, high-repetition-rate signals (conditions which generally apply in μ-PL measurements), the probability of detecting more than one photon in a given signal period is much less than unity. Consider what happens if TCSPC is performed over a large number of such signal periods. For many of the signal periods, no photons are detected, for some of the periods a

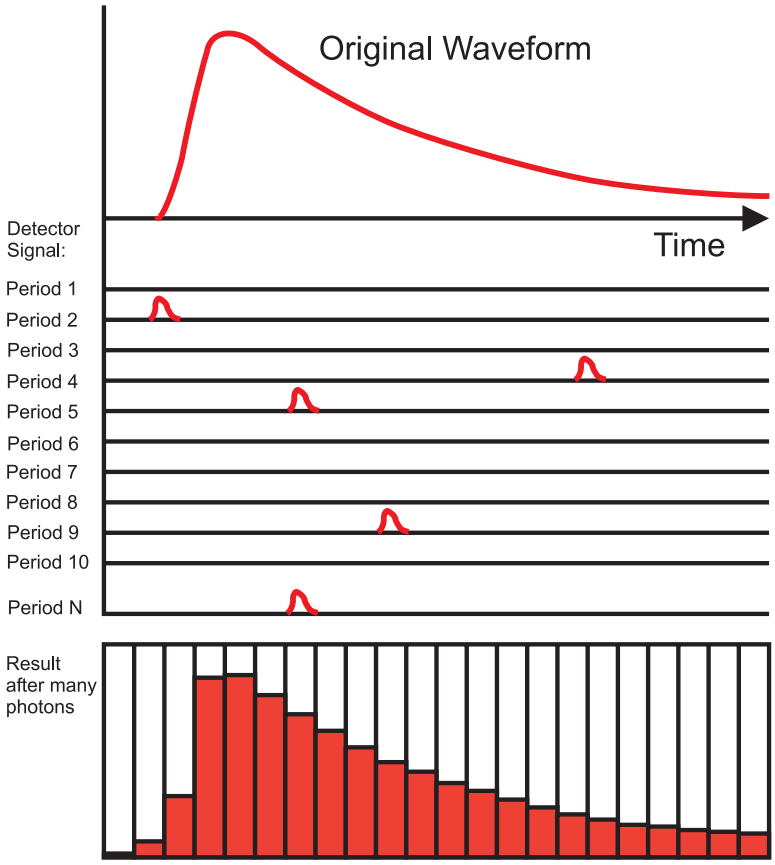


Figure 3.12: An illustration of the principle of time-correlated single photon counting. Repeated sampling of the original waveform allows the construction of a histogram showing the number of photons detected in each time channel. The histogram resembles the original waveform. Re-drawn from (20).

single photon is detected, and for a very few periods, more than one photon is detected. The TCSPC control unit can be *synchronized* with a reference pulse corresponding to the pulsed output of the laser used for excitation. Hence when a photon is detected, it is possible to deduce the time delay relative to the reference pulse. After many photons have been detected, a histogram of the detection times relative to the laser pulse can be built up. This corresponds to the waveform of the original optical pulse. This measurement principle is illustrated in Figure 3.12.

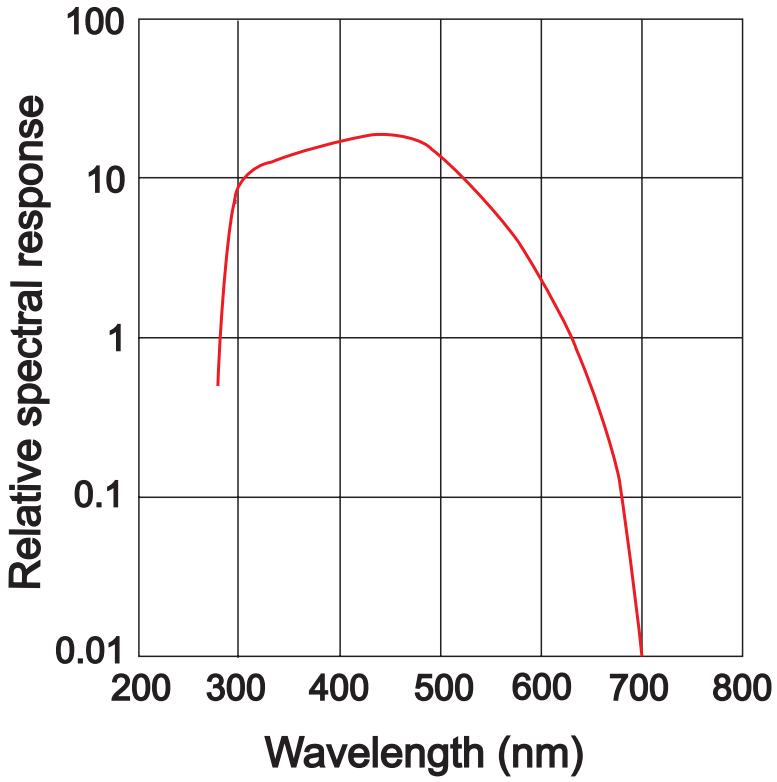


Figure 3.13: A plot of the relative spectral response of the high-speed PMT used for time-correlated single photon counting measurements. The detector was optimized for the wavelength range 300–650 nm. Re-drawn from (21).

3.6.3 Apparatus for time-correlated single photon counting

In this work, a commercial *Becker & Hickl* TCSPC system was used for time-resolved measurements. This used a high-speed photomultiplier tube (PMT) (Model PMH-100-0), optimized for detecting photons in the wavelength range 300–650 nm (the spectral response is shown in Figure 3.13). The PMT was controlled by an 'SPC-630' module installed in the card slot of a PC running the software package 'Multi SPC'. Synchronization with pulses from the laser used for excitation was achieved using a fast photodiode module (Model PHD-400-N) with a rise time of less than 200 ps. The spectral and temporal responses of the photodiode are shown in Figure 3.14.

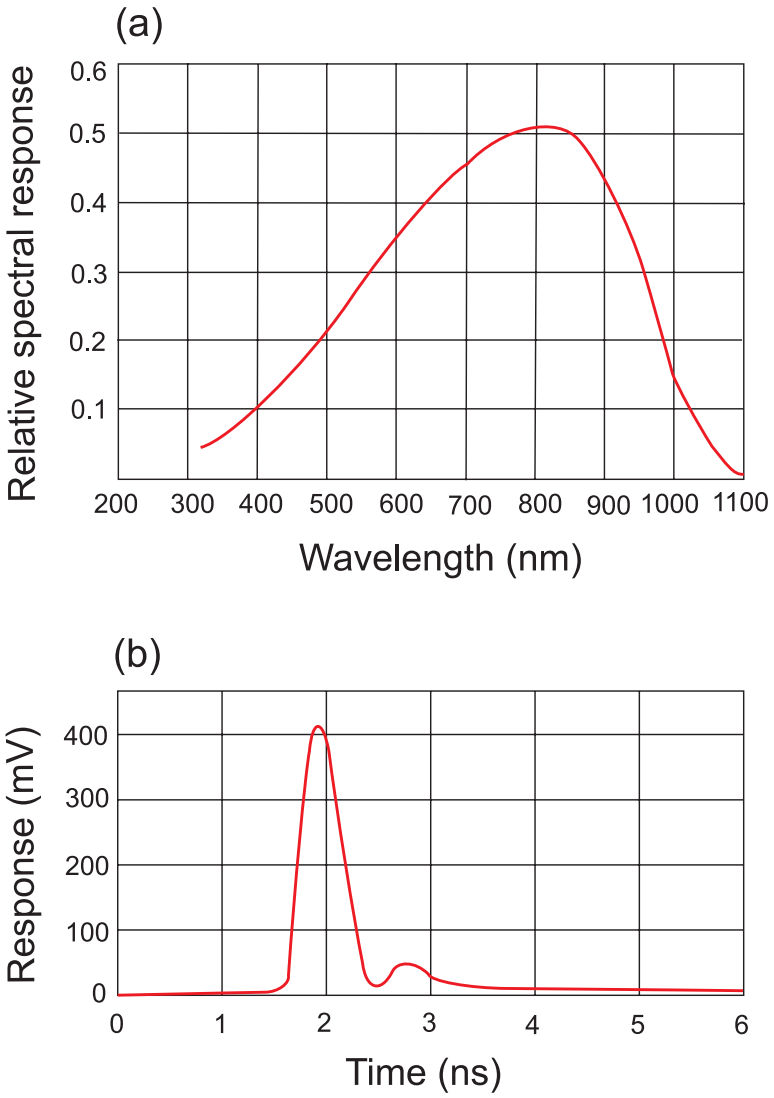


Figure 3.14: The (a) spectral and (b) temporal response of the high-speed photodiode module used for synchronization of the time-correlated single photon counting system. As can be seem from (a), the photodiode was sensitive over a broad wavelength range centred on the fundamental Ti:Sapphire laser output at ∼800 nm. (b) The rise time was less than 200 ps. Redrawn from (22).

Following detection of a photon by the PMT, the constant fraction discriminator (CFD) circuit in the 'SPC-630' module delivered an output pulse correlated with the temporal location of the detector pulse. Synchronization with incoming laser pulses was achieved using the SYNC circuit (with input from the photodiode), which generated a train of electrical pulses corresponding to the laser output. The time-to-amplitude converter (TAC) determined the temporal position of a detected photon within the SYNC pulse train. When the TAC was started by a pulse at the start input, it generated a linear ramp voltage until a stop pulse appeared at the stop input. Thus the TAC generated an output depending linearly on the temporal position of the photon.

The TAC signal was amplified and fed to the analogue-to-digital converter (ADC). This converted the signal to an address in the computer memory, proportional to the temporal position of the photon within the SYNC pulse train. When a photon was detected, the content of the addressed memory location was increased by a fixed increment. Thus over time the memory built up a curve corresponding to a time-resolved trace from the system under study.

The response of the TCSPC system to a single pulse from the Ti:Sapphire laser used for excitation is shown on a logarithmic scale in Figure 3.15. Since the temporal width of the laser pulse was less than 100 fs, the width of the main peak (FWHM $\sim$200 ps) is determined by the detector response. The secondary peak at $\sim$2.1 ns is due either to reflections or to 'ringing' in the detector. The existence of this secondary peak does not pose a serious experimental problem because it is much less intense than the main peak, and is easily swamped when there is a significant count rate at 2.1 ns (as is the case with the relatively long-lifetime processes occurring in QDs).

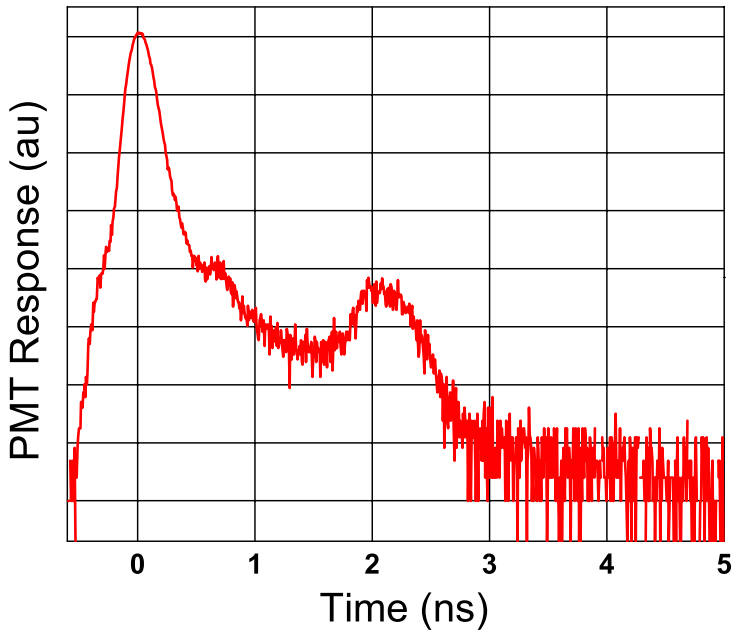


Figure 3.15: The experimentally-measured response of the time-correlated single photon counting system to a single Ti:Sapphire laser pulse, plotted on a logarithmic scale. The FWHM of the main peak is ∼200 ps.

3.7 Summary and conclusion

In order to study the properties of single QDs, μ-PL spectroscopy must be used. This means that the laser beam used for sample excitation is focused down to a small spot size using an optical microscope system. In addition, either mesas or sample masking may be employed in order to further reduce the number of QDs which are illuminated. In this work, μ-PL measurements with a relatively low spectral resolution were made using a commercial μ-PL system, but a second μ-PL system was designed and constructed for measurements with a higher spectral resolution. Sample masking was used to allow single-QD measurements.

The CW He-Cd laser, ultrafast Ti:Sapphire pulsed lasers, ultrafast harmonic generation system, continuous-flow helium cryostat, spectrometers, CCD detector and time-correlated single photon counting system used in this work were all standard, commercially-available

systems.

References

[1] He-Cd laser user information, *Kimmon Electric Co., Ltd.*

[2] 'Laser Fundamentals', W. T. Silfvast, CUP (1996).

[3] 'Femtosecond Laser Pulses: Principles and Experiments', C. Rullière (Ed.), Springer-Verlag (1998).

[4] 'Optics', E. Hecht and A. Zajac, Addison-Wesley (1974).

[5] Kwangseuk Kyhm, DPhil Thesis, University of Oxford (2001).

[6] 'Mai Tai: Diode-Pumped, Mode-Locked Ti:Sapphire Laser', *Spectra-Physics Lasers* (user manual).

[7] 'Operator's Manual: Verdi V-8/V-10 Diode-Pumped Lasers', *Coherent* (user manual).

[8] 'Operator's Manual: The Coherent Mira Model 900-F Laser' *Coherent* (user manual).

[9] 'Optoelectronics and Photonics: Principles and Practices', S. O. Kasap, Prentice Hall (2001).

[10] 'Ultrafast Harmonic Generation System: Model 5-050', *INRAD* (user manual).

[11] K. Brunner, U. Bockelmann, G. Abstreiter, M. Walther, G. Böhm, G. Tränkle and G. Weimann, *Phys. Rev. Lett.* **69**, 3216 (1992).

[12] J.-Y. Marzin, J.-M. Gérard, A. Izraël, D. Barrier and G. Bastard, *Phys. Rev. Lett.* **73**, 716 (1994).

[13] L. Samuelson, N. Carlsson, P. Castrillo, A. Gustafsson, D. Hessman, J. Lindahl, L. Montelius, A. Petersson, M.-E. Pistol and W. Seifert, *Jpn. J. Appl. Phys.* Part 1 **34**, 4392 (1995).

[14] D. Hessman, P. Castrillo, M.-E. Pistol, C. Pryor and L. Samuelson, *Appl. Phys. Lett.* **69**, 749 (1996).

[15] O. Moriwaki, T. Someya, K. Tachibana, S. Ishida and Y. Arakawa, *Appl. Phys. Lett.* **76**, 2361 (2000).

[16] K. P. J. Williams, G. D. Pitt, B. J. E. Smith, A. Whitely, D. N. Batchelder and I. P. Hayward, *J. Raman Spectroscopy* **25**, 131 (1994).

[17] 'RM series Raman systems options and upgrades', *Renishaw*.

[18] 'Microstat-HiRes: Operator's Handbook', *Oxford Instruments* (user manual).

[19] 'Andor DU420-BR-DD', *Andor* (specifications).

[20] 'Time-Correlated Single Photon Counting Modules; Multi SPC Software', *Becker & Hickl GmbH* (user manual).

[21] 'High Speed PMT Detector Head for Photon Counting', *Becker & Hickl GmbH* (specifications).

[22] 'High Speed Photodiode Module', *Becker & Hickl GmbH* (specifications).

Chapter 4

Theoretical motivation: quantum information processing

4.1 Introduction

All existing computation technology relies upon *classical* information processing. This means that, in today's computers, the representation, manipulation and transmission of information can be described purely in terms of Newtonian mechanics (1).

However, Newtonian mechanics is known not to be the final physical theory of the Universe. Instead, it is merely a limiting case of quantum mechanics. Since the operation of any computing machine is necessarily a physical process, this means that there should be no reason that information processing could not in principle be carried out on the basis of quantum mechanical principles rather than in a classical manner. An information processing device working in this way is known as a *quantum computer* (2; 3; 4).

It would appear that a large-scale quantum computer, if one could ever be built, would offer

enormous advantages over a classical computer for certain computational tasks. There are some tasks requiring enormous amounts of classical processing time which could be performed in far fewer steps using a quantum computer. It is this possibility of huge improvements in processing power compared to classical computers which is responsible for the immense interest in constructing a practical large-scale quantum computer.

4.2 The classical bit versus the quantum bit

The two-level 'bit' is the basic means of representing information in all computer systems. The classical bit is generally physically represented (or 'embodied') in a macroscopic system which can be described in terms of one or more continuous parameters. The designer of the bit associates the values '0' and '1' with particular well-separated regions of the parameter space. In the case of the vast majority of computers in use today, a single parameter is chosen, namely voltage. In this case, the bit is usually defined to be in the 0 state when the voltage is below a certain level, and in the 1 state when the voltage is above this level.

The quantum bit ('qubit') (5), in contrast, is generally embodied in a microscopic system whose behaviour must be described in terms of the laws of quantum mechanics (6). The two states 0 and 1 are now defined in terms of different states of the quantum system and are generally written in *Dirac notation* as $|0\rangle$ and $|1\rangle$ respectively. For example, a qubit could be embodied using two mutually orthogonal polarization states of a photon: one polarization could represent $|0\rangle$, while the other would represent $|1\rangle$. Other physical representations might be the alignment of a nuclear spin in a uniform magnetic field, or two states of an electron orbiting a single atom (7). The important point is that, since the qubit is a quantum

mechanical system, it is free to exist not just in the $|0\rangle$ or $|1\rangle$ states, but in *any possible* superposition of the two states.

A *pair* of qubits is then capable of existing in four boolean states, $|00\rangle$, $|01\rangle$, $|10\rangle$ and $|11\rangle$, but also (according to quantum mechanics) in *all possible superpositions* of these boolean states. Some of these superpositions cannot be described in terms of tensor products of the states of individual qubits. These so-called 'entangled' states correspond to a situation in which neither qubit by itself has a definite state, even though the pair together does.

The possibility of creating entangled states in a quantum computer is responsible for the potentially huge processing power of such a device. In a classical system, n classical bits can exist in any of 2^n boolean states, but in a quantum system, n qubits can exist in a far larger number of superposition states. In fact, the general state of n qubits is specified by a 2^n-dimensional complex vector. All of the states in a quantum computer represented by superpositions of the basic states can, in principle, be manipulated simultaneously. Thus a quantum computer would have enormous *parallelism*.

4.3 The Bloch sphere single-qubit visualization

As noted in Section 4.2, a single qubit can be in a state *other* than the *computational basis states* $|0\rangle$ and $|1\rangle$. In general, the state of a qubit can be described as a linear combination or superposition, of the form

$$|\psi\rangle = \alpha\,|0\rangle + \beta\,|1\rangle\,, \tag{4.1}$$

where α and β are complex numbers. Put another way, the state of a qubit is a vector in a two-dimensional complex vector space.

The measurement of the qubit will yield the value 0, with probability $|\alpha|^2$, or 1, with probability $|\beta|^2$. Naturally, $|\alpha|^2 + |\beta|^2 = 1$, since the probabilities must sum to unity. Geometrically, this can be interpreted as the condition that the qubit's state is normalized to length 1. Thus, in general, a qubit's state is a unit vector in a two-dimensional complex vector space.

Because $|\alpha|^2 + |\beta|^2 = 1$, Equation 4.1 can be re-written as

$$|\psi\rangle = e^{i\gamma}\left(\cos\frac{\theta}{2}|0\rangle + e^{i\varphi}\sin\frac{\theta}{2}|1\rangle\right), \tag{4.2}$$

where θ, φ and γ are real numbers. The factor $e^{i\gamma}$ can be ignored since it has no observable effects (7), and the equation can therefore be effectively expressed as

$$|\psi\rangle = \cos\frac{\theta}{2}|0\rangle + e^{i\varphi}\sin\frac{\theta}{2}|1\rangle. \tag{4.3}$$

The numbers θ and φ define a point on the unit three-dimensional sphere, as shown in Figure 4.1. This so-called *Bloch sphere* provides a useful means of visualizing the state of a single qubit, and many single-qubit operations can be neatly described in this way. For example, single qubit gate operations simply correspond to reflections and rotations of the Bloch sphere.

Nevertheless, it should be pointed out that, while the Bloch sphere visualization is very useful for a single qubit, it is limited in that there is no known simple generalization for multiple qubits.

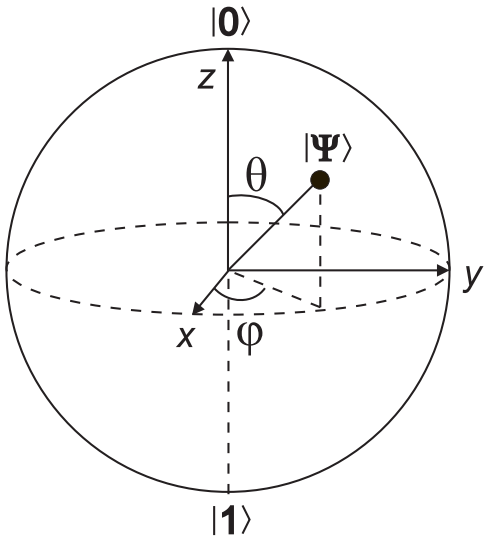


Figure 4.1: The Bloch sphere representation of a qubit.

4.4 Potential advantages of quantum information processing

When the notion of a quantum computer was first proposed, it was not immediately clear how the performance of such a device would differ from that of a classical computer (8). It had been originally believed that the answer to the question of whether any given problem could be solved in a time that was polynomial in the size of its inputs, or greater than polynomial, was independent of the physical apparatus used to perform the computation (9). However, this idea was later shown to be false. Various *quantum mechanical algorithms* were discovered which would allow certain computational tasks to be carried out in far fewer steps (and hence potentially far more rapidly) on a quantum computer than on any classical counterpart.

The first quantum mechanical algorithm which would give a solution *with certainty* in a given time, and which would be absolutely more efficient than any classical method, was

discovered in 1992. This was the Deutsch-Jozsa algorithm (10). Unfortunately, the Deutsch-Jozsa algorithm, while being theoretically very significant, actually solves a mathematical problem of little practical use.

The first computationally *useful* quantum mechanical algorithm to be discovered was Shor's factorization algorithm (11), first identified in 1994. This would be exponentially faster than any known classical factorization algorithm. Shor's factorization algorithm was mathematically very interesting since mathematicians had unsuccessfully been searching for efficient factorization algorithms for a long time. Moreover, many commonly-used cryptographic codes, such as the Rivest-Shamir-Adleman (RSA) cryptosystem (12), rely on the assumption that the factorization of a large number would require an extremely large amount of computing time, and therefore that such codes are, for all practical purposes, unbreakable. In contrast to a classical device, a large-scale quantum computer would easily be able to defeat a cryptographic code of this type.

A second useful quantum mechanical algorithm, the Grover algorithm, was discovered in 1996 (13). This algorithm could be used to rapidly search a database of n items for a single item satisfying a given condition. The number of steps required would scale as $\sqrt{n}$, in contrast to all known classical algorithms, for which the scaling would be linear in n. Given a sufficiently large database, the Grover quantum mechanical algorithm would clearly be vastly superior to any classical algorithm.

A third computational task for which a quantum computer would offer superior performance compared to a classical computer is the simulation of a many-particle quantum mechanical system (14). The speed-up in this case could be as rapid as exponential (6).

Despite the discovery of these quantum mechanical algorithms, it is now known that there is also a broad class of computational tasks which would not be sped up at all by using quantum information processing rather than classical information processing. It is clear that a large-scale quantum computer would be able to offer speed advantages in solving only a fairly limited range of problems. Nevertheless, the performance increase in these cases would potentially be so large that it would still seem to be well worth trying to build a large-scale quantum computer.

4.5 Requirements for the physical implementation of quantum information processing

Researchers now agree that there are various fundamental physical requirements which any large-scale quantum computer must fulfill. A widely-accepted formulation of these requirements in terms of five basic criteria was proposed by DiVincenzo (1) in 2000, and may be summarized as described in this section.

4.5.1 Well-characterized qubits and scalability

A qubit is generally embodied using two levels of a quantum mechanical system. One of the levels is defined as being associated with the qubit state $|0\rangle$, and the other is defined as being associated with $|1\rangle$. That the qubit is 'well-characterized' means that its physical parameters are accurately known. This includes the internal Hamiltonian (which determines the energy eigenstates of the qubit), the presence of and couplings to other states of the

qubit, the interactions with other qubits, and the couplings to external fields that might be used to manipulate the state of the qubit.

The system must be *scalable* to a large number of qubits if a large-scale quantum computer is to be constructed. In practice, a large-scale device would probably require several thousand qubits.

4.5.2 Ability to prepare fiducial initial states

It must be possible to initialize the state of the qubits to a simple fiducial state. This first reason for this requirement is the simple fact that, in any computational scheme (even a classical one), it must be possible to prepare the desired input. This is because, naturally, it will only be possible to carry out a computation provided that the information required by the computer can be entered correctly.

It should be noted that in a quantum computer it will only be necessary to be able to (repeatedly) produce one specific quantum state with high fidelity, since a unitary transform can be used to turn it into any other desired input state. For example, being able to put n qubits into the $|00\ldots0\rangle$ state is good enough.

There is a second reason for the initialization requirement. Schemes for quantum error correction require a continuous, fresh supply of qubits in a low-entropy state (such as $|0\rangle$). Unfortunately, this necessity may pose serious problems for some proposed schemes for quantum computing. Arranging a continuous supply of qubits in the $|0\rangle$ state, rather than just an initial supply, may prove difficult.

4.5.3 Long decoherence times

As discussed in more detail in Section 4.6, any qubit must necessarily have some degree of contact with its environment. Over time, interactions between the qubit and its environment will cause the qubit to lose its phase coherence. The characteristic time over which this occurs is known as the *decoherence time*. Simply understood, this would be characteristic time for a general qubit state $|\psi\rangle = a|0\rangle + b|1\rangle$ to be transformed into the mixture $\rho = |a|^2 |0\rangle\langle 0| + |b|^2 |1\rangle\langle 1|$ (1).

The problem of decoherence is a very serious one in quantum computing. Over long enough timescales, the state of a qubit would effectively become randomized. This would cause the qubit to lose the quantum information it carries, preventing the quantum computer from carrying out its calculation successfully.

It might be thought that the minimum decoherence time necessary to perform a successful quantum computation would scale with the duration of the computation. If this were the case, a quantum computer would either be restricted to extremely short computations, or would have to consist of qubits with a very long decoherence time. Fortunately, it is now known that *error correction* of quantum states is possible, and that this correction procedure can be applied in quantum computing. (This is discussed in more detail in Section 4.6.) The use of quantum error correction gives rise to much more reasonable requirements on the decoherence time.

4.5.4 A 'universal' set of quantum gates

It can be shown that a small set of gates can be used to compute an arbitrary classical function. Such a set of gates is said to be *universal for classical computation*. A similar universality result is true for quantum computation, where a set of gates is said to be *universal for quantum computation* if any unitary operation may be approximated to arbitrary accuracy by a quantum circuit involving only those gates.

It can be shown that any unitary operation on n qubits can be approximated to arbitrary accuracy using the so-called Hadamard, phase, controlled-NOT (CNOT) and $\pi/8$ gates (7). This set of gates is known as the *standard set* of universal gates for quantum computation. Of the four gates comprising the standard set, only the CNOT gate is a two-qubit gate; the rest all operate on just one qubit.

Any proposed scheme for implementing quantum information processing must therefore demonstrate a means of realizing these gates. It is usually relatively straightforward to implement one-qubit gates (the Hadamard, phase and $\pi/8$ gates) using externally-applied control pulses; but an important requirement for any proposed scheme for quantum computing will be the ability to realize a CNOT gate.

4.5.5 A qubit-specific measurement capability

It must be possible to 'read out' the result of a quantum computation, and this requires the ability to correctly measure specific qubits. In practice, the fidelity of reading out a quantum state will be less than perfect: each such measurement can be described in terms of a 'quantum efficiency'. It may still be possible to successfully read out the result of a

quantum computation even when the quantum efficiency is less than 100%. This can be achieved by encoding the output state (before it is read) into an entangled state of a number of other qubits, then individually measuring the states of all these qubits. Even if there is an error in reading out some of the qubits, it should still be possible to read out the correct state provided that sufficient copies were made. This process does not violate the well-known principle that unknown quantum mechanical states cannot be 'cloned'. Triple repetition, for example, should be viewed not as the making of three copies of the input qubit ($\psi \rightarrow \psi \otimes \psi \otimes \psi$), but rather as the mapping $\alpha |0\rangle + \beta |1\rangle \rightarrow \alpha |000\rangle + \beta |111\rangle$, which does not violate any quantum mechanical principle (6).

4.6 Quantum error correction

All physical systems are subject to random fluctuations (15). First consider those degrees of freedom which may be described in terms of classical mechanics. In practice, it is possible to stabilize classical degrees of freedom to a very large degree. This can be done either *passively* (by making the size of the system very large compared to the size of the perturbation) or *actively*, by continuously monitoring the system and applying negative feedback against system fluctuations.

Next, consider a system which may be described in terms of quantum mechanics. Passive stabilization can still be applied in this case, but there are limits to this since the system cannot be enlarged too much, or it will cease to behave in a quantum mechanical way. Some sort of active stabilization is likely to be necessary in order to reduce the effect of random fluctuations in such a system.

In the case of a qubit, active stabilization against random fluctuations will be extremely important. If left unchecked, fluctuations could change the state of the qubit, resulting in computational errors in the quantum computer of which it forms a part. This is the problem of *decoherence* which was briefly discussed in Section 4.5.3. If left uncorrected, decoherence would render useful quantum computation impossible.

All decoherence in a quantum computer is due to unwanted interactions of qubits with their environment. The process of stabilizing the system against these environmental perturbations is known as *quantum error correction*. This is analogous to classical error correction, which is used widely in today's classical computers.

Various quantum error-correcting codes (QECC) have been devised. These protect quantum information against noise. The simplest QECCs are based on the principle of encoding an arbitrary qubit into an entangled state of a number of other qubits. The basic principle here is redundancy: even if some of the information encoded is lost due to noise, it should still be possible to extract the original information (the state of the first qubit). Unfortunately, simple approaches of this type suffer from the problem that the error correction operations would themselves have to be perfect (completely free of errors) in order for the error correction procedure to work correctly. In practice, this is unlikely to be possible since the quantum error correction would just be provided by additional qubits in the same system, which would be just as susceptible to errors as the qubits they should be correcting.

This problem has apparently been solved by the advent of quantum fault-tolerant computation (QFTC) schemes, in which error correction can, in principle, be achieved even when the corrective operations are themselves imperfect. Moreover, some recently-proposed schemes for implementing QFTC should work much more efficiently than early QECC: far fewer ad-

ditional qubits would be required as an 'overhead' for the error-correction process. In fact, it can be shown that in order to perform a t-step computation fault-tolerantly, the number of gates and wires need only be multiplied by a factor polynomial in $\log t$ (6). This means that, for computations with a significant quantum speed-up, a fault-tolerant quantum computer would still vastly outperform any classical computer on sufficiently large inputs, despite the necessity for the 'overhead' of error-correction qubits.

Thanks to efficient QFTC, it now appears that the problem of decoherence should not constitute an insurmountable barrier to realizing large-scale quantum information processing. The *threshold theorem* states that, provided the rate of decoherence is kept below a certain threshold (which will depend on the detailed physical properties of the system), it will be possible to efficiently perform an arbitrarily large quantum computation. If the rate of the processes tending to lead to decoherence rises above the threshold, however, then the error correction system will be overwhelmed and accurate computation will become impossible.

Calculations show that it should be possible to implement fault-tolerant quantum computation provided that the decoherence time is at least $10^4 - 10^5$ times greater than the 'clock time' of the quantum computer, where the 'clock time' is the time required for the execution of an individual quantum gate (1). Once this threshold is reached, it should be possible to perform arbitrarily long quantum calculations, even in the presence of decoherence.

4.7 Practical realizations of quantum information processing

Realizing quantum information processing in real physical systems has been found to be extremely challenging. Experimentalists *have* been able to successfully demonstrate working quantum computers containing a few qubits; it has even been possible to experimentally implement simple quantum algorithms. Unfortunately, it seems that all the systems in which this small-scale quantum computing has so far been achieved will be difficult to scale beyond a few qubits. Some of the most promising approaches are reviewed in this section.

4.7.1 Nuclear magnetic resonance schemes

One of the leading approaches in the field of experimental quantum computing currently appears to be that based on nuclear magnetic resonance (NMR). NMR techniques make use of a liquid sample consisting of molecules of a carefully-chosen type dissolved in a solvent. A typical molecule which might be used would contain n protons, each having spin 1/2, and would produce an NMR signal at about 500 MHz when placed in a magnetic field of about 11.7 T (7). The frequencies of different nuclei within a molecule would be expected to differ by between a few kHz and several hundreds of kHz because of differences in the local magnetic fields due to chemical environment shielding effects. Since the molecules would be dissolved in a solvent, inter-molecular interactions would become negligible. This would leave a system that could be considered as an ensemble of individual n-qubit 'quantum computers'.

The liquid sample is contained within an NMR spectrometer. The spectrometer uses a large superconducting magnet to generate a strong, constant B-field which is highly uniform throughout the sample volume. Orthogonal Helmholtz coils lying in the transverse plane allow small, oscillating magnetic fields to be applied at right angles to the direction of the constant B-field. These small fields can be rapidly pulsed on and off to manipulate nuclear spin states, generating arbitrary transforms. Couplings between spins are provided by the chemical bonds between neighbouring atoms.

In order to 'read out' the result of a quantum computation in an NMR-based scheme, the experimenter measures the voltage signal induced by the precessing magnetic moment. The result will be a mean value from the whole ensemble of molecules in the solution. This means that computational errors will not be fatal provided that they are restricted to a relatively low level; quantum error correction in a small NMR quantum computer is therefore not essential.

NMR-based quantum computing techniques have been successfully used to experimentally implement various quantum algorithms. The first quantum algorithm to be successfully implemented was the simplest version of the Deutsch-Jozsa (D-J) quantum algorithm (16). This was followed by an implementation of Grover's quantum search algorithm (17). But the most impressive demonstration of quantum information processing using the NMR-based technique was the successful use of Shor's algorithm, on a seven-qubit quantum computer, to factorize the number 15 (18). This remains by far the most advanced realization of experimental quantum computing to date.

Unfortunately, NMR-based schemes in their current form are apparently not scalable beyond a few qubits (6). One reason for this is that, under current implementations, the readout

signal reduces exponentially in the number of qubits. Another problem is that the frequency-domain addressing which is used, in which each qubit has a distinct chemical shift ω_i, becomes difficult when the number of qubits grows large. It may be possible to solve these problems eventually, but for now NMR-based schemes are restricted to less than around ten qubits.

4.7.2 Ion-trap schemes

Another promising approach is that based on ion-trap schemes. In these schemes, ions are cooled to the recoil limit (very close to absolute zero) via laser cooling and then further via sideband cooling, such that $k_B T \ll \hbar\omega_z$ (7). These cooled ions are then confined in an ion trap in the centre of a potential created by four cylindrical electrodes. The apparatus is typically contained in a high vacuum; modulated laser light incident on the ions through windows in the vacuum chamber performs operations on the atomic states, and is used to read them out.

According to the quantum computer architecture proposed by Cirac and Zoller (19), qubits are associated with internal (hyperfine) states of the ions, and information is transferred between qubits through a shared motional degree of freedom. Due to the high degree of isolation of the ions from their environment, decoherence in such a system should be negligible; moreover, it should be relatively easy to scale up the computer to a large number of qubits.

Ion-trap quantum computers have been used to realize a two-qubit quantum logic gate (20), and to implement the Deutsch-Jozsa algorithm (21).

4.7.3 Other schemes

Other researchers are investigating the possibility of realizing quantum information processing using a variety of other schemes. These include the optical photon quantum computer, proposals based on electron magnetic resonance spectroscopy, schemes based on optical cavity quantum electrodynamics, superconductor-based approaches, schemes using optical lattices and others using Bose condensates. There are also proposals based on using excitons confined in QDs, which are discussed in more detail in Section 4.8.

4.8 Quantum information processing using quantum dots

4.8.1 Conventional approaches

A workable, large-scale quantum computer would probably require several thousand qubits. It currently appears that a quantum computer of this size is more likely to be built using solid-state technologies such as semiconductor QDs than by other proposed schemes (22). This is because non-solid-state approaches seem to suffer from serious problems with scalability when it comes to realizing large numbers of qubits. In contrast, any scheme based on solid-state hardware, such as QDs, is likely to be intrinsically scalable. In the case of QDs, very large numbers can be produced on a single substrate relatively easily. This can be done either via selective growth techniques or by self-assembly. Both techniques are relatively well-developed experimentally.

It would appear that QDs may in fact be very well suited for quantum computing applications. The quantized, atom-like energy structure of QDs allows for a weak interaction of the QD system with environmental degrees of freedom such as phonons (23). This implies that the quantum evolution of a QD system enjoys a low rate of decoherence, a very useful property for quantum computing applications.

A considerable number of QD-based quantum computing schemes have been suggested. The first such scheme to be proposed was that described by Loss and DiVincenzo in 1998 (24). This used the spin states of coupled single-electron QDs to embody the $|0\rangle$ and $|1\rangle$ states of the qubit. Desired operations are effected by the gating of the tunnel barrier between neighbouring QDs.

Unfortunately, spin-based schemes seem to suffer from the problem that the decoherence time would not be sufficiently long compared to the switching time for even fault-tolerant quantum computing to be successfully carried out (25). Therefore, several other schemes have been proposed which instead rely upon the gating of *charge* excitations. Using ultrafast laser technology, it is possible to generate electron-hole quantum states in QDs on a sub-picosecond timescale, and to perform on such states a variety of coherent-carrier-control operations.

The first scheme for charge-based quantum computing using QDs was that proposed by Zanardi and Rossi in 1998 (25). This proposal for the first time envisaged the use of an array of QDs as a register for information encoding.

In this early scheme, and in some others (26; 27), single-qubit operations are implemented by means of ultrafast optical spectroscopy. Unfortunately, the control of two-qubit operations

in these implementations still involves the application of time-varying external electric fields and/or microcavity-mode couplings. From a technological point of view, this would require the presence of electrical contacts which would seriously limit the time response of the system and strongly complicate the physical interconnection of the device. Indeed, the switching time of the external electric field would probably be much longer than the decoherence time of the exciton in the QD.

A proposal for so-called *all-optical* quantum computing with QDs was put forward by Biolatti *et al.* in 2000 (28). This strategy exploits exciton-exciton interactions driven by ultrafast, multi-colour laser pulses. An external electric field *is* still required, but this is now static rather than time-varying, thus removing the problem with the relatively long switching time for such fields. The external field serves to induce dipoles in the QDs when excitons are present, thus giving rise to dipole-dipole interactions between excitons in adjacent QDs. Coulomb interactions between exciton dipoles in QDs are therefore the mechanism for the qubit-qubit interactions which are essential in any quantum computer.

4.8.2 Experimental realization of a quantum-dot-based quantum logic gate

As well as the various proposed schemes for large-scale quantum information processing with QDs, a simple QD-based two-qubit quantum logic gate has actually been experimentally implemented (29; 30).

The quantum gate was realized via coherent optical control of *two* excitons (a 'biexciton') confined in a single GaAs QD. Each of the excitons in the single QD was used to embody a

qubit. For each qubit, the values $|0\rangle$ and $|1\rangle$ respectively were used to represent the absence or presence of the exciton. The two-qubit system levels therefore consisted of the ground state $|00\rangle$, two *distinguishable* exciton states $|01\rangle$ and $|10\rangle$ with orthogonal polarizations, and the biexciton state $|11\rangle$.

The experimenters were able to demonstrate operation of the system as a so-called controlled-rotation (CROT) gate. In a CROT gate, the relative amplitudes for a superposition of $|0\rangle$ and $|1\rangle$ in a 'target' qubit depend on the logical state of a separate 'control' qubit. The gate does nothing if the control qubit is in the state $|0\rangle$, but if the control qubit is in the state $|1\rangle$, the amplitudes of the logical states for the controlled qubit are interchanged.

Laser pulses tuned to different wavelengths were used to generate Rabi oscillations both between the ground state and the exciton states, and between the exciton and biexciton states. The operation of the gate could be controlled using an 'input' laser pulse, which determined the state of the control qubit, and an 'operational' laser pulse, which would flip the state of the target qubit provided that the control qubit was in the correct quantum state. The operational pulse for the CROT gate was chosen to be a π pulse tuned to the $|10\rangle \leftrightarrow |11\rangle$ transition. If the input of the gate was $|00\rangle$, the operational pulse would be off-resonant and the output would remain $|00\rangle$. If the input was $|01\rangle$, the operational pulse would have the wrong polarization (because of the orthogonal polarizations of the exciton states) and the output would not change. However, when the input was $|10\rangle$, the operational pulse rotated this to give $-|11\rangle$. Similarly, if the input was chosen to be $|11\rangle$, the operational pulse would cause it to change to $|10\rangle$.

The truth table of the CROT gate was 'mapped out' experimentally. Due to decoherence, the gate operation was less than perfect. The experimentally-measured fidelity of the gate

was found to be approximately 0.7.

Unfortunately, this simple implementation of a quantum logic gate is intrinsically unscalable since it uses two excitons in a single QD. Controlling more than two excitons in the QD would be difficult, and reaching numbers sufficient for large-scale quantum information processing would be unworkable. Scalable schemes must demonstrate entanglement between excitons in *different* QDs rather than within a single QD. Nevertheless, this work is an interesting demonstration that a QD-based quantum logic gate can work in principle.

4.8.3 Global addressing

An apparent problem in operating a quantum computer consisting of a large array of QDs might be the difficulty of manipulating *individual* qubits. The QDs, in which the qubits are embodied, could well be very close together; the QD-QD separation might be considerably less than the wavelength of the laser radiation used for control. This would rule out the possibility of using spatial selection techniques to address individual qubits.

Fortunately, it has been shown that a quantum computer could still operate successfully even without local addressing. It has been shown that it would sufficient to apply only *global* manipulations, to which all the elements are subjected simultaneously.

A global addressing scheme of this type was devised by Benjamin in 2000 (31). This scheme envisages two types of cell, A and B, alternating along a one-dimensional array. Each cell has two internal eigenstates, $|\downarrow\rangle$ and $|\uparrow\rangle$, and can represent any quantum superposition of these states. A qubit of quantum information is represented by *four* consecutive cells, and each pair of qubits must be separated by at least four spacer cells in the $|\downarrow\rangle$ state. The array

is subject to 'update' rules specified by the notation $A_f^{\mathbf{U}}$ which means that each cell of type A is subjected to unitary transform **U** if, and only if, its 'field' has the value f. The 'field' is defined as the number of nearest neighbours in state $|\uparrow\rangle$ minus the number in state $|\downarrow\rangle$.

A quantum computer must have the ability to apply a chosen unitary transform to a particular qubit without affecting the other qubits. In Benjamin's scheme, one qubit is 'singled out' through the use of a 'control unit' (CU). The CU is a certain pattern of states which exists only in one place along the array. The application of the correct update sequence will now perform a gating operation only on the qubit in the vicinity of the CU. By applying various other update sequences, a different qubit could be transformed, or the CU could be moved without altering any of the qubits. Thus a general one-qubit gate can be implemented.

To implement a two-qubit gating operation, the 'control-**U**' is used. This gate applies the transform **U** to a certain qubit (the 'target') if, and only if, a second qubit (the 'control') is in state $|1\rangle$. Through the use of the control-**U** two-qubit gate, and various one-qubit gates, a 'universal' set of quantum gates can be realized. Moreover, through the use of several CUs, gating operations can be applied at several points in the array simultaneously.

Benjamin's scheme is useful in that it requires only global addressing. It may therefore be of considerable help in constructing a functioning QD-based quantum computer if local addressing becomes very difficult or impossible.

4.8.4 Approaches based on nitride quantum dots

In Section 4.8.1, a scheme proposed by Biolatti *et al.* (28) for scalable all-optical quantum computing with QDs was discussed. This would not require the application of time-varying

external electric fields. However, as discussed it *would* still require the application of a *static* external field to induce dipoles in the QDs when excitons were present.

It has been pointed out that this requirement could be circumvented through the use of a semiconductor material which exhibits a strong *internal* electric field. As discussed previously, nitride semiconductors have a strong 'built-in' electric field induced by the spontaneous and piezoelectric polarizations. Relying on this fact, a scheme for GaN QD-based quantum computing has been proposed by D'Amico *et al.* (32; 33; 34). Such an architecture would negate the requirement for the application of any external electric fields.

The scheme of D'Amico *et al.* may be described as follows. The physical hardware of the quantum computer consists of an array of pairs of vertically-stacked nitride QDs. Two-QD systems grown epitaxially can be tailored in such a way that the lower QD is smaller than the upper QD, due to the overlap of the strain fields, or such that the two QDs have identical base diameter but slightly different height, thanks to control of the deposition rate and III-V ratio. In both cases, the potential of the two QDs is engineered to control the splitting of the respective ground levels, thus allowing selective optical excitation of one of the two QDs by ultrafast laser pulses.

Each QD is used to embody a qubit. The basis states $|1\rangle$ and $|0\rangle$ of the qubit correspond respectively to the presence or absence of a ground-state exciton in the QD.

The internal electric field in the nitride QDs is correctly tailored (again by slightly adjusting the size of the QDs) such that internal, built-in exciton dipoles are induced: this provides the mechanism for interactions between excitons in the upper and lower QDs in each vertical stack. The vertical separation is chosen to prevent single-particle tunnelling between the two

QDs, but to allow at the same time significant dipole-dipole Coulomb coupling – and hence qubit-qubit interactions.

Consider QDs a and b, which form a single vertical stack. Because of dipole-dipole interactions between excitons in the two QDs, the exciton transition energy in b will depend upon whether or not a contains an exciton. Theoretical modelling suggests that this energy difference will be of the order of several meV. This now raises the obvious possibility of using the two QDs to realize a *conditional* quantum logic gate. Laser pulses tuned to two different energies can be used to achieve this. The laser wavelength could be tuned to be resonant with the exciton transition energy of b when a contains an exciton. In this case, the laser pulse will only cause manipulations of the state of b when a is occupied. If a does not contain an exciton, then b will not be affected by the laser pulse since the energy of the exciton transition will now be detuned from the laser wavelength. This means that if the laser pulse performs a π operation, for example, then the system will function as a CNOT gate: the state of the b is changed if and only if a is in the state $|1\rangle$.

An important point is that, since the 'biexciton' energy splitting will be quite large (of the order of several meV), a laser pulse with a relatively large frequency bandwidth can be used. This, via the Uncertainty Principle, implies that an ultrafast pulse would be acceptable: a pulse on the sub-picosecond timescale would be expected to be suitable. This means that it should be possible to perform a relatively large number of elementary operations within the exciton decoherence time.

Schemes similar to that of Biolatti *et al.*, working upon the basis of exciton-exciton interactions, may offer real promise in realizing scalable quantum computing. Nevertheless, there are still numerous difficulties to be overcome. Firstly, it is necessary to be able to fabricate

high-quality, regularly-spaced, uniform QDs. This is difficult, especially in nitride systems. SK growth techniques *have* been successfully used to produce high-quality, uniform nitride QDs. However, achieving regular spacing has been more difficult: vertical 'stacking' of QDs (in the z-direction) with a regular separation has proved experimentally elusive. A second problem is producing QDs which have a sufficiently long exciton decoherence time to permit the required ratio between decoherence time and gating time (probably $10^4 - 10^5$) to be achieved. Efforts are being made to achieve this through improved growth techniques.

Provided that the problems discussed above can be resolved, it is possible to see how a QD-based quantum computer of this type might fulfill the five criteria discussed in Section 4.5. Firstly, a qubit could be robustly embodied using the presence or absence of excitons in a QD: the absence of an exciton might correspond to the state $|0\rangle$, for example, while the presence of an exciton might correspond to the state $|1\rangle$. Scalability could be achieved relatively easily using semiconductor growth techniques. Secondly, the qubits could be initialized in the $|0\rangle$ state by simply allowing them to decay to their ground state: this would probably require at most a few tens of ns. Thirdly, sufficiently long exciton decoherence times may be achievable through improvements in QD fabrication techniques. Fourthly, the CNOT gate, necessary for achieving a universal set of quantum gates, could be achieved through allowing closely-spaced QDs to interact via the Coulomb interaction. Fifthly, qubits could be read out optically.

4.9 Summary and conclusion

Quantum information processing is a large, diverse and rapidly-growing field. As we have seen, the idea of representing and manipulating information in a quantum mechanical way rather than classically could offer huge speed advantages for certain computational tasks. Unfortunately, any computer designed to work quantum mechanically would have to meet a very challenging set of physical requirements. One of the most serious problems is that of decoherence, the tendency of quantum information to be lost due to interactions of qubits with their environment. To overcome this difficulty, a range of error-correction schemes have been proposed, including some which are tolerant to faults in the error-correction process itself. The use of such schemes would make it possible to perform fault-free quantum computations provided that the rate of decoherence was kept below a certain threshold.

Despite the difficulty of building a quantum computer, there have already been a number of experimental demonstrations of machines consisting of a few qubits; some of these devices have even been used to implement simple quantum algorithms. Schemes based on nuclear magnetic resonance and on ion traps seem to have produced the best results so far, but such architectures unfortunately appear not to be scalable to the large numbers of qubits which would be required for a large-scale quantum computer.

An alternative set of schemes which seem to hold out more hope of scalability are those based on semiconductor QDs. The manufacturing processes required for fabricating large arrays of QDs are relatively well understood. But although a simple quantum logic gate has been demonstrated on a quantum-dot-based device, QD schemes are still in an early stage of development. One problem with the QD approach is the necessity, in many schemes, of

using rapidly-switched electric fields. This could seriously slow down the operation of the computer and would heavily complicate its architecture. A solution to this might lie in the use of nitride QDs which, with their strong internal electric fields, would not require the application of external electric fields.

There is no doubt that steady progress is being made in the field of quantum information processing, from both theoretical and experimental viewpoints. Nevertheless, there seems to be a very long way to go before a large-scale (and useful) quantum computer can be constructed.

References

[1] D. P. DiVincenzo, *Fortchr. Phys.* **48**, 771 (2000).

[2] D. Deutsch, *Proc. R. Soc. Lond. A* **400**, 97 (1985).

[3] D. Deutsch, *Proc. R. Soc. Lond. A* **425**, 73 (1989).

[4] S. Lloyd, *Science* **261**, 1569 (1993).

[5] B. Schumacher, *Phys. Rev. A* **51**, 2738 (1995).

[6] C. H. Bennett and D. P. DiVincenzo, *Nature* **404**, 247 (2000).

[7] M. A. Nielsen and I. L. Chuang, 'Quantum Information and Computation', Cambridge University Press (2000).

[8] L. K. Grover, *Science* **281**, 792 (1998).

[9] D. P. DiVincenzo, *Science* **270**, 255 (1995).

[10] D. Deutsch and R. Jozsa, *Proc. R. Soc. Lond. A* **439**, 553 (1992).

[11] P. W. Shor, in *Proceedings of the Symposium on the Foundations of Computer Science, 1994, Los Alamitos, California* (IEEE Computer Society Press, New York, 1994).

[12] R. L. Rivest, A. Shamir and L. M. Adleman, *Communications of the ACM (2)* **21**, 120 (1978).

[13] L. K. Grover, *Phys. Rev. Lett.* **79**, 325 (1997).

[14] D. S. Abrams, *Phys. Rev. Lett.* **79**, 2586 (1997).

[15] A. M. Steane, 'Dark matter in cosmology, quantum measurements and experimental gravitation', Proc. XXXI Recontres de Moriond (1996).

[16] I. L. Chuang, L. M. K. Vandersypen, X. Zhou, D. W. Leung and S. Lloyd, *Nature* **393**, 143 (1998).

[17] J. A. Jones, M. Mosca and R. H. Hansen, *Nature* **393**, 344 (1998).

[18] L. M. K. Vandersypen, M. Steffen, G. Breyta, C. S. Yannoni, M. H. Sherwood and I. L. Chuang, *Nature* **414**, 883 (2001).

[19] J. I. Cirac and P. Zoller, *Phys. Rev. Lett.* **74**, 4091 (1995).

[20] C. Monroe, D. M. Meekhof, B. E. King, W. M. Itano and D. J. Wineland, *Phys. Rev. Lett.* **75**, 4714 (1995).

[21] S. Gulde, M. Riebe, G. P. T. Lancaster, C. Becher, J. Eschner, H. Häffner, F. Schmidt-Kaler, I. L. Chuang and R. Blatt, *Nature* **421**, 48 (2003).

[22] S.-S. Li, G.-L. Long, F.-S. Bai, S.-L. Feng and H.-Z. Zheng, *Proc. Nat. Acad. Sci. U.S.A.* **98**, 11847 (2001).

[23] E. Biolatti, I. D'Amico, P. Zanardi and F. Rossi, *Phys. Rev. B* **65**, 075306 (2002).

[24] D. Loss and D. P. DiVincenzo, *Phys. Rev. A* **57**, 120 (1998).

[25] P. Zanardi and F. Rossi, *Phys. Rev. Lett.* **81**, 4752 (1998).

[26] M. S. Sherwin, A. Imamoglu and T. Montroy, *Phys. Rev. A* **60**, 3508 (1999).

[27] T. Tanamoto, *Phys. Rev. A* **61**, 022305 (2000).

[28] E. Biolatti, R. C. Iotti, P. Zanardi and F. Rossi, *Phys. Rev. Lett.* **85**, 5647 (2000).

[29] X. Li, Y. Wu, D. Steel, D. Gammon, T. H. Stievater, D. S. Katzer, D. Park, C. Piermarocchi and L. J. Sham, *Science* **301**, 809 (2003).

[30] G. Milburn, *Phys. World* **October 2003**, 24.

[31] S. C. Benjamin, *Phys. Rev. A* **61**, 020301 (2000).

[32] S. De Rinaldis, I. D'Amico, E. Biolatti, R. Rinaldi, R. Cingolani and F. Rossi, *Phys. Rev. B* **65**, 081309 (2002).

[33] I. D'Amico, E. Biolatti, F. Rossi, S. De Rinaldis, R. Rinaldis and R. Cingolani, *Superlatt. and Microstruct.* **31**, 117 (2002).

[34] I. D'Amico, S. De Rinaldis, E. Biolatti, E. Pazy, R. C. Iotti, P. Zanardi and F. Rossi, *Phys. Stat. Sol.* **234**, 58 (2002).

Chapter 5

Self-assembled InGaN quantum dots

5.1 Preliminary measurements

As a first step in the characterization of Samples A and B, initial macroscopic time-integrated measurements of the PL were made by Dr James Rice of the University of Oxford. The macroscopic PL spectrum of Sample A at 4.2 K was found to show two very broad, overlapping peaks centred at ∼2.97 eV and ∼2.83 eV. The higher energy peak corresponded to PL from the WL and the lower energy peak was attributed to PL from the QDs. In a similar way, the macroscopic PL spectrum of Sample B at 4.2 K was also found to show two very broad, overlapping peaks. These were centred at ∼2.85 eV and ∼2.53 eV. In this case, the higher energy peak was attributed to PL from QDs, whereas the lower energy peak was attributed to PL from the WL.

Following the macroscopic measurements, time-integrated μ-PL measurements were made (also by Dr James Rice) using the *Renishaw* μ-PL system (CW excitation at 325.0 nm being provided by the He-Cd laser). When light was collected from an unmasked part of Sample A or Sample B, the μ-PL spectrum was found to show only broad spectral features

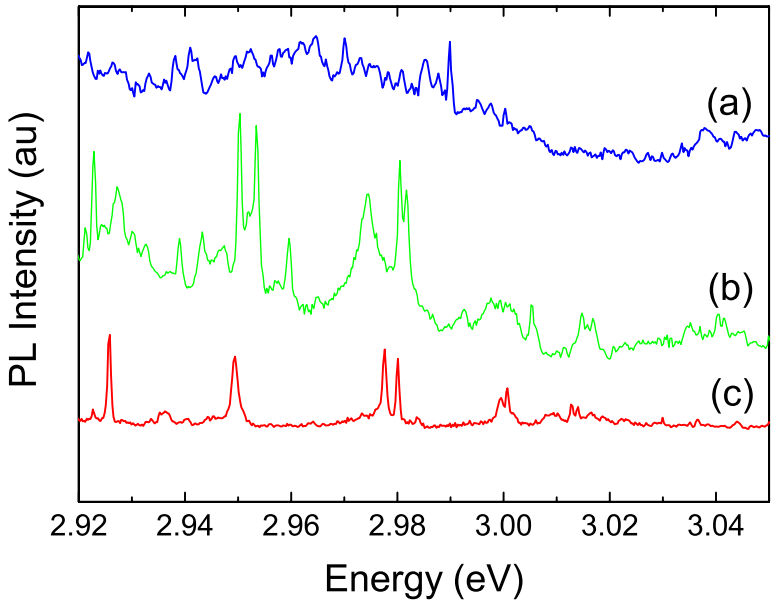


Figure 5.1: Three μ-PL spectra from Sample B, recorded at 4.2 K. (a) shows μ-PL from an unmasked area (laser spot size $\sim$2 μm), while (b) and (c) show μ-PL from square apertures with side lengths of 500 nm and 200 nm respectively. Sharp emission lines resulting from exciton recombination in single QDs are visible in (b) and (c), but not in (a) due to the large number of QDs being excited. Data from (1).

(Figure 5.1(a)) and was devoid of the individual sharp lines which characterize the μ-PL from single QDs. This is because so many QDs were excited simultaneously that it was not possible to make out the contributions from single QDs. However, if light was collected from a small aperture on the masked part of the sample instead (Figure 5.1(b)), thus restricting the number of QDs being studied, sharp lines corresponding to individual QDs *were* seen, superimposed upon the WL background. Reducing the size of the aperture area from which light was collected was found to reduce the number of sharp lines observed in the μ-PL spectrum (Figure 5.1(c)).

5.2 Time-resolved measurements

The presence of sharp spectral lines (resulting from exciton recombination in single QDs) in time-integrated μ-PL spectra from both Samples A and B having been established, the author performed time-resolved measurements in order to study the dynamics of exciton recombination in the two samples. This made it possible to find values for the exciton recombination lifetime T_1, which is significant for QIP applications.

The measurements were carried out using the high-resolution μ-PL set-up constructed by the author. Excitation was achieved using a Ti:Sapphire laser frequency-tripled to 266 nm. Two *Spex* 'Minimate' spectrometers were used to disperse the PL. One of the spectrometers was fitted with the CCD detector for time-integrated measurements (allowing the spectral positions of QD emission lines of interest to be determined), and the other was equipped with the time-correlated single photon counting system for time-resolved measurements. A movable mirror was used to direct the μ-PL to each spectrometer in turn.

The experimental arrangement is described in more detail in Chapter 3, with photographs in Figure 3.9.

5.2.1 Sample A

Figure 5.2 shows a time-integrated μ-PL spectrum collected at 4.2 K from an aperture in a masked area of Sample A. The spectrum displays a sharp peak at 2.862 eV, originating from exciton recombination in a single QD. The peak is superimposed upon a strong background signal originating from the underlying WL.

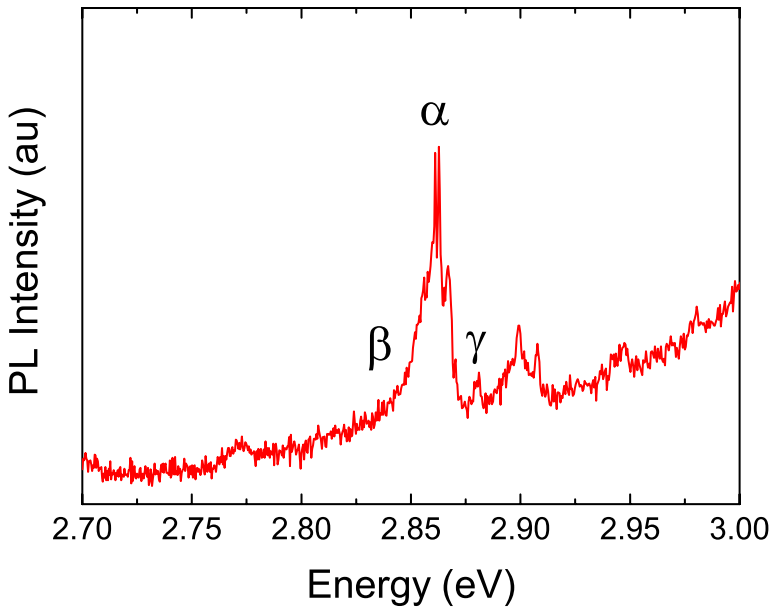


Figure 5.2: A time-integrated μ-PL spectrum from a single QD in Sample A, showing a sharp peak at 2.862 eV originating from exciton recombination. The background originates from WL emission.

Figure 5.3(a) shows three time-resolved traces marked α, β and γ, all recorded from Sample A at 4.2 K. Trace α was recorded at an energy of 2.862 eV, corresponding to the position of the dominant peak in Figure 5.2. Traces β and γ were recorded at 2.848 eV and 2.874 eV respectively, slightly lower and slightly higher in energy than the position of the peak.

The integrated areas under the time-resolved decay traces α, β and γ shown in Figure 5.3(a) would be expected to display the same relative magnitudes as the intensities observed in the time-integrated spectrum at positions α, β and γ shown in Figure 5.2. (The excitation power density was the same in both cases.) Calculations from 0 ns to 6 ns show that the integrated areas (arbitrary units) under the time-resolved decay traces α, β and γ were 5266, 2283 and 1972 respectively. This gives intensity ratios $I_{\alpha}^{\mathrm{TR}}/I_{\beta}^{\mathrm{TR}} = 2.31$ and $I_{\alpha}^{\mathrm{TR}}/I_{\gamma}^{\mathrm{TR}} = 2.67$. From the data shown in Figure 5.2, it was found that the intensities at positions α, β and γ were 432, 165 and 120 respectively (arbitrary units). This gives intensity ratios $I_{\alpha}^{\mathrm{TI}}/I_{\beta}^{\mathrm{TI}} = 2.62$

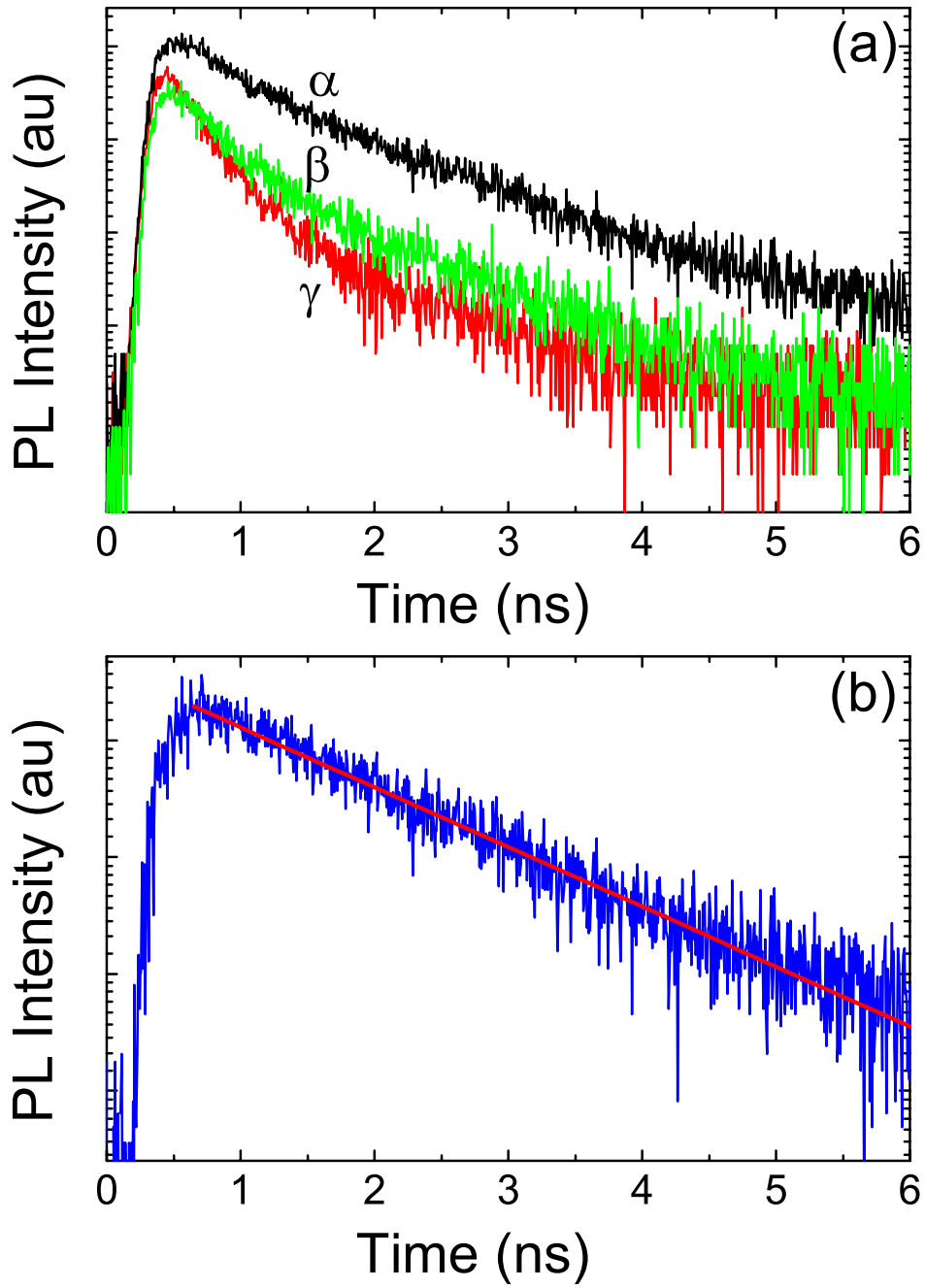


Figure 5.3: (a) Time-resolved μ-PL traces recorded from Sample A at 4.2 K, shown on a logarithmic scale. Trace α shows μ-PL corresponding to the peak at 2.862 eV in Figure 5.2. Traces β and γ correspond respectively to WL positions at slightly lower energy (2.848 eV) and slightly higher energy (2.874 eV). In each case, the excitation power density was the same as that used in recording the data shown in Figure 5.2. (b) The trace which results when the average of traces β and γ is subtracted from α, again shown on a logarithmic scale. The red line is a linear fit, demonstrating that the subtracted decay is almost perfectly mono-exponential. The lifetime is 1.79 ns.

and $I_\alpha^{\mathrm{TI}}/I_\gamma^{\mathrm{TI}} = 3.60$. Thus the time-resolved and time-integrated measurements give approximately the same ratios of I_α/I_β and I_α/I_γ, just as would be expected. The ratios in the time-resolved case were slightly lower than in the time-integrated case, but this was probably because of the limited resolution of the spectrometer. Recording a signal at position α would actually involve integrating light from a finite range of wavelengths surrounding α. Since the peak was at α, the mean intensity over the wavelength range surrounding α would be less than at α itself, making the peak appear less intense in time-resolved measurements.

It can be seen from Figure 5.2 that the QD-related μ-PL peak at 2.862 eV is sharp, and so the time-resolved traces β and γ recorded at 2.848 eV and 2.874 eV will consist of emission solely from the WL. However, since in the sample the QD is known to lie spatially on top of the WL, the time-resolved trace α must consist of emission from *both* the QD *and* the WL. Therefore, in order to isolate the emission from the QD, it is necessary to perform a *subtraction* of the WL signal. Because the WL signal changes only slowly with energy compared to the sharp QD peak, the time-resolved WL contribution at the position of the peak can be taken to be approximately the average of the two WL traces on each side. Thus the necessary subtraction can be performed by subtracting the average of β and γ from α. Figure 5.3(b) shows the time-resolved trace which results from this subtraction process.

The red line in Figure 5.3(b) is a linear fit to the subtracted decay trace. As can be seen, the subtracted trace is almost perfectly mono-exponential. This is in sharp contrast to the WL traces β and γ and to the unsubtracted decay trace α, which consists of a combination of QD and WL emission.

Ensemble measurements on other nitride QD systems (2; 3) have been made, and strongly non-exponential decays have been reported. Given the data shown in Figure 5.3, it appears

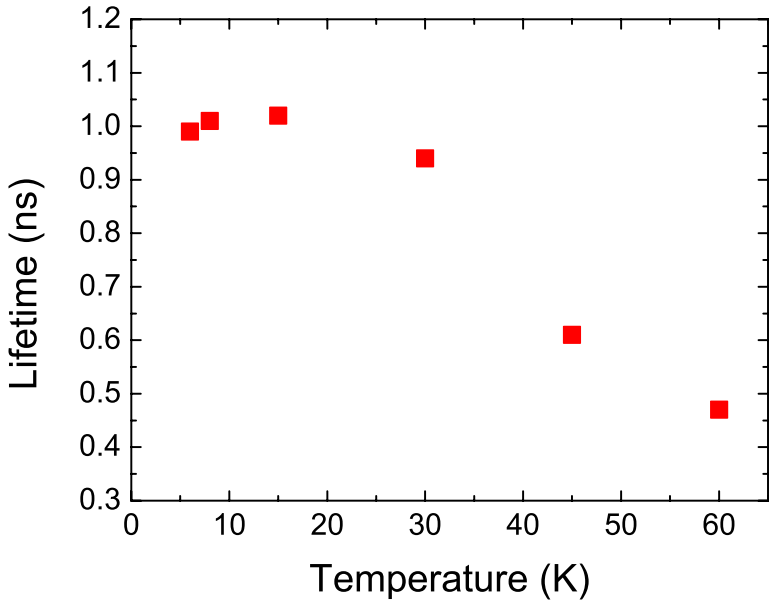


Figure 5.4: A plot of the exciton recombination lifetime in a single QD in Sample A (emitting at 2.862 eV) as a function of temperature. These data points were determined from time-resolved measurements as described in the text.

likely that a combination of QD and WL emission is responsible for this.

Further μ-PL spectra were recorded at a range of excitation power densities. As the excitation power density was reduced, the ratio of the QD signal to the WL signal increased, but the behaviour shown in Figure 5.3 was maintained: an almost perfectly mono-exponential single-QD decay trace following background subtraction.

Finally, the dependence of the lifetime upon temperature was investigated. The QD and WL decay traces from the single QD shown in Figure 5.2 were recorded at a range of temperatures in the range 6 K to 60 K, and the exciton recombination lifetime was determined using the background subtraction procedure already described. The lifetime varied from 0.99 ns at 6 K to 0.47 ns at 60 K, as shown in Figure 5.4. Above 60 K, the QD signal 'washed out' and it was no longer possible to measure the lifetime.

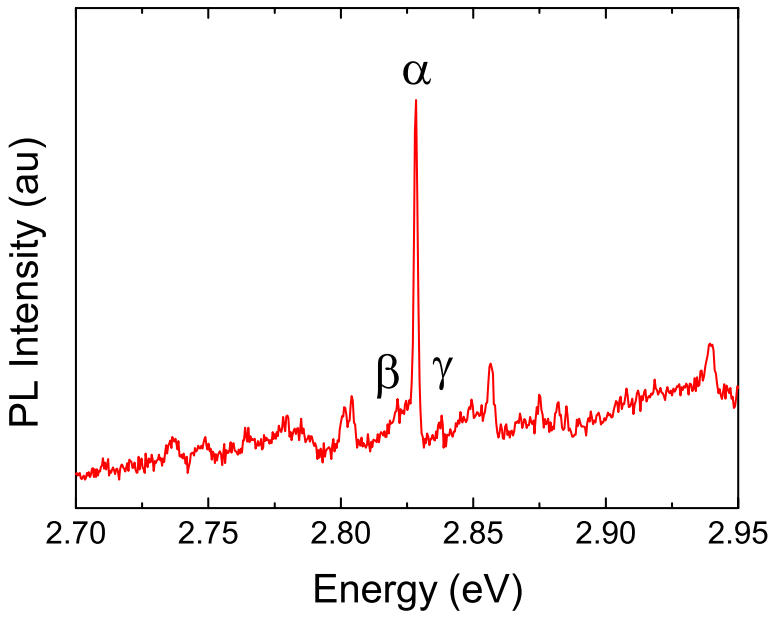


Figure 5.5: A time-integrated μ-PL spectrum from a single QD in Sample B, showing a sharp peak at 2.830 eV originating from exciton recombination. The background originates from WL emission.

5.2.2 Sample B

The experimental investigations performed on Sample A were repeated on Sample B. Figure 5.5 shows a time-integrated μ-PL spectrum collected at 4.2 K from an aperture in a masked area of Sample B. The spectrum displays a sharp peak at 2.830 eV, originating from exciton recombination in a single QD. The peak is again superimposed upon a strong background signal originating from the underlying WL.

Just as for Sample A, decay traces β (at 2.825 eV) and γ (at 2.837 eV) were recorded from the WL at slightly lower and slightly higher energies than that of the exciton recombination peak α (at 2.830 eV). These three time-resolved traces are shown on a logarithmic scale in Figure 5.6(a). The contribution of the WL signal to the decay trace α was subtracted out as before, giving the trace shown in Figure 5.6(b). This trace, consisting solely of emission from

the QD, is seen to be almost perfectly mono-exponential, just as for Sample A. Again, this is in sharp contrast to the non-exponential decays from the WL and from the unsubtracted QD. Just as for Sample A, the ratio of the QD signal to the WL signal was found to increase as the excitation power density was reduced, but the mono-exponential behaviour following subtraction was maintained.

Following initial time-resolved studies of Sample B, the temperature dependence of the exciton recombination lifetime of the QD shown in Figure 5.5 was investigated. Figure 5.7(a) shows time-integrated μ-PL spectra recorded from Sample B at a range of temperatures between 4.2 K and 60 K. The PL peak resulting from exciton recombination is seen to decline in intensity with increasing temperature, and is completely 'washed out' by $\sim$60 K. It is likely that this behaviour is caused by carriers being lost to thermally-activated non-radiative centres, or to their being emitted thermally from the QDs. Figure 5.7(b) shows a plot of the exciton recombination lifetime as a function of temperature for the single QD shown in Figure 5.5, as determined from time-resolved measurements. Just as for Sample A (Figure 5.4), the lifetime is seen to decrease as the temperature rises.

After the studies of the QD whose time-integrated μ-PL spectrum is shown in Figure 5.5, further investigations were made of several *other* QDs in Sample B. Figure 5.8 shows a time-integrated μ-PL spectrum which clearly exhibits a number of different exciton recombination lines at various energies. The lifetime of exciton recombination was determined experimentally in a number of cases by monitoring emission at the QD peak and at WL positions on each side, as described previously. The results of these time-resolved measurements are shown in Figure 5.8, where experimentally-deduced lifetimes are shown above a number of the peaks. It is interesting to note that although there is a range of lifetimes, they all lie

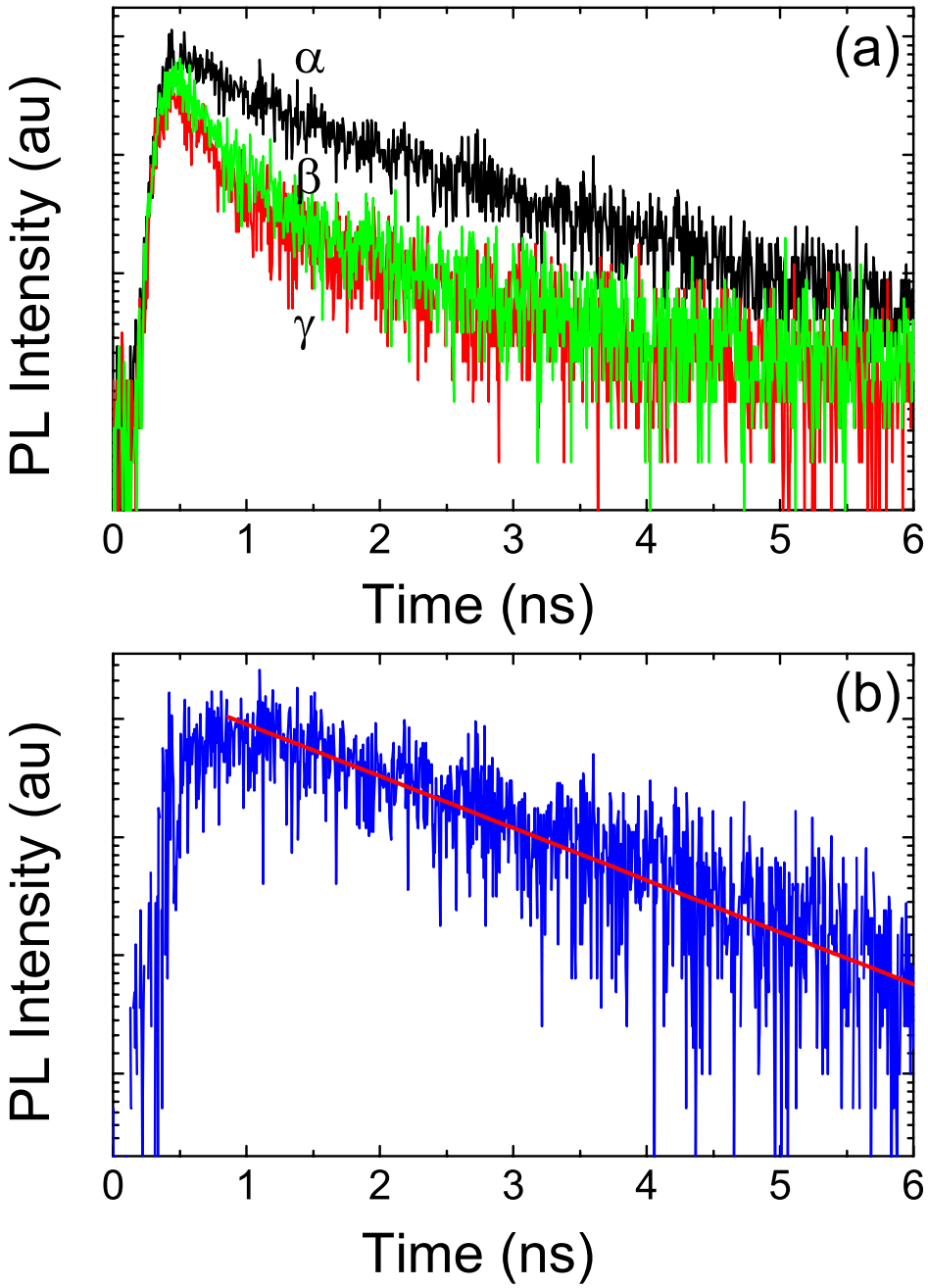


Figure 5.6: (a) Time-resolved μ-PL traces recorded from Sample B at 4.2 K, shown on a logarithmic scale. Trace α shows μ-PL corresponding to the peak at 2.830 eV in Figure 5.5. Traces β and γ correspond respectively to WL positions at slightly lower energy (2.825 eV) and slightly higher energy (2.837 eV). (b) The trace which results when the average of traces β and γ is subtracted from α, again shown on a logarithmic scale. The red line is a linear fit, demonstrating that the subtracted decay is almost perfectly mono-exponential. The lifetime is 2.43 ns.

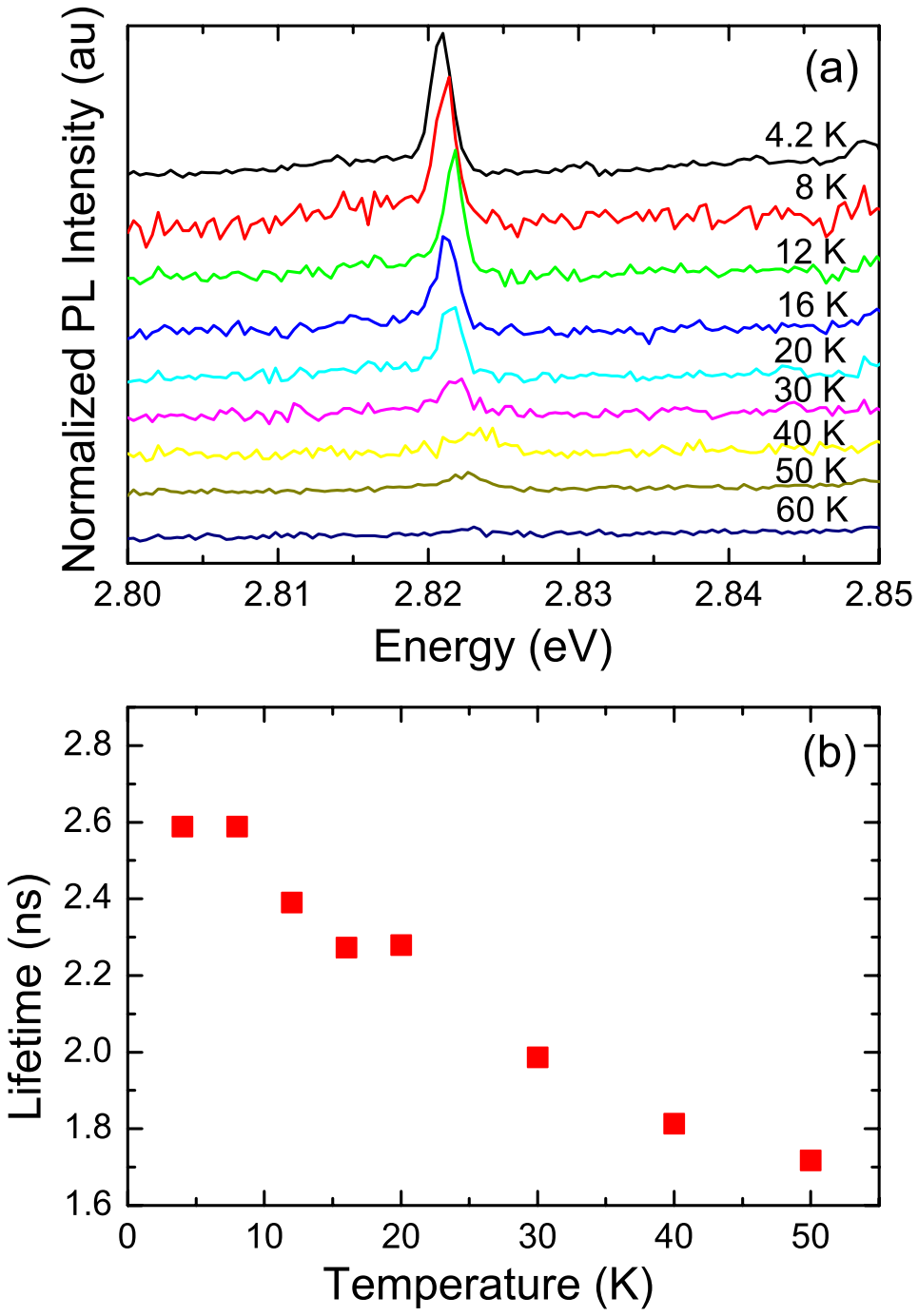


Figure 5.7: (a) A series of time-integrated μ-PL spectra from the single QD shown in Figures 5.5 and 5.6, recorded at temperatures between 4.2 K and 60 K. The exciton recombination peak decreases in intensity and broadens as the temperature rises, and has completely 'washed out' by 60 K. (b) A plot of the exciton recombination lifetime (determined from time-resolved measurements as described in the text) as a function of temperature, corresponding to the time-integrated spectra shown in (a).

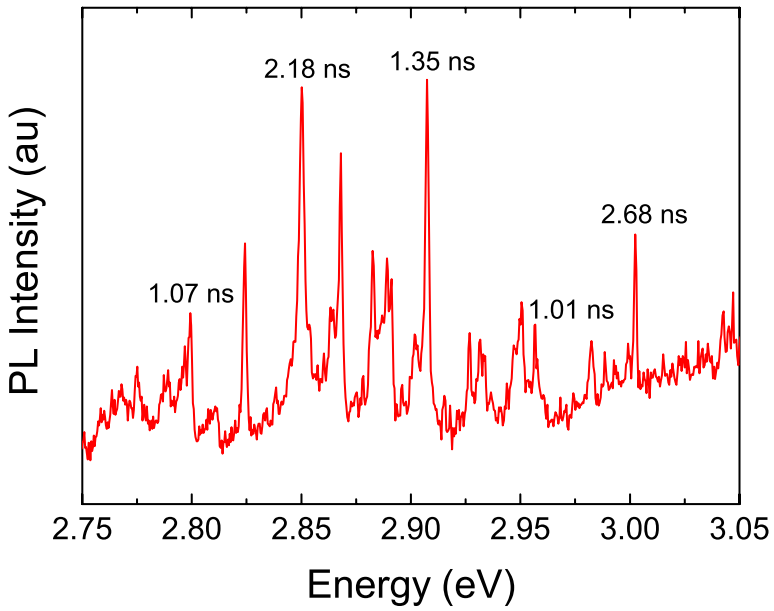


Figure 5.8: A time-integrated μ-PL spectrum from Sample B, recorded at 4.2 K, showing exciton recombination lines from many different QDs. Time-resolved measurements were performed on a number of the lines, and the experimentally-deduced lifetimes are shown above the relevant peaks.

within a relatively narrow range of ∼1–2 ns. In earlier work on QD ensembles the lifetime was found to decrease sharply with increasing energy (2). No evidence of this is found in Sample B.

5.3 Linewidth measurements

The linewidth of an exciton recombination peak originating from a single QD can provide important information about the interaction of excitons in the QD with their environment. In the absence of inhomogeneous broadening, the linewidth of an exciton recombination line will be limited by homogeneous broadening processes associated with decoherence. If the exciton decoherence time is T_2, in a two-level model (4; 5; 6) the FWHM Γ is given by the

expression

$$\Gamma = 2\hbar/T_2. \tag{5.1}$$

Since T_2 is an important parameter in potential implementations of QIP, efforts were made to determine the narrowest linewidths observable in Samples A and B. As before, the high-resolution μ-PL set-up was used, but this time with CW excitation provided by a He-Cd laser operating at 325.0 nm. The 0.85 m double-grating spectrometer was used in order to obtain high spectral resolution, thus permitting measurement of very narrow linewidths. In practice, the spectrometer was used in single-grating mode rather than in double-grating mode, since this was sufficient to resolve the narrowest spectral lines which were observed.

Figure 5.9 displays a time-integrated μ-PL spectrum showing the narrowest exciton recombination line observed in the PL from Sample A. The FWHM here is $\sim$290 μeV. Using Equation 5.1, this implies a decoherence time of $T_2 \geq 4.5$ ps.

Figure 5.10 displays a time-integrated μ-PL spectrum showing the narrowest exciton recombination line observed in the PL from Sample B. The FWHM here is $\sim$230 μeV. Using Equation 5.1, this implies a decoherence time of $T_2 \geq 5.7$ ps.

In practice, the values calculated above for T_2 for excitons confined in QDs in Samples A and B are simply lower limits. In using Equation 5.1, it has been assumed that linewidth broadening is purely related to decoherence. In reality, this is unlikely to be the case, and there are a number of other processes which can also cause linewidth broadening. This means that the actual values of T_2 for excitons confined in QDs in Samples A and B may be considerably larger than those calculated above.

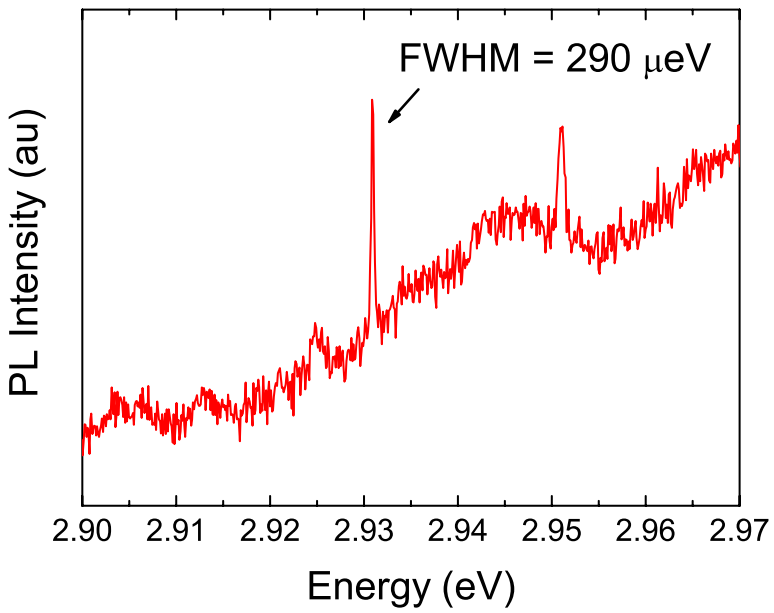


Figure 5.9: A time-integrated μ-PL spectrum showing the narrowest exciton recombination line observed in Sample A, the FWHM being $\sim$290 μeV. The spectrum was recorded at 4.2 K.

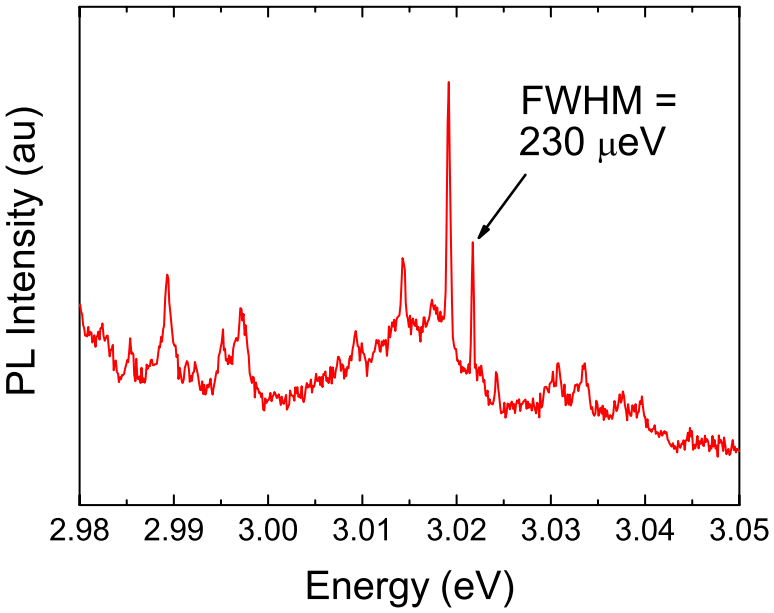


Figure 5.10: A time-integrated μ-PL spectrum showing the narrowest exciton recombination line observed in Sample B, the FWHM being $\sim$230 μeV. The spectrum was recorded at 4.2 K.

5.4 Spectral diffusion measurements

5.4.1 Introduction

The energy levels in a quasi zero-dimensional system (such as a QD) may be strongly influenced by the local semiconductor environment. For example, a fluctuating local charge distribution (perhaps caused by the trapping and untrapping of carriers in nearby defects) will generate a time-varying local electric field which may transiently perturb QD energy levels via the quantum-confined Stark effect (QCSE). This can result in a jitter (so-called *spectral diffusion*) of the spectral features (such as the transition energy) of an exciton recombination peak on a long timescale (typically seconds) (7).

Spectral diffusion has been observed experimentally in ions (8; 9), in single molecules (10; 11; 12) and in nanocrystals (13; 14; 15; 16). Studies of linewidth broadening in the emission spectra of epitaxially-grown QDs had indirectly implied the presence of spectral diffusion in these systems (17), but it was not until 2000 that the phenomenon was directly observed (7; 18; 19). In (7) and (18), spectral shifts of up to 3.5 meV and 1 meV respectively were seen in the emission spectra of self-assembled CdSe QDs. In both cases, the spectral diffusion was attributed to Stark shifts caused by fluctuating local electric fields due to trapping and untrapping of photo-excited carriers. In (19), spectral shifts of up to 1.1 meV were seen in the emission spectra of self-assembled InAlAs QDs, and were again attributed to Stark shifts caused by local trapping and untrapping of carriers.

In 2004, cathodoluminescence measurements were used to demonstrate spectral diffusion in single InGaN QDs formed by interface fluctuations in an InGaN quantum well (20). However,

prior to the work described in this Chapter, there are no previous reports in the literature of spectral diffusion in single self-assembled InGaN QDs.

5.4.2 Data acquisition

In order to determine whether single self-assembled InGaN QDs exhibited spectral diffusion behaviour, sequences of time-integrated μ-PL spectra from single InGaN QDs in Sample B were recorded using the high-resolution μ-PL set-up. Excitation was provided by a CW He-Cd laser operating at 325.0 nm. The PL was dispersed using the double-grating spectrometer in order to obtain high spectral resolution, so that even small spectral shifts could be resolved.

The μ-PL system first had to be manually aligned so that the exciton recombination peak from a single QD was clearly seen in the CCD time-integrated spectrum. Spectra were recorded at a number of excitation power densities in order to check that the peak definitely did originate from exciton recombination and not from a higher-order process. At an appropriate excitation power density, the software controlling the CCD was then programmed to sequentially record a large number of spectra with individual integration times of either 3 s or 10 s, and to save the spectra to disc. These time-integrated spectra could then be compared, allowing any changes in the energy, intensity or FWHM of the exciton recombination peak to be measured.

5.4.3 Computerized data analysis

Typically, an experimental run would result in the accumulation of several hundred individual time-integrated spectra. It would have been impractical to fit each spectrum by hand in order to track the evolution of the energy, intensity and FWHM of the exciton recombination peak. Therefore, the author wrote the computer programme DIFFUSION (running in *Mathworks* MATLAB) to automatically extract this information and write it to file. The code is shown in Appendix A.

The programme DIFFUSION began by reading from file the data corresponding to an entire experimental run. This data related to a large number of sequentially-recorded μ-PL spectra. Typically, a single spectrum would consist of a single exciton recombination peak superimposed upon a broad WL background. For each spectrum, the tasks of the programme were to (i) determine the spectral position of the recombination peak, (ii) find its intensity, and (iii) calculate the FWHM. After (i)–(iii) had been carried out, the programme stored the values of peak position, intensity and FWHM in a matrix and then analyzed the next spectrum. When all the individual spectra from an entire experimental run had been fitted in this way, DIFFUSION wrote to an output file the matrix containing all the values of peak position, intensity and FWHM.

The method of operation of DIFFUSION will now be outlined. The discussion can be followed by referring to the code of the programme given in Appendix A. It should be noted that DIFFUSION operated entirely in terms of pixel number (since data from the CCD was automatically saved to file in terms of CCD pixel numbers), and that calibration to wavelength or energy had to be carried out manually by the user afterwards.

The programme began by prompting the user for an estimated position (in pixels) for the recombination peak to be fitted. The estimated position had to be determined manually by the user: the first time-integrated spectrum from the experimental run under study generally had to be fitted by hand using *Microcal* ORIGIN.

After the estimated peak position had been entered, DIFFUSION began to analyze the first experimental spectrum. It was possible that the original data contained some 'cosmic ray' events: these would be very sharp, high-intensity peaks in the μ-PL spectrum caused by high-energy particles from outside the Earth's atmosphere striking the detector. It was very important to remove these events from the spectrum since the sharp peaks would be difficult to distinguish from the recombination peak at the fitting stage. Therefore, DIFFUSION contained a routine to remove any such cosmic ray events. This routine checked each element in the matrix containing the data read from file, and set to zero any data point which was greater than a certain pre-determined value, 'cosmic'. The value of 'cosmic' could be set by the user to be greater than any point on the actual experimental spectrum, so that any data point exceeding 'cosmic' had to be associated with a cosmic ray event and could be safely removed.

Following removal of cosmic ray events, DIFFUSION then *smoothed* the data using *5-point averaging*: each data point was re-calculated by averaging it with the two data points on each side. The purpose of this smoothing was to reduce the effect of random fluctuations in the spectrum (noise) in order to bring out more clearly the underlying shape of the curve.

Using the smoothed data, DIFFUSION found the position of the peak. For the first spectrum, this was done using the estimated position entered by the user. For subsequent spectra, the position of the peak in the previous spectrum was taken as the 'best guess' for its position

in the next (this assumed a relatively low rate of spectral diffusion, which turned out to be a valid assumption). The programme examined the points 15 pixels each side of the estimated peak position in order to determine which point had the highest value (corresponding to the most intense emission): this was then assumed to be the peak. The intensity was then also easily obtained, since this was simply the value at that point.

The FWHM was more difficult to calculate. In order to find a value for this, it was first necessary to calculate a 'baseline' corresponding to the WL emission underneath the peak. The true peak height would then be the measured peak intensity minus this baseline. A value for the baseline was calculated by averaging the signal across a spectral window around the vicinity of the peak. Once the true peak height had been found, the half width (on one side of the peak) could be calculated by stepping across the peak, looking for the pixel position at which the squared difference between the value at that point and half the peak height was minimized. This process was repeated on the other side of the peak to give the other half width, and the two half widths were then added to give the FWHM.

Once DIFFUSION had calculated peak position, intensity and FWHM for a single spectrum, it stored these values at appropriate locations in a matrix and then examined the next spectrum. This continued until all the spectra in a given experimental run had been analyzed. The programme then wrote an output file containing the results of this process.

5.4.4 Measurements and discussion

Figure 5.11 shows μ-PL spectra recorded at 4.2 K with an excitation power density of 7×10^3 Wcm^{-2}. This excitation power density was sufficiently low to ensure that only single-

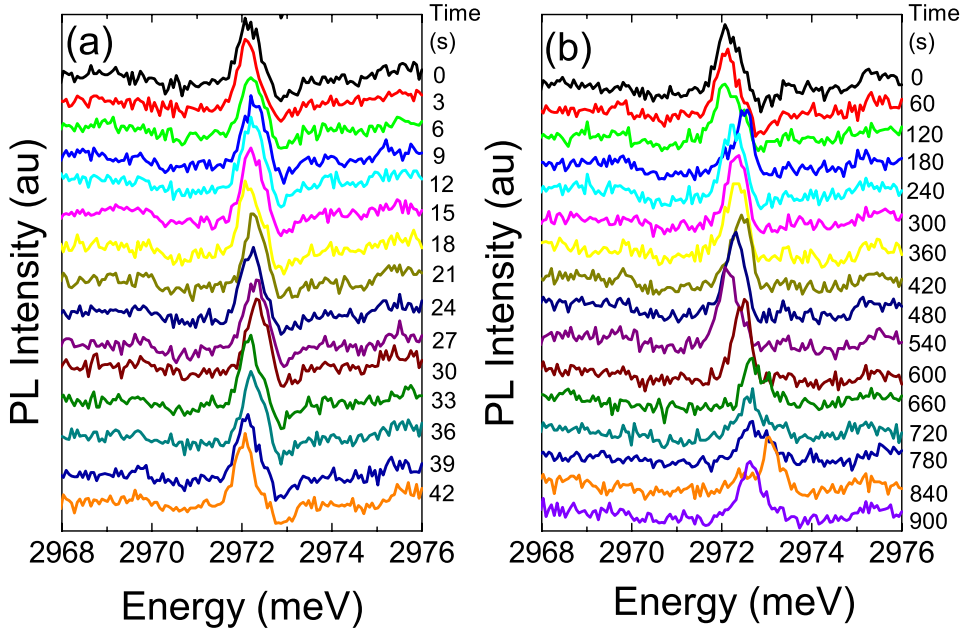


Figure 5.11: μ-PL spectra from a single QD, recorded at 4.2 K. The integration time for each spectrum was 3 s. (a) A series of consecutively-recorded spectra at 3 s intervals. (b) A series of consecutively-recorded spectra at 60 s intervals.

exciton states (consisting of a single electron-hole pair) were excited. Figure 5.11(a) shows the time evolution over a 42 s period of an isolated recombination peak corresponding to a single-exciton optical transition. Figure 5.11(b) shows the time evolution over a much longer period of 900 s for the same peak. In Figure 5.11(a), changes in the peak position of up to 0.3 meV are seen along with variations in the FWHM of up to 150 μeV. Over the much longer observation time shown in Figure 5.11(b), larger fluctuations in the peak position of up to 1 meV are seen and the FWHM shows greater variations of up to 350 μeV.

As discussed in Section 5.4.1, studies of temporal variations in recombination peak energy and intensity have been previously performed for epitaxially-grown CdSe QDs (7). The shifts which were observed were interpreted as arising from carriers becoming trapped in defect states in the vicinity of the QDs. A trapped carrier would generate a local electric

field. Thus the electric field at a particular QD would change with time as different numbers of carriers became trapped nearby and subsequently escaped, resulting in a transient Stark shift of the QD emission (14; 21). It is believed that the same mechanism is responsible for the spectral diffusion which is observed in the InGaN QD system.

In general, a carrier will remain trapped in a defect for time $\tau_{\text{trap}} = \tau_{\text{phonon}}\exp(E_{\text{trap}}/kT)$. Here, τ_{phonon} is a typical phonon scattering time and E_{trap} is the trap potential depth. This implies that at low temperatures τ_{trap} may range from seconds to minutes (7), even for trap depths of only a few meV. The magnitude of the spectral diffusion shifts observed in the CdSe QDs implied variations in the local electric field of $\sim 10^5$ Vcm^{-1}. A field of this magnitude would be generated by a single carrier lying within a radius of $\sim$10 nm (7; 14). Carrier trapping in the CdSe QDs was believed to occur in dislocations caused by stacking faults (7).

AFM studies of uncapped InGaN QD samples show a large number of 'pits' in the sample surface whose formation is induced by the growth process. After capping with GaN, these pits are filled, providing interfaces which could act as trapping centres (22). Additionally, the presence of self-formed In-rich regions (23; 24) and the high threading dislocation density ($\sim 10^9$ cm^{-2} in Sample B) may provide centres for carrier trapping. It is also possible in principle that electric fields could be generated by carriers trapped in adjacent QDs. However, AFM data suggests that the distance between QDs is usually much greater than the $\sim$10 nm separation which would be necessary to generate the required field. Thus it would appear that spectral diffusion in the emission from single InGaN QDs is due to the trapping of carriers near pits, in In-rich regions and in dislocations.

Figure 5.12 shows data obtained from the same QD as in Figure 5.11, but over a longer period

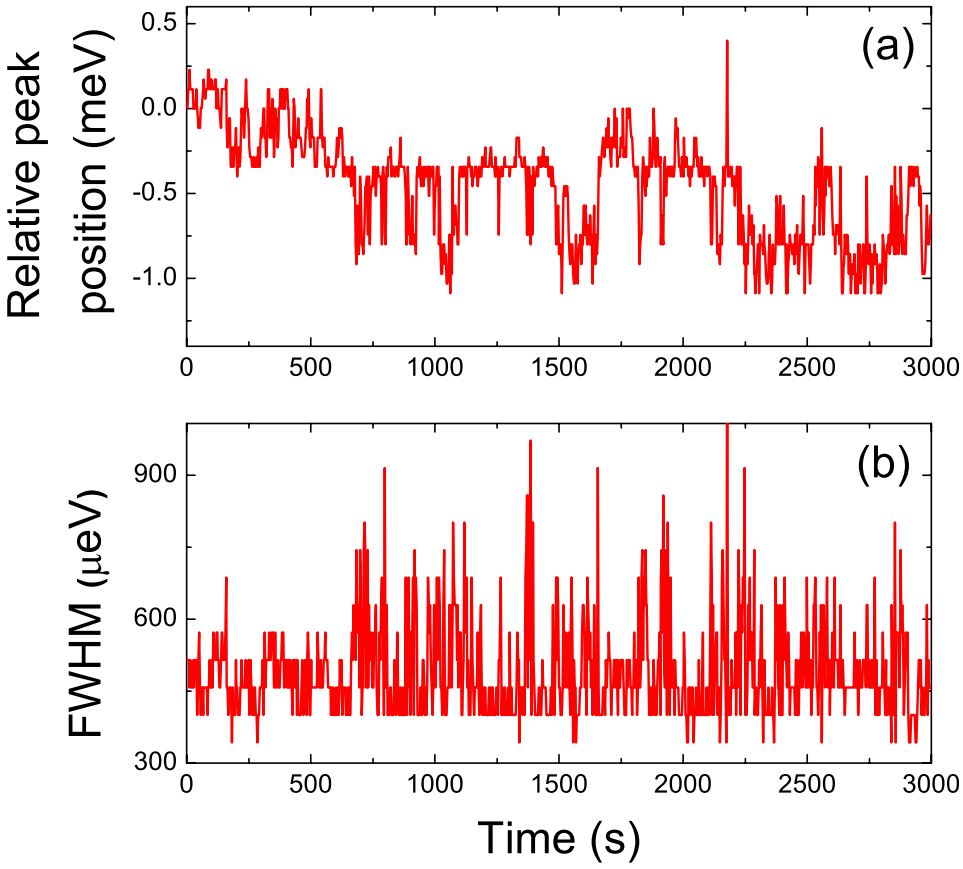


Figure 5.12: Plots of (a) relative peak position and (b) FWHM from μ-PL spectra from a single QD, recorded at 4.2 K. Each individual spectrum was accumulated for 3 s, and the measurements were recorded over 3000 s in total. This data was extracted from the raw experimental spectra using the computer programme DIFFUSION, written by the author.

of 3000 s. In order to construct this figure, individual μ-PL spectra of the type displayed in Figure 5.11 were analyzed using the programme DIFFUSION (as described in Section 5.4.3) in order to extract the required data. Figure 5.12(a) and Figure 5.12(b) respectively show the relative peak position and FWHM as a function of time. The peak position is found to display a maximum variation of 1.35 meV, while the FWHM varies by up to 600 μeV.

Calculations were made in order to determine whether the fluctuations seen in Figure 5.12 were completely random, or whether any periodicity was present. This was done using the

autocorrelation function $C(\Delta t)$ given by the expression

$$C(\Delta t) \equiv \frac{1}{N} \int A(t)A(t+\Delta t)\ dt, \tag{5.2}$$

where $A(t)$ is the quantity of interest at time t and where $1/N$ is a normalization factor. The autocorrelation function provides a way of determining the degree of correlation between a signal at time t and at later time $t + \Delta t$. The value of the integral in Equation 5.2 becomes large if there is a correlation.

The computer programme CORRELATE (running in MATLAB) was used to calculate a numerical value for the autocorrelation function, using the data shown in Figure 5.12. The code for this programme is shown in Appendix B. The method of operation of CORRELATE was simple. The raw data was smoothed using 21-point averaging, and a polynomial line of best fit (calculated using ORIGIN) was subtracted. (The subtraction of the line of best fit reduced problems caused by long-timescale systematic departures of the curve from the $y = 0$ line. The timescales involved were much longer than those expected to be associated with any periodic behaviour.) The value of the autocorrelation function for the smoothed, scaled data was then calculated over a range specified by the user.

Following analysis using CORRELATE, no evidence of periodic behaviour was found for either the peak position or the FWHM over the measured time frame: both quantities appeared to vary entirely randomly with time. Although this observation was is in contrast to the quasi-periodic behaviour reported for peak position in CdSe QDs (7), it is nevertheless consistent with the proposed spectral diffusion mechanism. Stark shifts caused by the electric fields from locally trapped carriers would be expected to vary randomly with time, since the process of carrier trapping would also be expected to be random.

Even though no evidence for periodic behaviour was found, it was also possible that there was a correlation between the energy position of the exciton recombination peak and its FWHM. It seemed possible that a local electric field might influence both. In order to evaluate the extent of any such correlation, the *Pearson product moment correlation coefficient*, r, for the two data sets shown in Figure 5.12(a) and Figure 5.12(b) was calculated. The value of r reflects the extent of linear relationship between two data sets, and is defined by the expression

$$r \equiv \frac{n\Sigma xy - \Sigma x \Sigma y}{\sqrt{[n\Sigma x^2 - (\Sigma x)^2][n\Sigma y^2 - (\Sigma y)^2]}} \tag{5.3}$$

for a general set of n data points (x_i, y_i) (25).

The value of r in this case was found to be 0.08, indicating very weak correlation. Thus there seemed to be no significant correlation between the peak position and its FWHM. Similar results were obtained from other experimental runs on different QDs.

Next, a more detailed investigation of the energies of the exciton recombination peak was made. It was possible that the recombination energy either varied completely randomly within the spectral diffusion range, or that it was more likely to take some values rather than others. Temporal variation of peak position is plotted in Figure 5.13 as statistical histograms for three different power densities. At the highest excitation power density (7×10^3 Wcm^{-2}), the histogram shows a clear maximum for the peak position at ΔS=0 meV (where ΔS is the relative peak shift), with the occurrence of peak position occupancy declining on both sides of the maximum. A secondary maximum is seen in the histogram at ΔS=-0.45 meV. An explanation for this may be given by referring to defect sites: a single closely-lying site may perhaps induce a Stark shift of magnitude 0.45 meV. The proximity of this site relative to the others would result in a shift of this magnitude being induced more frequently over time

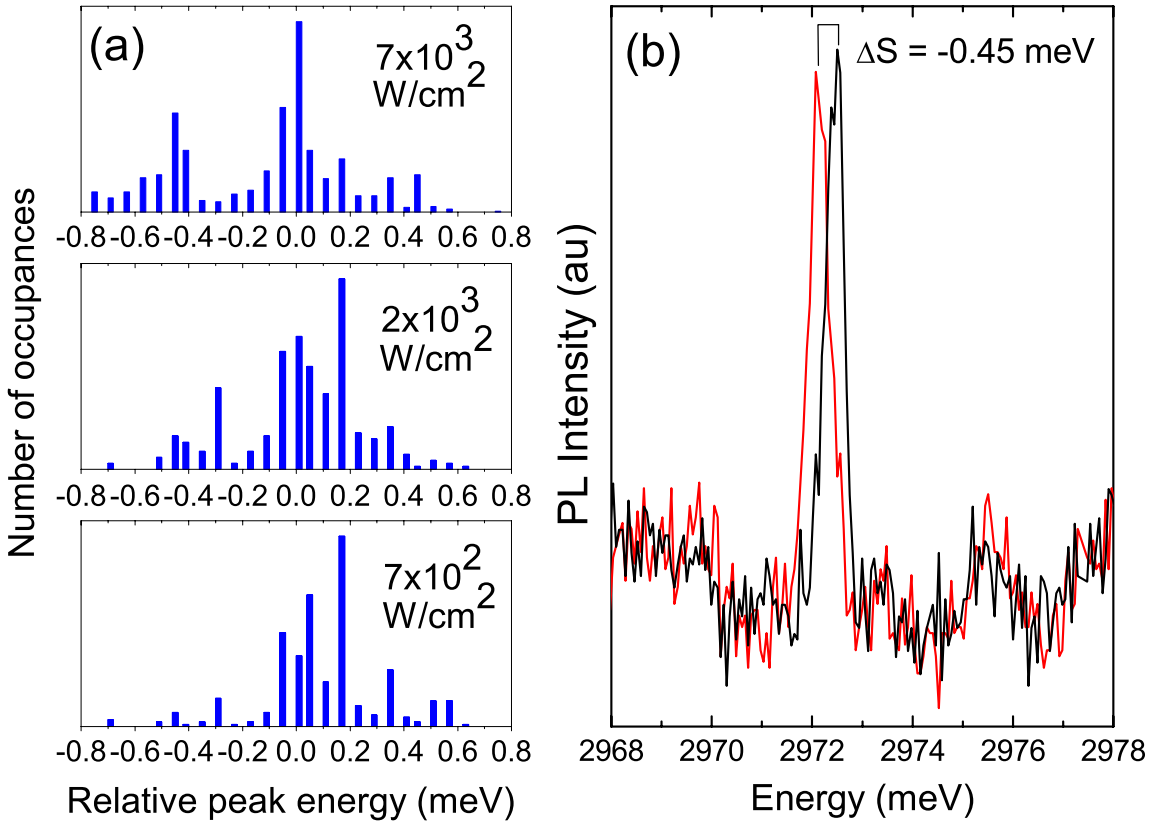


Figure 5.13: (a) Statistical histogram plots of occupancy rate for various recombination peak energy positions, at three different power densities. (b) A pair of μ-PL spectra recorded at different times from a single QD, clearly illustrating the ΔS=-0.45 meV displacement.

than other Stark shift magnitudes which originate from defect sites at greater distances. At an excitation power density of 2×10^3 Wcm^{-2}, a local maximum is still observed at ΔS=-0.45 meV with a reduced occupancy rate. Reducing the laser excitation power still further to 7×10^2 Wcm^{-2} results in the disappearance of the local maximum from the histogram.

A study was made of the effect of temperature upon the temporal variations in the recombination peak energy position. Sequences of μ-PL spectra from a single QD were recorded at several different temperatures in the range 4.2 K to 60 K. The individual spectra showed that as the temperature increased, the intensity from the single QD peak in the PL spec-

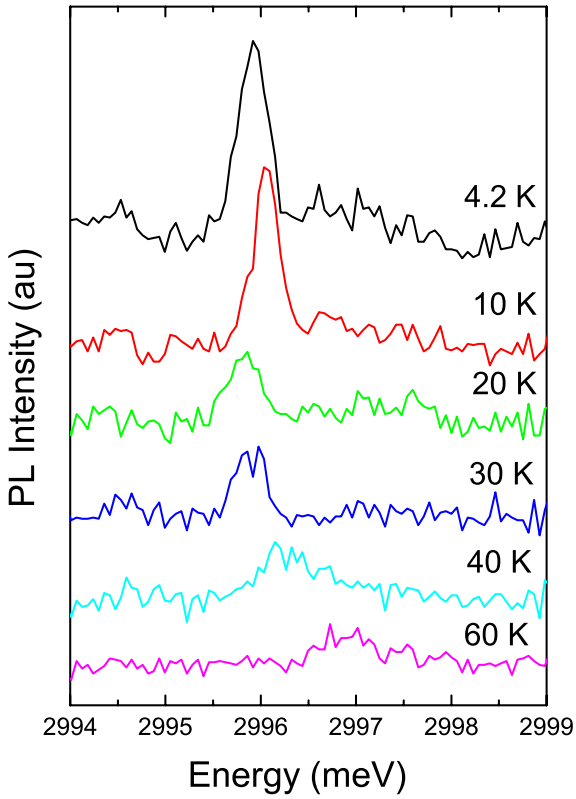


Figure 5.14: Time-integrated μ-PL spectra recorded from a single QD at a range of temperatures between 4.2 K and 60 K. The integration time was 10 s in each case. The intensity of the exciton recombination peak is clearly seen to decrease as the temperature rises.

trum decreased, as reported previously (22). Single time-integrated spectra are shown in Figure 5.14.

For each temperature, the programme DIFFUSION was used to extract from the series of individual spectra the energy position of the exciton recombination peak as a function of time. The result of this process is shown in Figure 5.15(a). As the temperature increased, the relative peak position apparently fluctuated with a greater amplitude. The standard deviation was calculated for each of the traces shown in Figure 5.15(a), and the results of this process are shown in Figure 5.15(b). There appeared to be a positive (and apparently approximately linear) correlation between temperature and the standard deviation of the

fluctuations. It might be possible to explain this behaviour in terms of thermally-activated traps which only become accessible at higher temperatures, perhaps due to the existence of higher-energy trapped states. The presence of additional active traps might lead to the trapping of more carriers, and hence to the generation of stronger electric fields giving larger shifts.

Unfortunately, however, it was difficult to be certain whether the apparent increase in the amplitude of the fluctuations with temperature was a real effect. As the temperature increased, the poorer QD-to-background intensity ratio made it harder to track the position of the recombination peak accurately. It is also possible that this may have accounted for the apparent increase in the amplitude of the fluctuations.

5.5 Summary and conclusion

Initial macroscopic time-integrated measurements on Samples A and B showed that masking was effective in reducing the number of QDs from which PL was observed. For small aperture sizes, sharp spectral lines corresponding to exciton recombination in single QDs were recorded.

Time-integrated μ-PL measurements were used to identify exciton recombination lines originating from single QDs in both Sample A and Sample B. Time-resolved measurements of these exciton recombination lines and of WL emission at slightly lower and slightly higher energy all showed non-exponential decays, but *subtraction* of the WL signal from the QD trace revealed almost perfectly mono-exponential decays. This behaviour was maintained over a range of excitation power densities and temperatures. The exciton recombination

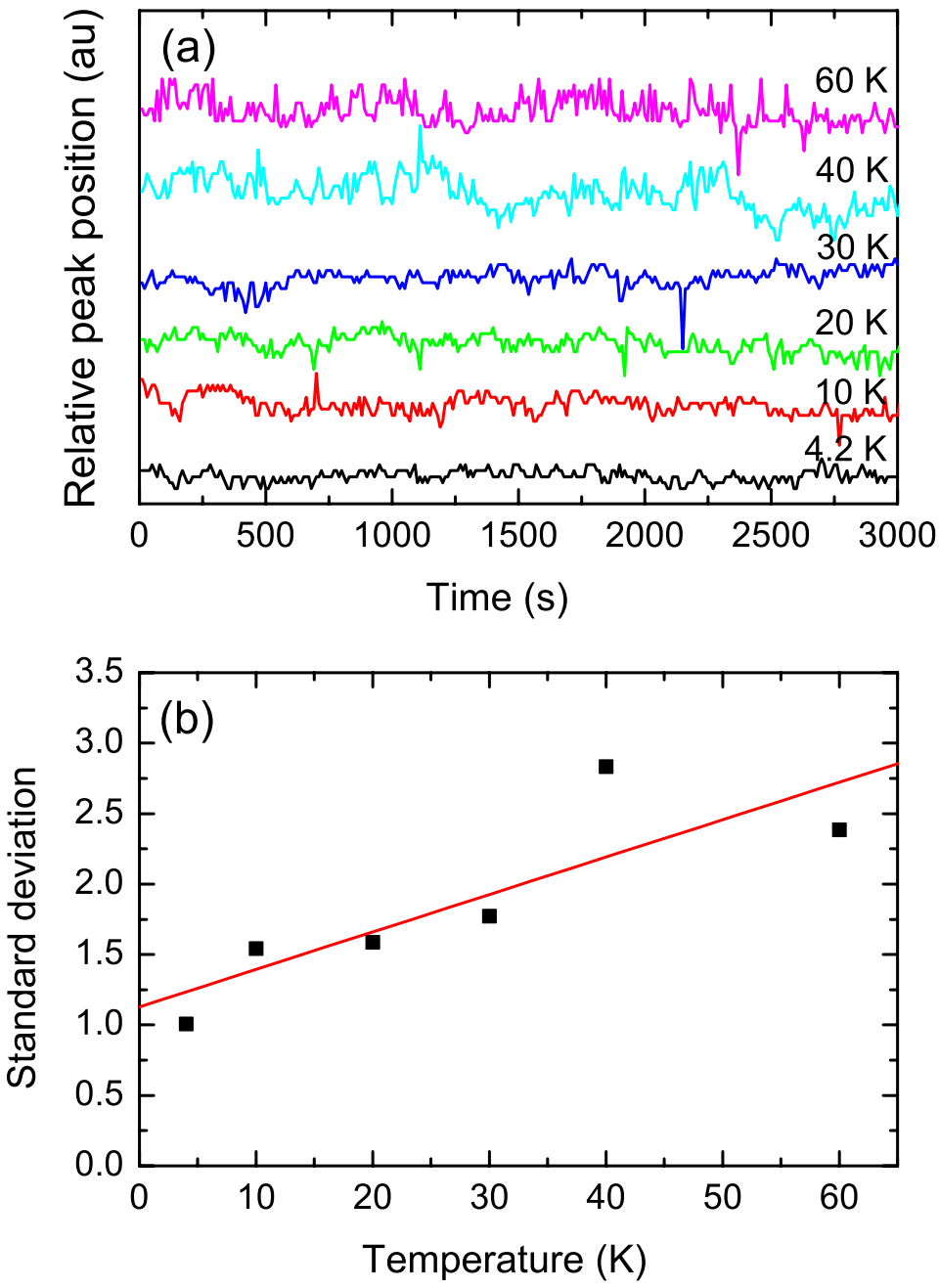


Figure 5.15: (a) The changes in the relative energy position of the exciton recombination peak from a single QD over a period of 3000 s, recorded at various temperatures (the traces are offset for clarity). This data was built up from sequences of spectra with an individual integration time of 10 s. Smoothing of the original time-integrated spectra was used in an attempt to track the true peak position as accurately as possible. (b) The standard deviation of the traces in (a) as a function of temperature. The solid red line is a linear fit.

lifetime was found to decrease as the temperature increased.

Despite the differences in the growth methods of Samples A and B (resulting in different QD sizes and composition), the exciton recombination lifetimes were found to be comparable in the two samples (typically ∼1–2 ns in both cases), and similar behaviour was observed as the excitation power density and temperature were varied.

Further time-integrated measurements showed that the narrowest exciton recombination line in Sample A had a FWHM of ∼290 μeV, while the narrowest exciton recombination line in Sample B had a FWHM of ∼230 μeV. This implied decoherence times of $T_2 \geq 4.5$ ps and $T_2 \geq 5.7$ ps respectively.

A second series of measurements demonstrated the presence of random fluctuations in the energy, intensity and FWHM of an exciton recombination peak from a single QD in Sample B. The fluctuations were found to be random in time (there was no evidence of periodic behaviour), and no correlation was found between changes in the peak position and its FWHM. It was, however, noted that the peak seemed to preferentially take up certain energies, suggesting that the influence of carrier confinement in a nearby trap could be inferred. As the temperature rose, there was an apparent increase in the amplitude of the fluctuations of the peak position.

The spectral diffusion measurements may have important implications for linewidth measurements in the InGaN QD system. The fluctuation of the energy of the exciton recombination peak on a timescale of seconds can be expected to lead to a broadening of the measured linewidth (which is integrated on a similar timescale) (15; 18). Therefore, it is possible the true linewidths of the exciton recombination peaks from single InGaN QDs may be in fact

much narrower than their measured values, and that consequently the true values of T_2 may be much larger than those which have been calculated.

References

[1] Data acquired by Dr James Rice (private communication).

[2] I. L. Krestnikov, N. N. Ledentsov, A. Hoffmann, D. Bimberg, A. V. Sakharov, W. V. Lundin, A. F. Tsatsul'nikov, A. S. Usikov, Zh. I. Alferov, Yu. G. Musikhin and D. Gerthsen, *Phys. Rev. B* **66**, 155310 (2002).

[3] J. Simon, E. Martinez-Guerrero, C. Adelmann, G. Mula, B. Daudin, G. Feuillet, H. Mariette and N. T. Pelekanos, *Phys. Stat. Sol. (b)* **224**, 13 (2001).

[4] P. Borri, W. Langbein, J. Mørk, J. M. Hvam, H. Heinrichsdorff, M.-H. Mao and D. Bimberg, *Phys. Rev. B* **60**, 7784 (1999).

[5] C. Kammerer, C. Voisin, G. Cassabois, C. Delalande, Ph. Roussignol, F. Klopf, J. P. Reithmaier, A. Forchel and J. M. Gérard, *Phys. Rev. B* **66**, 041306 (2002).

[6] C. Kammerer, C. Voisin, G. Cassabois, C. Delalande, Ph. Roussignol, J. P. Reithmaier and J. M. Gérard, *Physica E* **17**, 7 (2003).

[7] J. Seufert, R. Weigand, G. Bacher, T. Kummell, A. Forchel, K. Leonardi and D. Hommel, *Appl. Phys. Lett.* **76**, 1872 (2000).

[8] R. Flach, D. S. Hamilton, P. M. Selzer and W. M. Yen, *Phys. Rev. Lett.* **35**, 1034 (1975).

[9] A. Szabo and R. Kaarli, *Phys. Rev. B* **44**, 12307 (1991).

[10] W. P. Ambrose and W. E. Moerner, *Nature* **349**, 225 (1991).

[11] W. P. Ambrose, Th. Basché and W. E. Moerner, *J. Chem. Phys.* **95**, 7150 (1991).

[12] H. Bach, A. Renn, G. Zumofen and U. P. Wild, *Phys. Rev. Lett.* **82**, 2195 (1999).

[13] S. A. Empedocles, D. J. Norris and M. G. Bawendi, *Phys. Rev. Lett.* **77**, 3873 (1996).

[14] S. A. Empedocles and M. G. Bawendi, *Science* **278**, 2114 (1997).

[15] S. A. Empedocles and M. G. Bawendi, *J. Phys. Chem. B* **103**, 1826 (1999).

[16] S. A. Blanton, M. A. Hines and P. Guyot-Sionnest, *Appl. Phys. Lett.* **69**, 3905 (1996).

[17] K. Leosson, J. R. Jensen, J. M. Hvam and W. Langbein, *Phys. Stat. Sol.* **221**, 49 (2000).

[18] V. Türck, S. Rodt, O. Stier, R. Heitz, U. W. Pohl, R. Engelhardt and D. Bimberg, *J. Lumin.* **87-89**, 337 (2000).

[19] H. D. Robinson and B. B. Goldberg, *Phys. Rev. B* **61**, 5086 (2000).

[20] R. Seguin, S. Rodt, A. Strittmatter, L. Reißmann, T. Bartel, A. Hoffmann, D. Bimberg, E. Hahn and D. Gerthsen, *Appl. Phys. Lett.* **84**, 4023 (2004).

[21] W. Heller, U. Bockelmann and G. Abstreiter, *Phys. Rev. B* **57**, 6270 (1998).

[22] R. A. Oliver, G. A. D. Briggs, M. J. Kappers, C. J. Humphreys, S. Yasin, J. H. Rice, J. D. Smith and R. A. Taylor, *Appl. Phys. Lett.* **76**, 2361 (2003).

[23] S. W. Feng, Y. C. Cheng, Y. Y. Chung, C. C. Yang, Y. S. Lin, C. Hsu, K. J. Ma and J. I. Chyi, *J. Appl. Phys.* **92**, 4441 (2002).

[24] Y. Narukawa, Y. Kawakami, S. Fujita and S. Nakamura, *Phys. Rev. B* **55**, 1938 (1997).

[25] E. W. Weisstein, 'Correlation Coefficient', from *MathWorld* – A Wolfram Web Resource.

Chapter 6

Selectively-grown InGaN quantum dots

6.1 Introduction

The growth methodology of selectively-grown InGaN QDs in general, and of Sample C in particular, was discussed in detail in Chapter 2. In that Chapter, SEM and white-light microscope images of the sample surface were presented. In this Chapter, we shall discuss data obtained from Sample C using cathodoluminescence (CL) hyper-spectral imaging and μ-PL spectroscopy.

6.2 Cathodoluminescence hyper-spectral imaging

6.2.1 Introduction to cathodoluminescence and hyper-spectral imaging

As discussed previously, in μ-PL spectroscopy a high-intensity beam of light is used to generate electron-hole pairs in a sample. Photons (luminescence) are then emitted as the

excited carriers radiatively recombine.

In CL spectroscopy, by contrast, excitation is generated using a focused beam of high-energy electrons (usually from either an SEM or a scanning transmission electron microscope (STEM)) (1).

The penetration depth of the electron beam into the sample is determined by the magnitude of the accelerating voltage which is used to generate it: the larger the voltage, the greater will be the penetration, allowing the sample to be probed at a greater depth. Accelerating voltages usually lie in the range of hundreds of volts to several kV, and the range of penetration depths is typically from a few tenths of a μm to several μm.

The spatial resolution which can be obtained using CL is limited by the diffusion of the created electron-hole pairs, and is therefore determined by the accelerating voltage. A lower accelerating voltage gives a smaller generation volume in the sample, and thereby a potentially higher spatial resolution.

A technique known as *hyper-spectral imaging* may be used to build up an image of the features on a particular sample. In hyper-spectral imaging, a large number of spectra are recorded at different positions (pixels) across the sample. Analysis of these individual spectra allows the energies and intensities of certain spectral features to be extracted. An image is then built up in which one of the parameters associated with a particular spectral feature is plotted as a function of position.

6.2.2 Measurements using cathodoluminescence hyper-spectral imaging

CL measurements on Sample C were performed by co-workers at the University of Strathclyde. CL hyper-spectral imaging was carried out in a modified *Cameca* 'SX100' electron probe microanalyzer, in which emitted light was collected using an optical microscope that was coaxial and confocal with the electron beam (2). The sample position was scanned in 100 nm steps with respect to the stationary beam, with the room-temperature CL spectrum being recorded at each position using a 0.125 m spectrometer and a cooled CCD array. A 500 pA beam with an accelerating voltage of 5 kV was used, with an integration time of 200 ms per pixel. The interaction width of the beam striking the sample surface was estimated as ∼100 nm.

Figure 6.1 (3) shows subsets of a single room-temperature CL hyper-spectral image of a micropyramid. Figure 6.1(a) shows a spectrum recorded from the centre of one of the micropyramid facets, exhibiting strong QW luminescence at ∼2.8 eV together with a weaker 'yellow band' centred at ∼2.2 eV. Figure 6.1(b) shows (on the same scale) a spectrum recorded at the apex, in which an additional peak at 2.37 eV is present. For each of these spectra, Gaussians were fitted to each of the peaks using non-linear regression. This was then repeated for each pixel position in the scan, allowing low-noise images to be assembled representing the spatial dependence of the spectral features.

Figures 6.2(a) and (c) (3) show respectively the intensity and energy of the QW luminescence as a function of position. This luminescence is seen to emanate from the entire surface of the micropyramid except for the apex. (In Figure 6.2(a), the symmetric 'halo' effect of

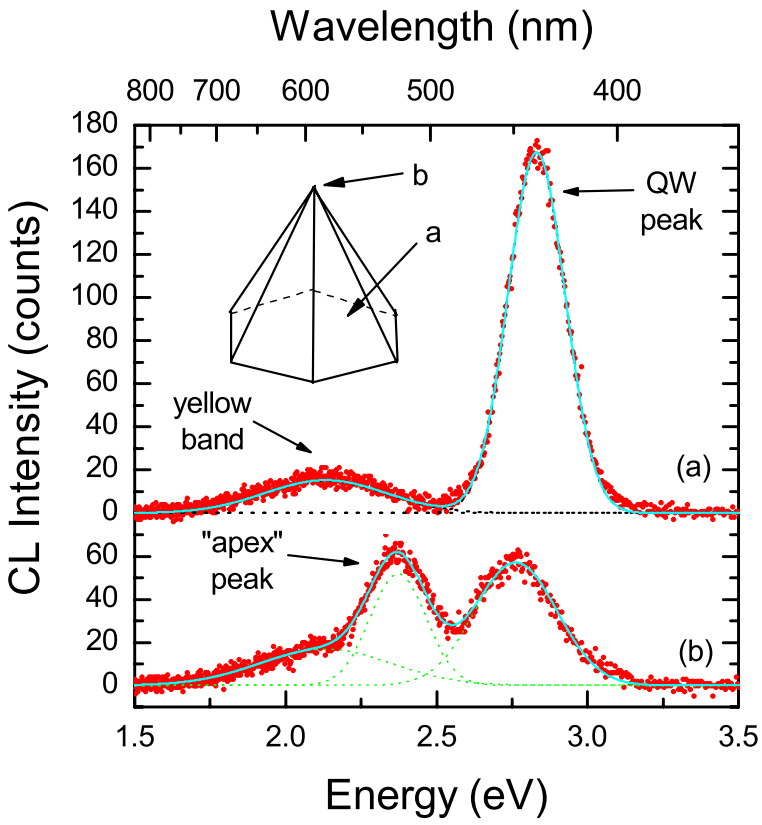


Figure 6.1: Representative room-temperature CL spectra extracted from points on the hyper-spectral image, showing the emission (a) from a facet centre, and (b) from the apex (3). The solid blue lines show the results of fitting three Gaussian peaks to each spectrum, a process repeated for each pixel position in the CL data set.

increased intensity on the facets midway between the base and apex may be attributable to waveguiding effects within the GaN micropyramid (4).) The emission energy of the QW luminescence is found to vary significantly with position (Figure 6.2(c)), decreasing with proximity to the apex. This effect is seen more clearly in a linescan through the centre of the micropyramid, shown in Figure 6.2(d), in which the shift appears linear with distance from the apex.

Relaxation of compressive strain with increasing growth thickness may be expected to contribute to the observed red-shift in the QW luminescence (5), but such an effect would not

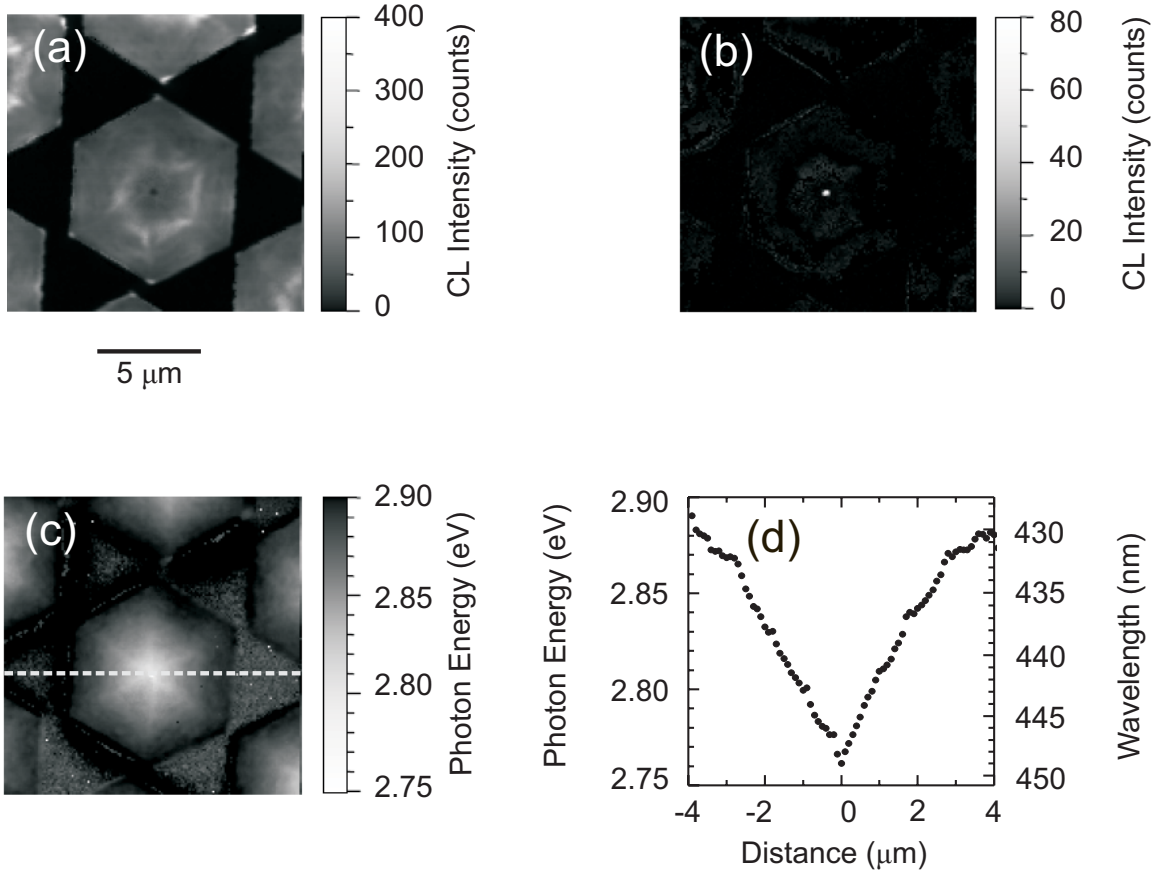


Figure 6.2: Images constructed from parameters determined by fitting three Gaussian peaks to each of the 150 × 150 spectra in the CL hyper-spectral image. (a) and (c) show the intensity and energy respectively of the QW emission from the facets, while (b) shows the intensity of the 2.37 eV apex-related band (3). The linescan (d), showing the QW luminescence energy varying across the micropyramid, was extracted from a horizontal line (shown schematically) through the apex in (c).

be expected to persist to the apex (at a height of $\sim$8 μm). The red-shift is, however, consistent with the occurrence of temperature gradients during QW growth: the In fraction x in $In_xGa_{1-x}N$ increases strongly with decreasing growth temperature, resulting in more In being incorporated at the topographic extremes, where radiative thermal losses are higher. The higher In content results in a smaller band gap.

Figure 6.2(b) shows the intensity of the apex-related 2.37 eV peak (as seen in Figure 6.1(b)). This observation is similar to that made by Tachibana *et al.* (6) at room temperature on comparable structures (allowing for a peak shift due to a different $In_xGa_{1-x}N$ composition), which was interpreted as evidence of QD formation. However, in order to distinguish directly between genuine QD emission and other possible luminescence sources (e.g. defects), low-temperature μ-PL measurements are required.

6.3 Micro-photoluminescence spectroscopy

6.3.1 Introduction

μ-PL measurements were made by the author using the high-resolution μ-PL set-up. Optical excitation was provide by an ultrafast Ti:Sapphire laser, frequency-tripled to a wavelength of 266 nm. The resulting PL was directed in turn to one of two *Spex* 'Minimate' spectrometers. One of the spectrometers was equipped with a CCD detector for time-integrated measurements, and the other was fitted with the time-correlated single photon counting system for time-resolved measurements.

6.3.2 Time-integrated measurements

Figure 6.3(a) shows a time-integrated μ-PL spectrum obtained from the apex of a single micropyramid at 4.2 K. This PL spectrum reveals sharp peaks characteristic of localized states, as previously observed in PL from single self-assembled InGaN QDs (7; 8). The FWHM of the peaks was found to be as small as $\sim$650 μeV (a value limited by the resolution of the spectrometer). Figure 6.3(b) shows a series of time-integrated μ-PL spectra recorded at different positions on the sample surface. The laser spot was sequentially focused on adjacent micropyramid apices and on points midway between apices. Sharp peaks were observed at the centres of each of the micropyramids (ii, iv, vi...), but not elsewhere on the sample (i, iii, v...). These observations show that QDs are present at the micropyramid apices where the facet QW planes intersect.

The spectrum shown in Figure 6.3(a) exhibits one strong peak and four weaker peaks. It is unclear whether the weaker peaks are due to higher-order exciton processes in a single QD, or to exciton transitions in the several QDs expected to be present at the micropyramid tip.

It should be noted that the sharp peaks in Figure 6.3 do not appear in the same spectral region as the broad apex-related CL peak seen in Figure 6.1(b), even after allowing for the difference in temperature. Moreover, the intensities of the sharp QD peaks were found to diminish rapidly with increasing temperature, becoming undetectable above $\sim$70 K, as shown in Figure 6.4. It must therefore be concluded that the luminescence emitted from the apex region *at room temperature* does not itself indicate the presence of QDs (as was previously reported (6)), but is instead defect-related. The red-shifting of the sharp μ-PL QD peaks with respect to the QW luminescence seen in CL spectra is likely to result from

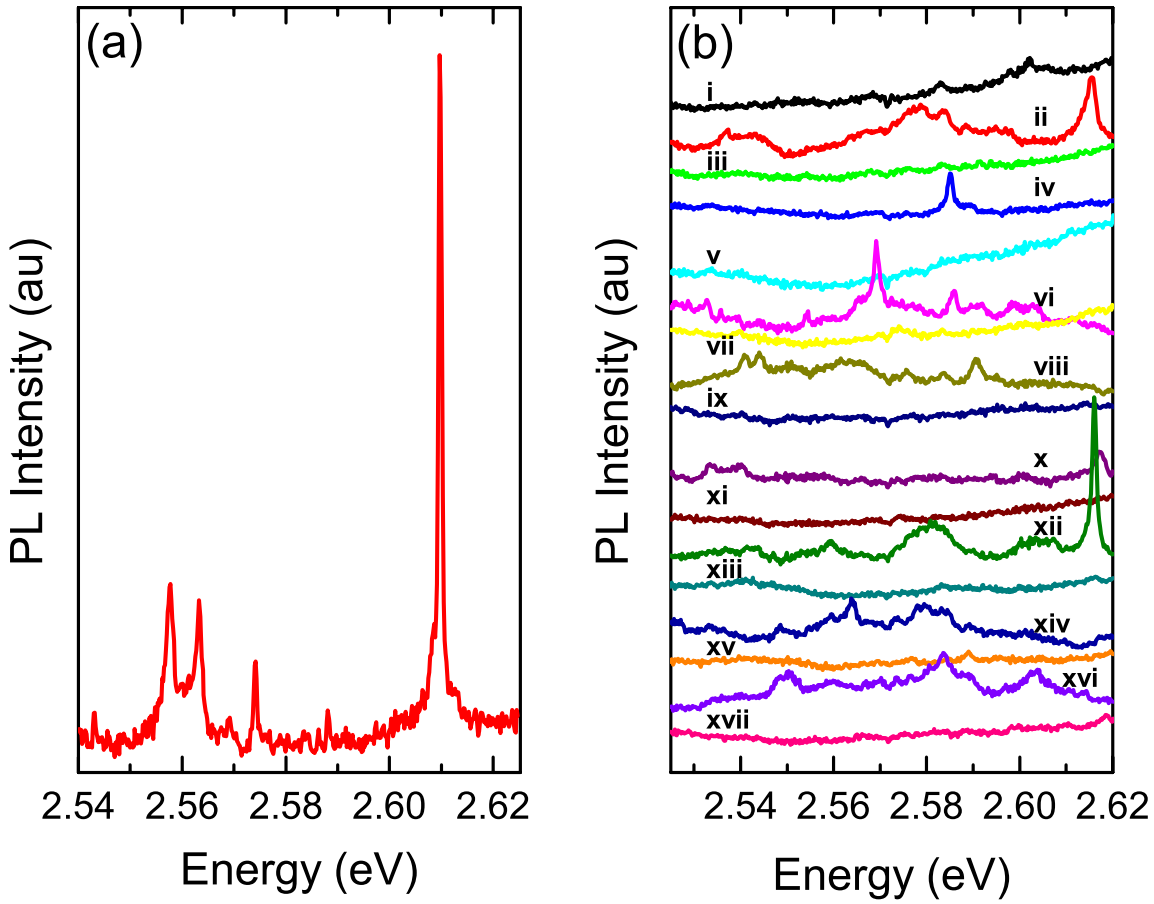


Figure 6.3: μ-PL spectra obtained at 4.2 K from Sample C. The spectrum recorded from the apex of a single micropyramid (a) exhibits several very sharp lines corresponding to exciton-related optical transitions. A series of spectra (b) were recorded in 5 μm steps across the sample surface: i, iii, v, vii, ix, xi, xiii, xv, and xvii are spectra recorded at positions between the apices of each micropyramid; whereas ii, iv, vi, viii, x, xii, xiv, and xvi show spectra recorded at the apices.

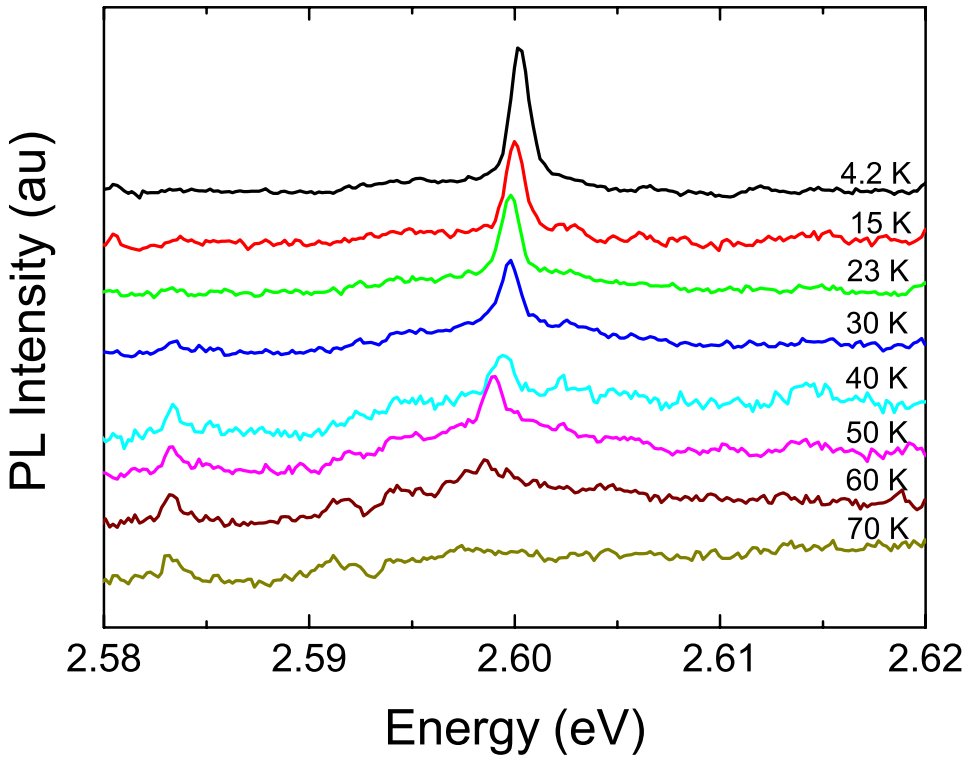


Figure 6.4: PL from a single QD at the apex of a micropyramid in Sample C, over a temperature range of 4.2 K to 70 K. The prominent peak seen at 2.60 eV at 4.2 K becomes undetectable by 70 K. The spectra in this figure have been intensity-normalized for clarity.

larger critical dimensions and higher built-in electric fields (2).

6.3.3 Time-resolved measurements

Figure 6.5(a) displays a time-integrated μ-PL spectrum from a single QD located at the apex of a GaN/InGaN micropyramid, showing a sharp peak at 2.633 eV (marked α) superimposed upon a strong background. The background originates from excitation of the side QW near the QD. It is expected that the PL decay trace recorded for the single QD will possess a dynamic profile with contributions from both the QW and the QD, in the same way that spectra from single self-assembled InGaN QDs include background emission from the

underlying WL. Since the single QD emission is sharp, monitoring the PL at ∼6 meV on each side of the energy corresponding to that of the QD (at β and γ shown in Figure 6.5(a)) produces PL exclusively from the QW. Because the properties of the QW change only slowly with energy, it is possible to use the time-resolved traces on each side of the QD emission to correct for the QW emission collected at the same spectral position as the QD emission, as discussed in Section 5.2.

The QW-subtracted decay profile of the single QD is shown in Figure 6.5(b), and is seen to be non-exponential (as shown by the failure of the straight-line fit). The decay trace from the QW was also found to be non-exponential, in agreement with previous measurements (9). The QW-subtracted trace from the QD closely matched that observed from the QW.

An approximate value for the decay time of the subtracted QD trace was found by fitting a straight line to the initial portion of the decay trace, plotted on a logarithmic scale. This gave ∼0.4 ns. This is considerably shorter than the lifetimes of ∼2 ns reported for InGaN QDs grown by self-assembly techniques (10). The shorter exciton recombination time in selectively-grown QDs is believed to be due to the stronger coupling of the zero-dimensional QD state to the side QWs in this system, in contrast to self-assembled nanostructures where the QD is relatively decoupled from the underlying WL.

6.4 Summary and conclusion

Selective growth can be a valuable tool since it allows the fabrication of QDs at precise locations determined by the grower, as opposed to the random positioning which is inevitable for self-assembled QDs.

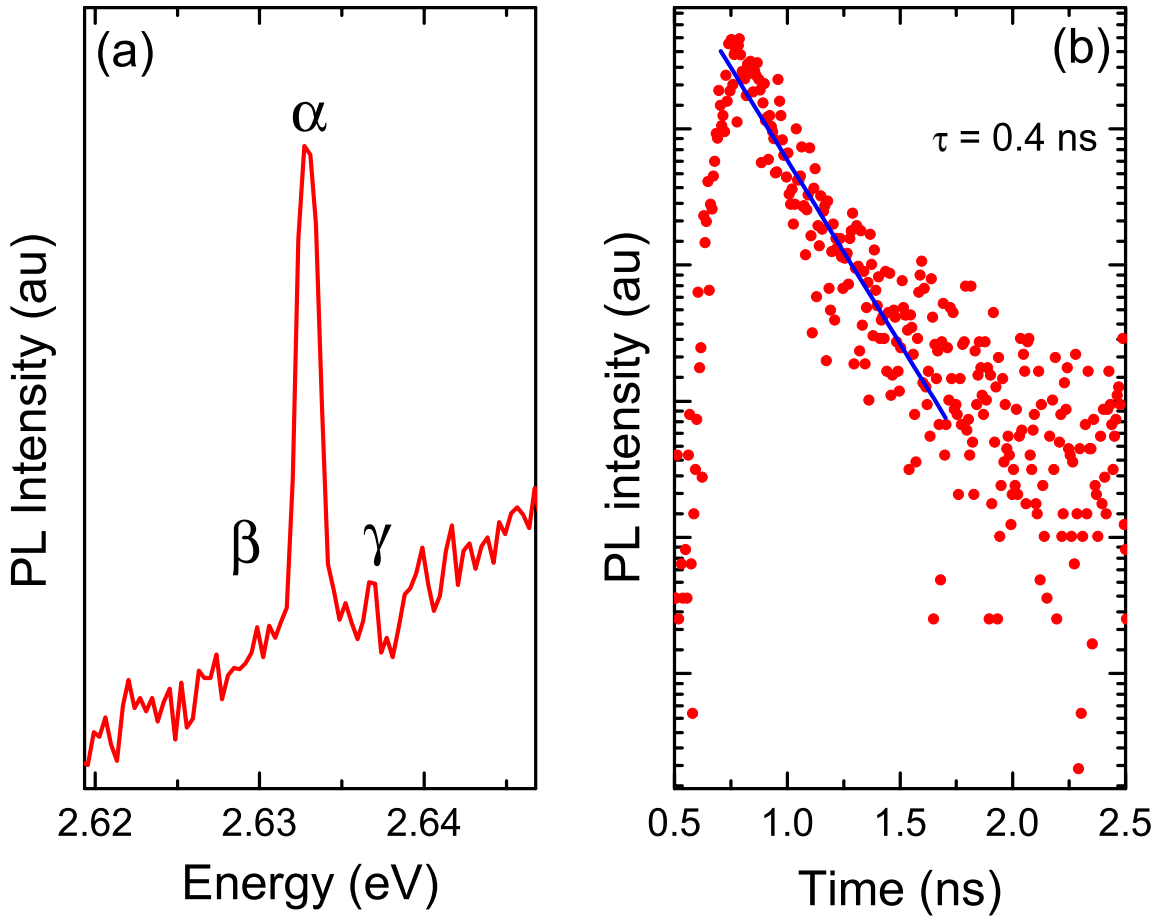


Figure 6.5: μ-PL from a single selectively-grown QD at 4.2 K. The time-integrated spectrum (a) shows a sharp peak at 2.633 eV originating from an optical transition in a single QD. The time-resolved decay trace (b) for this peak (plotted here on a logarithmic scale) was obtained by recording QW traces at β and γ (respectively $\sim$6 meV below and $\sim$6 meV above the energy of the QD emission) and subtracting the average of these traces from that recorded at the QD peak, α. The integration times at α, β and γ were 300 s in each case.

Arrays of GaN micropyramids topped with multiple InGaN QWs have been grown previously by a number of groups, and there has been indirect evidence of QD formation in these structures. The presence of a blue-shifted peak in the PL spectrum and the small spatial size of the emitting region associated with the blue-shifted component both suggested the existence of strongly-localized states. However, our work has been the first to directly demonstrate the existence of QDs in these selectively-grown structures since, for the first time, sharp lines have been observed in the μ-PL spectrum. The temperature behaviour of the sharp lines (they 'wash out' by $\sim$70 K) provides further evidence of QD-like behaviour.

Time-resolved measurements of these QDs reveal exciton recombination lifetimes of $\sim$0.4 ns, considerably shorter than the lifetimes found in self-assembled InGaN QDs. The relatively short exciton recombination lifetime is believed to be due to the strong coupling of the QD to the side QW, and there is a close similarity between the μ-PL decay traces from these regions. This is in contrast to decay traces from self-assembled InGaN QDs, where the QD shows a much clearer separation from the underlying WL.

References

[1] A. Gustafsson, M.-E. Pistol, L. Montelius and L. Samuelson, *J. Appl. Phys.* **84**, 1715 (1998).

[2] R. W. Martin, P. R. Edwards, K. P. ODonnell, M. D. Dawson, C.-W. Jeon, C. Liu, G. R. Rice and I. M. Watson, *Phys. Stat. Sol. A* **201**, 665 (2004).

[3] This data was obtained at the University of Strathclyde by Dr Robert Martin, *et al.*

[4] H. X. Jiang, J. Y. Lin, K. C. Zeng and W. Yang, *Appl. Phys. Lett.* **75**, 763 (1999).

[5] F. Bertram, J. Christen, M. Schmidt, K. Hiramatsu, S. Kitmura and N. Sawaki, *Physica E* **2**, 552 (1998).

[6] K. Tachibana, T. Someya, S. Ishida and Y. Arakawa, *Appl. Phys. Lett.* **76**, 3212 (2000).

[7] R. A. Oliver, G. A. D. Briggs, M. J. Kappers, C. J. Humphreys, J. H. Rice, J. D. Smith and R. A. Taylor, *Appl. Phys. Lett.* **83**, 755 (2003).

[8] O. Moriwaki, T. Someya, K. Tachibana, S. Ishida and Y. Arakawa, *Appl. Phys. Lett.* **76**, 2361 (2000).

[9] I. L. Krestnikov, N. N. Ledentsov, A. Hoffmann, D. Bimberg, A. V. Sakharov, W. V. Lundin, A. F. Tsatsul'nikov, A. S. Usikov, Z. I. Alferov, Y. G. Musikhin and D. Gerthsen, *Phys. Rev. B* **66**, 155310 (2002).

[10] J. W. Robinson, J. H. Rice, A. Jarjour, J. D. Smith, R. A. Taylor, R. A. Oliver, G. A. D Briggs, M. J. Kappers, C. J. Humphreys and Y. Arakawa, *Appl. Phys. Lett.* **83**, 2674 (2003).

Chapter 7

Exciton complexes in InGaN quantum dots

7.1 Introduction

The concept of exciton complexes was introduced in Chapter 2. It was explained how carriers which are optically pumped into the bulk of a semiconductor can diffuse through the semiconductor matrix and become trapped in QDs. Different exciton complexes were seen to arise from different combinations of trapped carriers. These complexes included the single exciton (X) consisting of a single electron-hole pair, the negatively-charged exciton (X^-) consisting of two electrons and one hole, the positively-charged exciton (X^+) consisting of one electron and two holes, and the biexciton (XX) consisting of two electrons and two holes.

Exciton complexes have been experimentally observed in μ-PL spectra from various QD systems, including GaAs/AlGaAs (1), InAs/GaAs (2; 3), InAs/AlGaAs (4) and InAs/InP (5).

7.2 Exciton complexes in single nitride quantum dots

7.2.1 Introduction

As already discussed in Section 3.2.2, the first μ-PL study of X recombination in a single InGaN QD was performed in 2000 (6). In 2004, XX recombination was observed in the μ-PL spectrum from localized states in an InGaN/GaN quantum well (7; 8). In (7), the XX line was found to be *blue-shifted* relative to the X line by 4.4 meV, and in (8) the exciton–biexciton splitting was found to take both positive and negative values depending on the particular QD examined. No evidence for XX recombination in single *self-assembled* InGaN QDs has been reported in the literature. However, in 2004 μ-PL spectroscopy of self-assembled GaN/AlN QDs demonstrated the presence of XX states in the system (9). The XX line was again found to be *blue-shifted* relative to the X line, in this case by $\sim$30 meV.

7.2.2 Theoretical calculations of exciton complex recombination energies

In order to demonstrate the existence of X, X^-, X^+ and XX states in single self-assembled InGaN QDs, it is very useful to know the expected energy separation of the various recombination lines. To find expected values for these splittings, theoretical calculations were carried out by David Williams and Prof Eoin O'Reilly of University College Cork, Ireland, in co-operation with Dr Aleksey Andreev of the University of Surrey.

The X, X^-, X^+ and XX wavefunctions and energies were calculated using a one-band Hamiltonian within the Hartree approximation, solved with an iterative self-consistent finite dif-

ference method, as explained in more detail in (10). As already discussed in Chapter 2, the wurtzite structure of InGaN is known to result in a large built-in piezoelectric field of the order of MVcm^{-1}, which increases the confinement of the wavefunctions and produces a spatial separation of the electrons and holes in the QD. This strong localization, together with the smaller dielectric constant, results in much larger Coulomb interactions in InGaN QDs than in GaAs-based QDs. The interaction energy between an electron and a hole (J_{eh}) is negative and hence tends to reduce the recombination energy, while the interaction energies between two electrons (J_{ee}) and between two holes (J_{hh}) are positive and tend to increase the recombination energy. The difference in recombination energy between the exciton and biexciton is given by

$$E_{XX} - E_X \approx 2J_{eh} + J_{ee} + J_{hh}. \tag{7.1}$$

(A more detailed discussion is given in (10; 11)). In GaAs-based QDs, the magnitude of J_{eh} is comparable to but slightly larger than J_{ee} and J_{hh}, so the XX energy is red-shifted with respect to the X energy. However, in nitride-based QDs, the electron-hole separation leads to a reduction in J_{eh} and calculations showed that, for a variety of QD sizes, shapes and indium composition consistent with those observed in experiment, that $|J_{eh}| < J_{ee} < J_{hh}$. Consequently, it is expected that the XX recombination energy will be blue-shifted with respect to the X energy in III-nitride QDs. It is also expected that the magnitude of this blue-shift will decrease as the height-to-width ratio of the QD decreases, in accordance with the $\sim$5 meV blue-shift observed in a QW (7).

Using the mean QD dimensions given in (6) (assuming a QD diameter of 23.4 nm and a QD height of 4.6 nm), calculations using an indium content of 7% (Figure 7.1(a)) gave an X recombination energy of 2.819 eV and an X–XX splitting of 51 meV (12). However, it

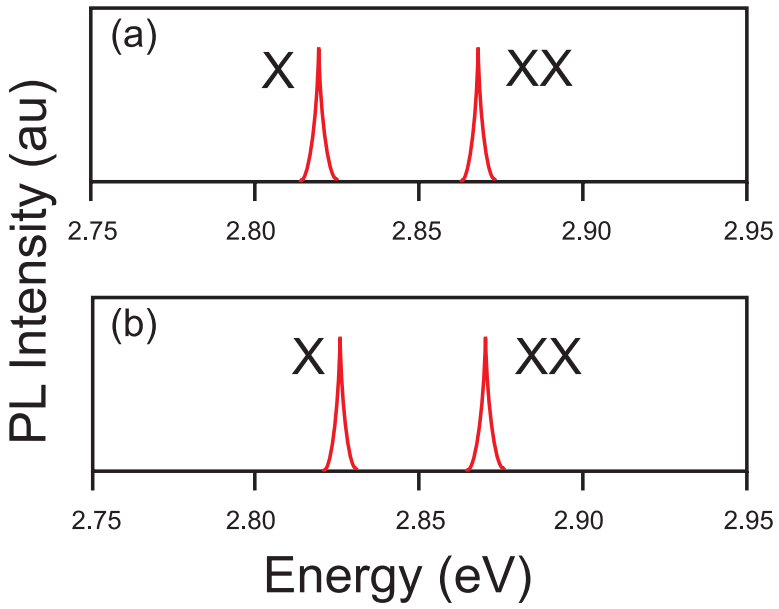


Figure 7.1: Theoretical μ-PL spectra from a single InGaN QD with height 0.93 nm and diameter 18 nm, on a 2.3 nm WL (12). The values of FWHM and intensity are arbitrary. (a) Uniform indium composition of 7%, and (b) 9% indium composition in the WL and 5.5% indium composition in the QD.

was possible that the WL and QD had different compositions. It was found that an X–XX splitting of 44 meV (see Section 7.3.2) could be obtained using 9% indium in the WL and 5.5% in the QD, with an X energy of 2.829 eV (Figure 7.1(b)).

Calculations of the expected X–X^-/X^+ splitting gave a range of values from +5 to +20 meV depending on the composition.

7.2.3 Time-integrated studies of exciton complexes in a single InGaN quantum dot

Preliminary time-integrated μ-PL measurements on Sample A were carried out by Dr James Rice of the University of Oxford, using the *Renishaw* μ-PL system. Excitation was pro-

vided by a CW He-Cd laser operating at 325 nm. Figure 7.2(a) shows a series of μ-PL spectra recorded at different excitation power densities, from (i) 3.5×10^4 Wcm^{-2} to (xi) 1.8×10 Wcm^{-2}. Three sharp peaks at 2.937 eV, 2.946 eV and 2.961 eV (marked α, β and γ respectively) are clearly visible.

Figure 7.2(b) shows the integrated intensities of the peaks shown in Figure 7.2(a) as a function of excitation power density. Peak α was assigned to X recombination since this peak is clearly visible even at the lowest excitation power densities. Peaks β and γ both appear only at higher excitation power densities, which suggests that they may be associated with higher-order exciton complexes. Moreover, the gradients in Figure 7.2(b) for peaks β and γ (before saturation) were found to be approximately twice as large as the gradient for peak α. It is well known that the intensity of an X recombination peak displays a linear dependence on excitation power density, whereas XX and X^-/X^+ recombination peaks show a quadratic relationship (13; 14).

Although α can safely be assigned to X recombination, it is difficult to be sure from the time-integrated measurements alone whether β and γ are associated with XX or X^-/X^+ recombination. However, results from the theoretical modelling can help. The theoretical calculations discussed in Section 7.2.2 indicated that the X–XX energy splitting should be $\sim$40 meV, while the X–X^-/X^+ energy splitting should be +5 to +20 meV. Thus it appears that peak β is associated with X^-/X^+ recombination (since peak β appears at an energy $\sim$9 meV greater than peak α), while peak γ is associated with XX recombination (since peak γ appears at an energy $\sim$24 meV greater than peak α).

It is not possible at this stage to differentiate experimentally between X^- and X^+ recombination, and this is not attempted. Nevertheless, there is a good basis for concluding that

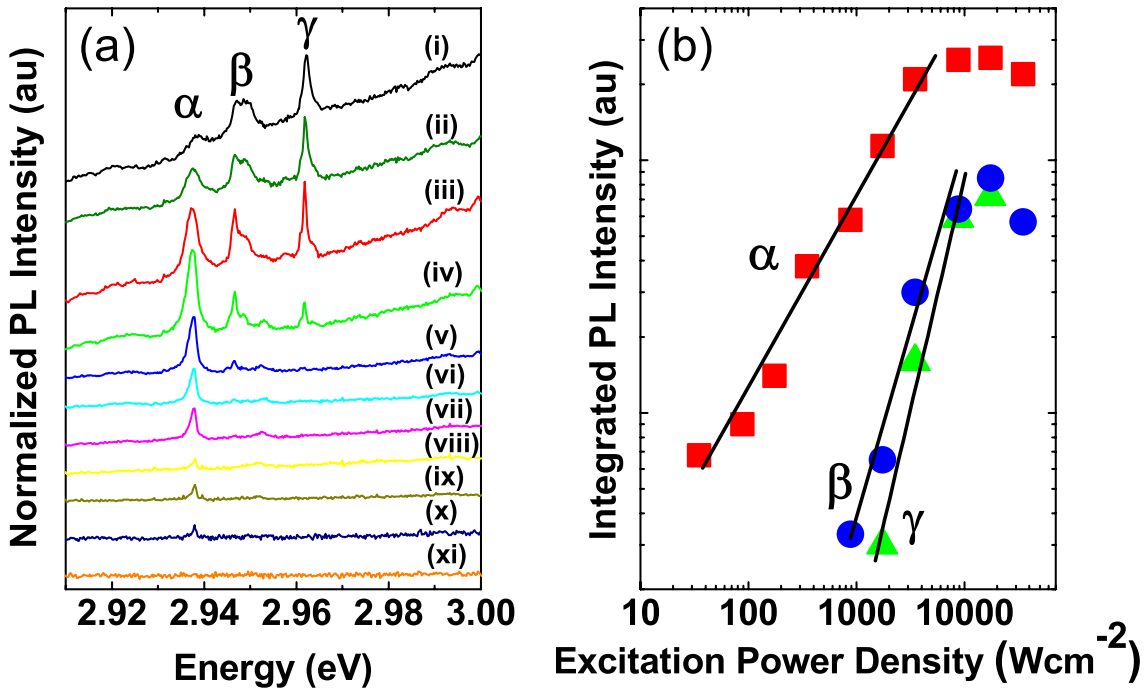


Figure 7.2: (a) Time-integrated μ-PL spectra recorded at 4.2 K from a single QD in Sample A, as a function of excitation power density (15). Three sharp peaks at 2.937 eV, 2.946 eV and 2.961 eV (marked α, β and γ respectively) are clearly visible. The excitation power densities (in Wcm^{-2}) were: (i) 3.5×10^{4}, (ii) 1.8×10^{4}, (iii) 8.8×10^{3}, (iv) 3.5×10^{3}, (v) 1.8×10^{3}, (vi) 8.8×10^{2}, (vii) 3.5×10^{2}, (viii) 1.8×10^{2}, (ix) 8.8×10^{1}, (x) 3.5×10^{1}, (xi) 1.8×10^{0}. (b) A log-log plot showing the integrated intensities of the peaks shown in (a) as a function of excitation power density (15). The gradients of the solid lines (low excitation power density regime) for α, β and γ respectively are 0.78 ± 0.1, 1.59 ± 0.4 and 1.83 ± 0.3.

peaks due to X, X^-/X^+ and XX recombination have been observed in a single InGaN QD.

7.3 Time-resolved studies of exciton complexes in a single InGaN quantum dot

7.3.1 Introduction

The time-integrated work discussed in Section 7.2.3 had established that XX peaks were observable in the μ-PL from single InGaN QDs in Sample A. Therefore, it was decided that further measurements would be carried out in order to determine the *dynamics* of X and XX recombination. This is because it is to be expected that different exciton complexes will show interesting differences in their recombination dynamics. Time-resolved studies of X^- and X^+ recombination lines were not attempted.

The time-resolved μ-PL measurements were made by the author using the high-resolution μ-PL set-up. Excitation was provided by a Ti:Sapphire laser frequency-doubled to a wavelength of 400 nm. The PL was dispersed by the *Andor* 'Shamrock' spectrometer, and time-correlated single photon counting was used to time-resolve the μ-PL signal.

7.3.2 Identification of exciton and biexciton recombination lines

An essential first step in carrying out a time-resolved study of the dynamics of X and XX states is the correct identification of a pair of PL peaks which originate from these transitions. As discussed in Section 7.2.3, a first indication that a pair of peaks is indeed due to X and XX

recombination would be the energy splitting, which should be similar to the value calculated using theoretical modelling (∼40 meV).

A second important criterion is the response of the peaks to excitation power density. As already discussed in Section 7.2.3, the intensity of an X recombination line should show a linear dependence on the excitation power density (before saturation), whereas an XX recombination line should show a quadratic dependence. Therefore, a series of time-integrated spectra from various single QDs in Sample A were recorded at a variety of excitation power densities.

Figure 7.3(a) displays time-integrated μ-PL spectra from a single QD in Sample A. This QD will be referred to as 'QD A'. The spectra were recorded at three excitation power densities: (i) 3×10^3 Wcm^{-2}, (ii) 8×10^2 Wcm^{-2} and (iii) 8×10^1 Wcm^{-2}. The spectrum at 3×10^3 Wcm^{-2} shows peaks at 2.825 eV and 2.866 eV. The energy separation of these peaks is 41 meV, and they appear at energies close to the ∼2.85 eV predicted by theoretical modelling. This suggests that they could be associated with X and XX processes, provided that their intensities show the correct dependence on excitation power density.

Figure 7.3(b) shows the intensities of the two peaks as a function of excitation power density. Calculation of the gradient for the peak at 2.825 eV showed linear power dependence, with an exponent of 0.96±0.2, while the peak at 2.866 eV showed quadratic power dependence, with an exponent of 2.02±0.4. Since these gradients closely match the expected values for X and XX recombination lines, the peaks at 2.825 eV and 2.866 eV were assigned to X and XX transitions respectively.

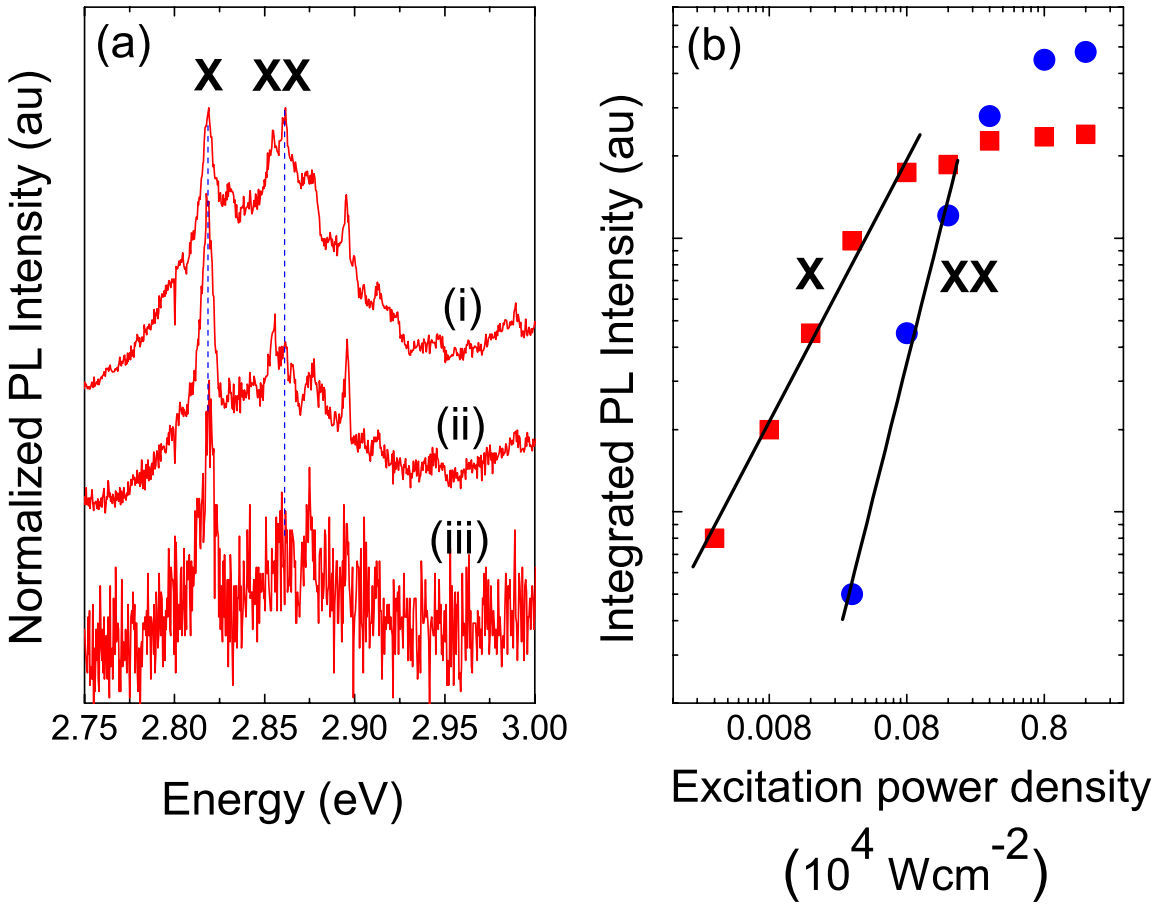


Figure 7.3: Time-integrated μ-PL from single QD A, recorded at 4.2 K. In each case, the individual integration time was 10 s. (a) μ-PL recorded at a variety of excitation power densities: (i) 3×10^3 Wcm^{-2}, (ii) 8×10^2 Wcm^{-2} and (iii) 8×10^1 Wcm^{-2}. The peaks at 2.825 eV and 2.866 eV are assigned to X and XX transitions respectively, as discussed in the text. (b) Dependence of the peak intensity of the X and XX lines on the excitation power density (log-log scale). The gradient of the solid line for X (low excitation power density regime) is 0.96±0.2, and the gradient of the solid line for XX (low excitation power density regime) is 2.02±0.4.

7.3.3 Time-resolved exciton and biexciton measurements

Figures 7.4(a) and (b) show time-resolved μ-PL decay traces from QD A, recorded at 4.2 K. Figure 7.4(a) shows the trace from the XX (recorded at 2.866 eV) and Figure 7.4(b) shows the trace from the X (recorded at 2.825 eV). In both cases, the excitation power density was 3×10^2 Wcm^{-2}. Since the recorded decay trace of an X or XX peak consists of emission from the underlying WL as well as from the QD, the decay traces for both X and XX underwent background subtraction using the method described in Chapter 5. By recording WL traces $\sim$12.8 meV on each side of the peak in question, averaging these two traces and subtracting from the X or XX signal, a background-subtracted decay profile for an X or XX in a single QD was produced.

In Figure 7.4(a), the subtracted XX trace shows a mono-exponential decay with no rounding at the peak. In Figure 7.4(b), the subtracted X trace, by contrast, shows a clear rounding effect, with the point of maximum intensity being delayed relative to that of the XX trace by $\sim$1.0 ns. Both the delay and the rounding can be attributed to the refilling of X states as XX states decay radiatively via the process XX$\rightarrow$X + photon. Such an effect has been observed previously in both arsenide-based (2; 16) and selenide-based (17; 18; 19) QD systems, and is a characteristic signature of time-resolved X and XX measurements. The clear coupling between the X and XX decay curves is evidence that the two transitions originate in the same QD.

Figure 7.4(c) shows a time-resolved background-subtracted X decay trace (recorded at 2.863 eV) from a different single QD in the same sample. This will be referred to as 'QD B'. At the power density used, no XX line was observed in this case. In contrast to the X decay trace

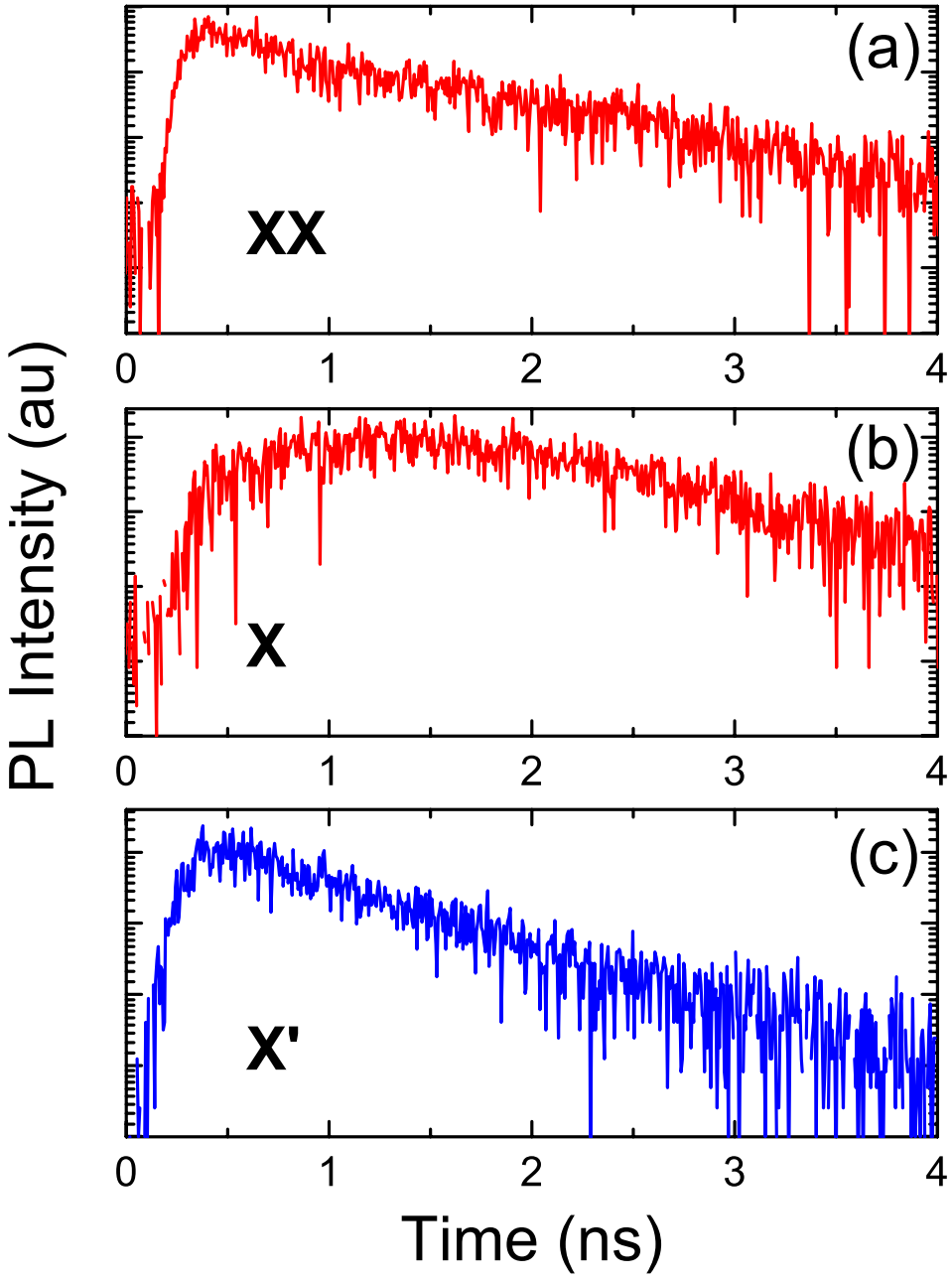


Figure 7.4: (a) and (b): Time-resolved μ-PL from single QD A, recorded at 4.2 K and at an excitation power density of 3×10^2 Wcm^{-2}. The integration time was 6000 s in each case. The traces have been obtained using the background-subtraction method described in the text. (a) PL from the XX line (at 2.866 eV). (b) PL from the X line (at 2.825 eV). (c) Time-resolved μ-PL from single QD B (in the single-exciton regime), recorded at 4.2 K. All three traces are plotted on logarithmic scales.

seen in (b), the X trace shows no rounding: the decay is found to be mono-exponential with a lifetime of 1.07 ns. This is expected as there is no XX state to cause refilling of the population of the X state in this case.

Figure 7.5 shows time-resolved background-subtracted decay traces for X and XX from QD A, recorded at two different excitation power densities (1.5×10^2 Wcm^{-2} and 3×10^2 Wcm^{-2}). Figure 7.5(a) shows the XX trace recorded at an excitation power density of 1.5×10^2 Wcm^{-2}. The XX line decays mono-exponentially with a time constant of 1.0 ns. Figure 7.5(b) shows the corresponding X trace recorded at the same excitation power density. This decays mono-exponentially with a time constant of 1.4 ns. A rounding of the X trace near the peak is observed, and the point of peak intensity for the X line is delayed relative to that of the XX line by $\sim$0.6 ns. Figure 7.5(c) and (d) respectively show the XX and X traces recorded at a higher excitation power density of 3×10^2 Wcm^{-2}. Here the delay between the peaks of the XX and X decay traces is 1.0 ns, which is longer than at the lower excitation power density, and the rounding of the X trace is more pronounced. The degree of rounding of the X trace and the delay of the X peak with respect to the XX peak are expected to be power dependent. At higher power, more XX states will be created and thus the population refilling effect will be greater. This is clearly seen in the differences between Figure 7.5(b) and 7.5(d).

The solid cyan lines in Figure 7.4(a–d) show results from a rate-equation model used to fit the decay profiles. The fitting was carried out by Kwan Lee of the University of Oxford. The aim was to explain the refilling of the X state by the XX. The populations of the XX and X states w_{XX} and w_{X} are described in terms of τ_{XX} and τ_{X} (XX and X decay lifetimes,

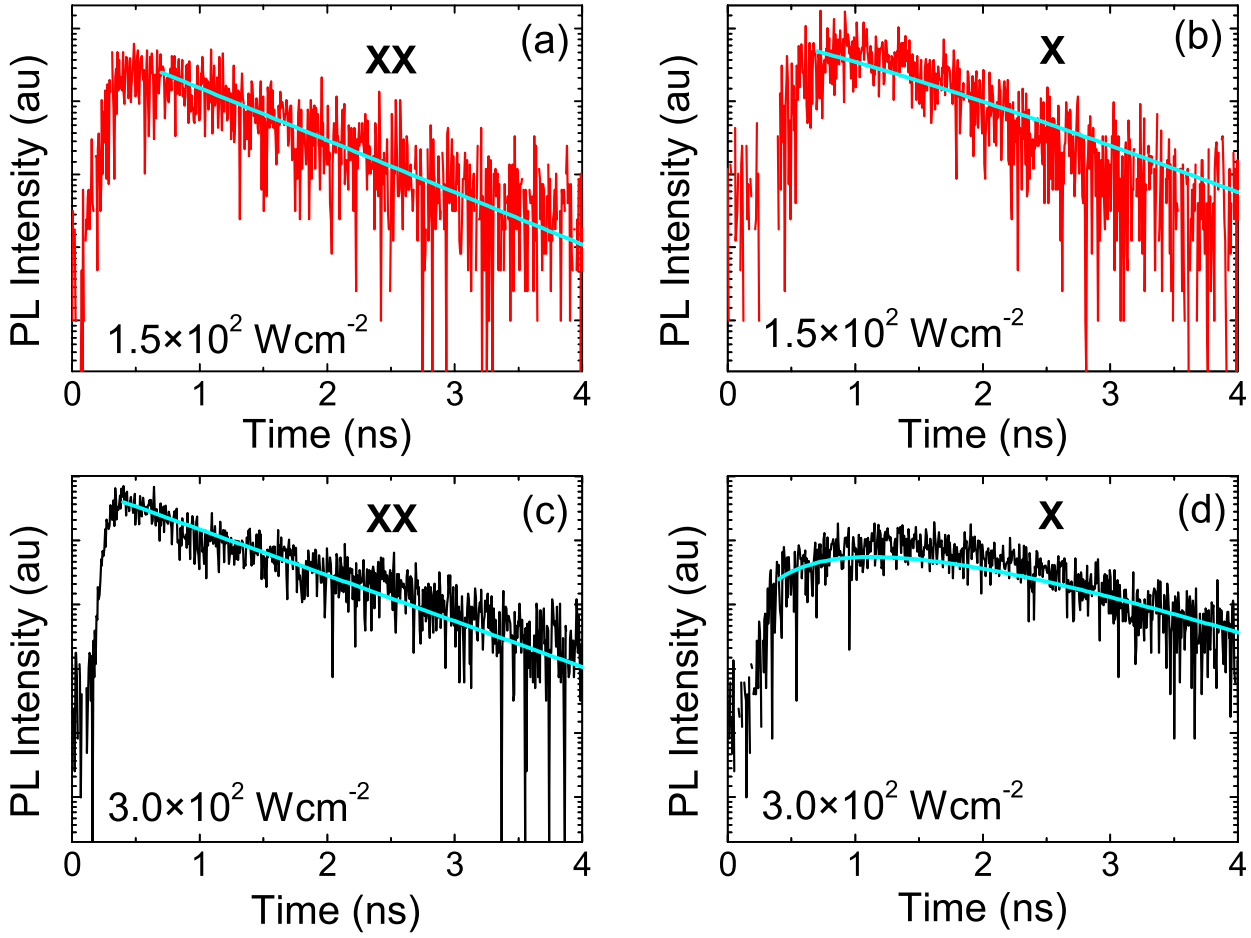


Figure 7.5: Time-resolved μ-PL from single QD A, recorded at 4.2 K with integration times of 6000 s in each case. The traces have all been obtained through the background subtraction method described in the text, and are all plotted on logarithmic scales. (a) PL recorded at an excitation power density of 1.5×10^2 Wcm^{-2}. The red trace shows the XX (recorded at 2.866 eV) and the solid cyan line represents a fit generated using a rate-equation model with temporal parameters τ_X=1.0 ns and τ_{XX}=1.4 ns, as described in the text. (b) The X (recorded at 2.825 eV) associated with the XX shown in (a), at the same excitation power density. The solid cyan line is a fit with the same parameters as in (a). (c) PL recorded at a higher excitation power density of 3×10^2 Wcm^{-2}. (This is the same data as is displayed in Figure 7.4(a).) The black trace shows the XX and the solid cyan line represents a fit generated using a rate-equation model with the same temporal parameters as in (a). (d) The X associated with the XX shown in (c), at the same excitation power density. (This is the same data as is displayed in Figure 7.4(b).) The solid cyan line is a fit with the same temporal parameters as in (a).

respectively) according to the coupled differential equations

$$\frac{\mathrm{d}w_{\mathrm{XX}}}{\mathrm{d}t} = -\frac{w_{\mathrm{XX}}}{\tau_{\mathrm{XX}}} \tag{7.2}$$

$$\frac{\mathrm{d}w_{\mathrm{X}}}{\mathrm{d}t} = -\frac{w_{\mathrm{X}}}{\tau_{\mathrm{X}}} + \frac{w_{\mathrm{XX}}}{\tau_{\mathrm{XX}}}. \tag{7.3}$$

In the low excitation power density (1.5×10^2 Wcm^{-2}) case, values of τ_{X}=1.0 ns and τ_{XX}=1.4 ns were found using this model. The result that τ_{X} and τ_{XX} are comparable is in accordance with previous experimental work on selenide-based QD systems (18; 19). In the higher excitation power density case (3×10^2 Wcm^{-2}), the same values of τ_{X}=1.0 ns and τ_{XX}=1.4 ns were again found, indicating that the X and XX lifetimes were independent of excitation power density in this range.

7.4 Summary and conclusion

Previous time-integrated experimental work by co-workers had for the first time established the presence of X, $\mathrm{X}^-/\mathrm{X}^+$ and XX states in single self-assembled InGaN QDs. Therefore, time-resolved studies on Sample A were carried out by the author in order to explore the dynamics of X and XX recombination. X and XX states were observed with a splitting energy of 41 meV, in agreement with values predicted by theoretical calculations in the Hartree approximation, using a self-consistent finite difference method. The radiative recombination lifetime of the XX (1.4 ns) was found to be longer than that of the X (1.0 ns), independent of excitation power density. Clear evidence was seen for a refilling of the X state as XX underwent radiative decay, in terms of a delay of the peak of the X decay curve relative to that of the XX curve, and a pronounced rounding of the X curve. Both effects became

more significant at higher excitation power density. The decay traces for the X and XX were found to be well-described by a rate equation model.

References

[1] G. Chen, T. H. Stievater, E. T. Batteh, X. Li, D. G. Steel, D. Gammon, D. S. Katzer, D. Park and L. J. Sham, *Phys. Rev. Lett.* **88**, 117901 (2002).

[2] R. M. Thompson, R. M. Stevenson, A. J. Shields, I. Farrer, C. J. Lobo, D. A. Ritchie, M. L. Leadbeater and M. Pepper, *Phys. Rev. B* **64**, 201302 (2001).

[3] S. Rodt, R. Heitz, A. Schliwa, R. L. Sellin, F. Guffarth and D. Bimberg, *Phys. Rev. B* **68**, 035331 (2003).

[4] J. J. Finley, A. D. Ashmore, A. Lemaître, D. J. Mowbray, M. S. Skolnick, I. E. Itskevich, P. A. Maksym, M. Hopkinson and T. F. Krauss, *Phys. Rev. B* **63**, 073307 (2001).

[5] D. Chithrani, R. L. Williams, J. Lefebvre, P. J. Poole and G. C. Aers, *Physica E* **21**, 290 (2004).

[6] O. Moriwaki, T. Someya, K. Tachibana, S. Ishida and Y. Arakawa, *Appl. Phys. Lett.* **76**, 2361 (2000).

[7] H. Schömig, S. Halm, A. Forchel, G. Bacher, J. Off and F. Scholz, *Phys. Rev. Lett.* **92**, 106802 (2004).

[8] R. Seguin, S. Rodt, A. Strittmatter, L. Reißmann, T. Bartel, A. Hoffmann, D. Bimberg, E. Hahn and D. Gerthsen, *Appl. Phys. Lett.* **84**, 4023 (2004).

[9] S. Kako, K. Hoshino, S. Iwamoto, S. Ishida and Y. Arakawa, *Appl. Phys. Lett.* **85**, 64 (2004).

[10] D. P. Williams, A. D. Andreev, D. A. Faux and E. P. O'Reilly, *Physica E* **21**, 358 (2004).

[11] D. P. Williams, A. D. Andreev and E. P. O'Reilly, *Superlattices and Microstructures* (in press).

[12] David Williams, private communication.

[13] A. Kuther, M. Bayer, A. Forchel, A. Gorbunov, V. B. Timofeev, F. Schäfer and J. P. Reithmaier, *Phys. Rev. B* **58**, 7508 (1998).

[14] V. D. Kulakovskii, G. Bacher, R. Weigand, T. Kümmell, A. Forchel, E. Borovitskaya, K. Leonardi and D. Hommel, *Phys. Rev. Lett.* **82**, 1780 (1999).

[15] This data was acquired by Dr James Rice of the University of Oxford.

[16] C. Santori, G. S. Solomon, M. Pelton and Y. Yamamoto, *Phys. Rev. B* **65**, 073310 (2002).

[17] B. Patton, W. Langbein and U. Woggon, *Phys. Rev. B* **68**, 125316 (2003).

[18] G. Bacher, R. Weigand, J. Seufert, V. D. Kulakovskii, N. A. Gippius, A. Forchel, K. Leonardi and D. Hommel, *Phys. Rev. Lett.* **83**, 4417 (1999).

[19] G. Bacher, R. Weigand, J. Seufert, N. A. Gippius, V. D. Kulakovskii, A. Forchel, K. Leonardi and D. Hommel, *Phys. Stat. Sol. (b)* **221**, 25 (2000).

Chapter 8

Electric field measurements

8.1 Introduction

As discussed in Chapter 2, it is well-known that nitride semiconductor materials exhibit a strong 'built-in' electric field ($\sim$MVcm^{-1}) in the growth (vertical) direction due to a combination of the spontaneous polarization in the equilibrium lattice and the strain-induced piezoelectric polarization. In the case of an exciton confined in a nitride QD, the field leads to a spatial separation of the electron and hole in the vertical direction, and therefore to a red-shift of the exciton recombination energy.

Applying an *external* electric field in the vertical direction to oppose the internal 'built-in' field would be expected to lead to a blue-shift of the exciton recombination energy. By the same principle, applying an external field in the opposite direction such that the 'built-in' field was reinforced would be expected to result in a further red-shift of the exciton recombination energy.

Unfortunately, applying a strong external electric field in the vertical direction is experimentally difficult. The sapphire substrates on which Sample A and Sample B were fabricated

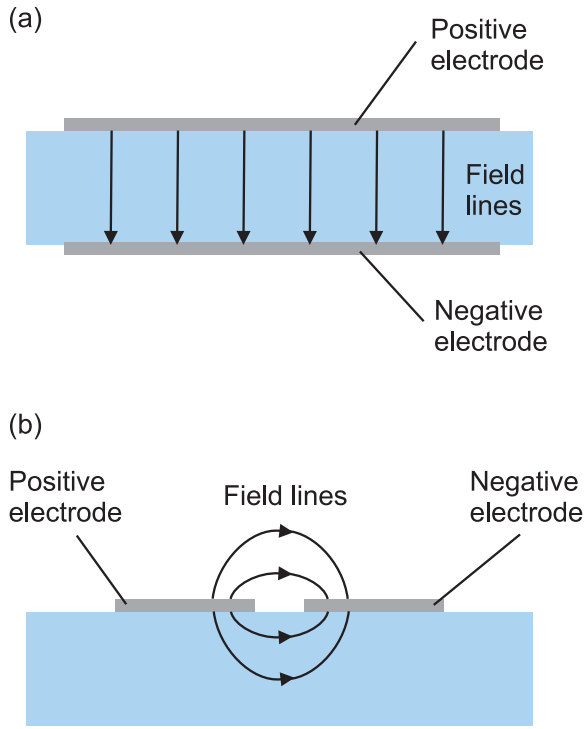


Figure 8.1: Schematic cross-sectional views of experimental arrangements which could be used for applying electric fields to the sample. (a) Electric field in the vertical direction. Electrodes are laid down on the upper and lower surfaces of the sample. A small region on the top electrode (not shown in this two-dimensional diagram) is left unmasked to allow for the collection of PL. (b) Electric field in the horizontal direction. A pair of electrodes is laid down side by side on the upper surface of the sample. PL can be collected from the unmasked area between the two electrodes.

each had a thickness of ∼1 mm. Thus, if electrodes were simply laid down on the upper and lower surfaces of the samples (as shown in Figure 8.1(a)), with a vertical separation of ∼1 mm, a voltage in the ∼MV range would be required in order to match the strength of the 'built-in' electric field. It is experimentally difficult to work with such large voltages.

An alternative approach is to apply the electric field in the *horizontal* direction using electrodes laid down on top of the sample, as shown in Figure 8.1(b). This lateral field would not directly oppose the vertical 'built-in' field, but would nevertheless be expected to lead to a shift in the exciton recombination energy since electrons and holes would experience a spatial separation in the horizontal direction.

The advantage of applying the field laterally is that the electrodes can be placed much closer together than is possible in the vertical-field case. This means that a much smaller applied voltage will be sufficient to generate an electric field of a given strength.

8.2 Previous work on electric fields

Previous work in other systems has looked at the application of external electric fields to QDs in both the vertical and lateral directions. In 1998, the effect of applying a lateral electric field to a GaAs QD formed by monolayer width fluctuations in a GaAs/GaAlAs QW was investigated (1; 2). The external field was found to cause both a red-shift of the exciton recombination peak and a reduction in its intensity. In the same year, the application of an electric field in the vertical direction to a self-assembled AlInAs QD was reported (3). Either a blue-shift or red-shift of the exciton recombination energy was observed, depending on the direction and magnitude of the applied electric field. In 2001 and 2002, the effects of applying both lateral and vertical electric fields to CdSe QDs were studied (4; 5; 6). As with lateral fields applied to the arsenide-based QDs, in CdSe QDs the exciton recombination peak was seen to red-shift and decrease in intensity with increasing electric field.

8.3 Sample preparation and estimate of field strength

In this work, lateral electric fields of various strengths were applied to QDs in Sample B. Four pairs of aluminium electrodes, each with an internal gap of 1 μm, were prepared on the sample surface by Dr David Hasko and Dr Shazia Yasin of the University of Cambridge.

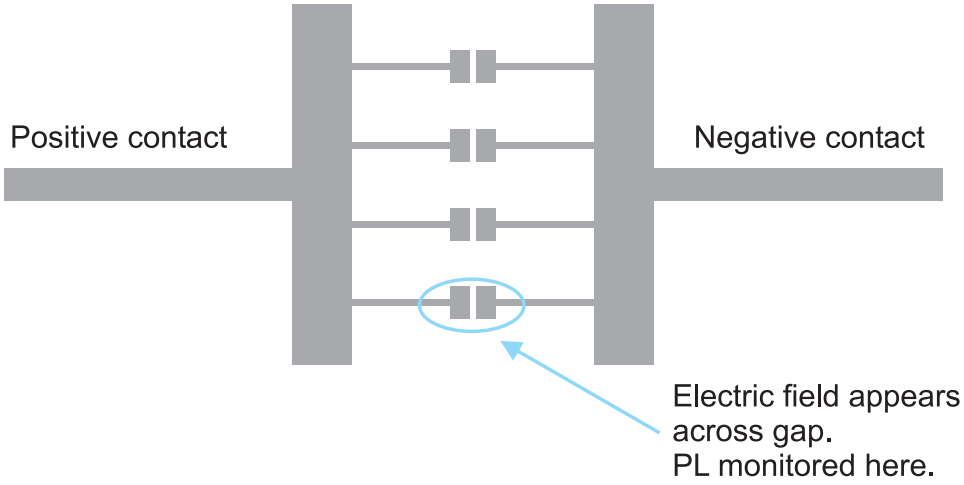


Figure 8.2: A schematic overhead view showing the layout of the electrical contacts on the surface of the sample. The four pairs of adjacent electrodes (arranged in parallel) are clearly seen. The positive and negative contacts were connected via leads to a variable voltage supply outside the cryostat.

In order to form these contacts, a 100-nm-thick aluminium layer was evaporated onto the sample surface, and an electrode pattern was fabricated by electron-beam lithography and reactive ion etching using $SiCl_4$.

Figure 8.2 shows the general layout of the contacts on the surface of the sample. The four pairs of electrodes were arranged in parallel. The gap between the two electrodes in each pair was 1 μm. A voltage could be applied using a variable external supply outside the cryostat. Figure 8.3 shows a close-up white-light microscope image (acquired using the *Renishaw* μ-PL system) of one of the pairs of electrodes.

Calculations were performed by Dr Rachel Oliver of the University of Cambridge to find the expected magnitude of the electric field across the QD layer. The ATLAS device simulation software from *Silvaco International* was used. For a bias of 10 V applied across the gap between the electrodes, the component of the expected electric field in the direction parallel to the QD layer was calculated to vary between a maximum of 0.17 $MVcm^{-1}$ and a minimum

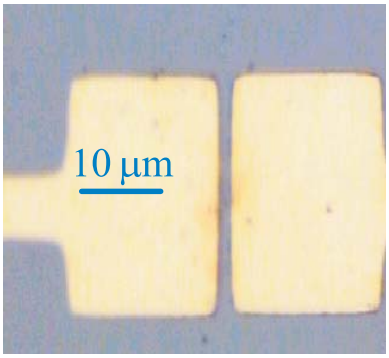


Figure 8.3: A white-light microscope image (acquired using the *Renishaw* μ-PL system) showing a pair of electrodes on the surface of Sample B. The horizontal gap between the contacts is $\sim$1 μm. When an external voltage was applied, an electric field was generated in the gap between the contacts, and PL was collected from this region.

of 0.065 MVcm^{-1}, according to position across the width of the gap. The mean field across the entire gap at this voltage was estimated to be 0.093 MVcm^{-1}. Analysis showed that the field at the middle of the gap was parallel to the QD layer, but that there was a significant component perpendicular to the QD layer at the edges of the gap. Assuming that the QDs were uniformly distributed across the gap, it was estimated that $\sim$10% of the structures would experience a significant field in the perpendicular direction.

8.4 Preliminary work

Carriers were pumped into the semiconductor bulk using optical excitation from a Ti:Sapphire laser frequency-tripled to 266 nm. The high-resolution μ-PL system was used to focus the incident laser beam on to the gap region between one of the pairs of electrodes and to collect the resulting PL, which was dispersed by the 'Shamrock' spectrometer. QDs which happened to lie in the gap experienced a lateral electric field when the external voltage was applied, and a range of different voltages was used in order to study the effects of various electric

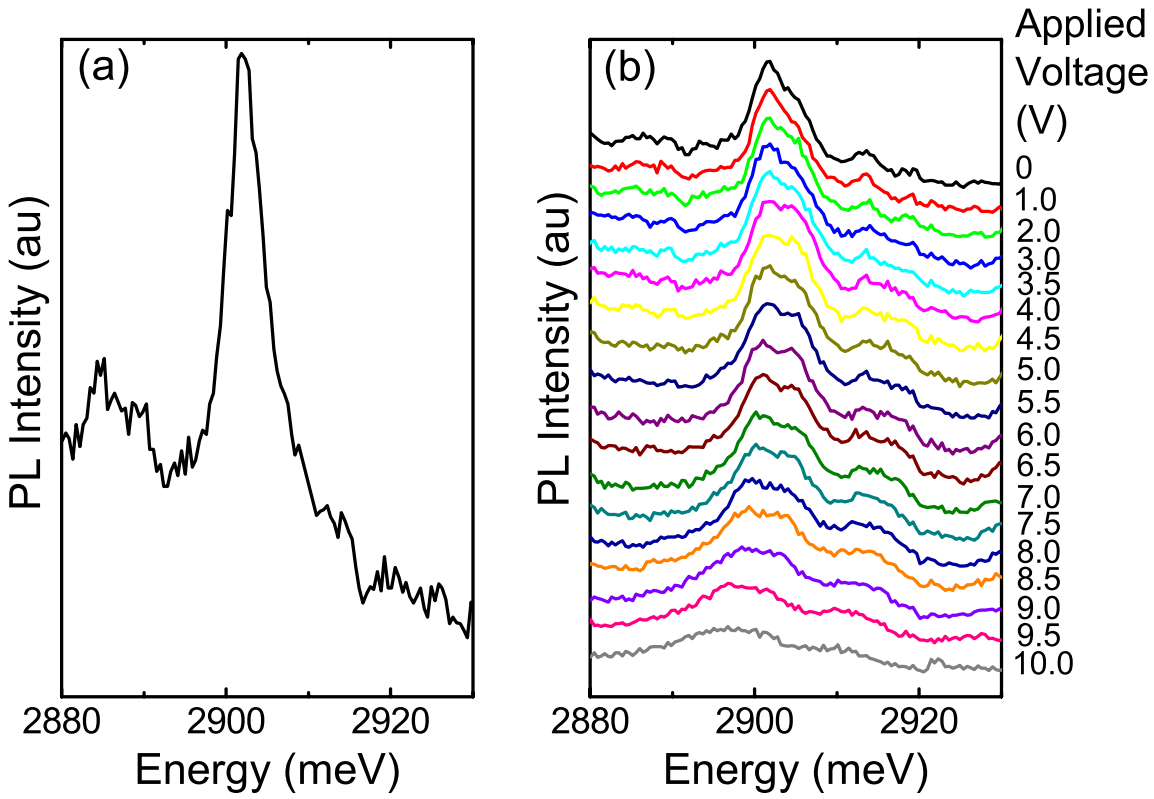


Figure 8.4: (a) A μ-PL spectrum from a single QD, recorded at 4.2 K with no external electric field. The spectrum shows a peak at 2902 meV originating from exciton recombination in a single QD. The integration time was 10 s. (b) A series of μ-PL spectra recorded sequentially with increasing externally-applied voltage, from 0 V to 10 V. The temperature was 4.2 K and the integration time was 10 s in each case.

fields upon exciton recombination.

Figure 8.4(a) shows a μ-PL spectrum from a single QD, recorded at 4.2 K. The spectrum exhibits a narrow peak at 2902 meV, originating from exciton recombination. Figure 8.4(b) shows a series of consecutively-recorded μ-PL spectra from the QD with increasing voltage. The exciton recombination peak gradually red-shifts and declines in intensity as the applied voltage is increased from 0 V to 10 V.

It is important to be certain that the effects seen in Figure 8.4(b) really are the result of the applied electric field, and that they are not due to something else. The application of voltage

across a narrow gap may cause ohmic heating. The effect of temperature upon single QDs in Sample B was discussed previously in Chapter 5. It was found that the sharp exciton recombination peaks observed in the μ-PL spectrum broadened, red-shifted and merged into the WL background as the temperature rose from 4.2 K to 60 K. However, the measurements presented in Chapter 5 indicated that the magnitudes of the temperature-induced red-shifts were less than 3 meV. This temperature-related shift is less than the shift of more than 5 meV observed when the external electric field is applied, indicating that the shifts shown in Figure 8.4(b) cannot be explained by local heating effects alone. The rapid disappearance (less than 1 s) of the field-related features in the μ-PL spectrum following the external voltage being turned off supports this conclusion. Figure 8.5 shows a series of consecutively-recorded μ-PL spectra with the applied voltage alternating between 0 V and 10 V. Even though the time interval between these spectra is very short (a few seconds), immediate recovery of the μ-PL is seen when the external field is switched off. It is also clear the shift and intensity decrease of the exciton recombination peak are completely reversible.

The relatively low resistance of the sample (of the order of a few hundred ohms) is probably due to surface transport (7). This is likely to involve a hopping mechanism, that is to say discrete charge transport between spatially separate surface traps (8). It would appear either that there is a large number of traps at the sample surface, or that the separation of the traps is small (perhaps if they arranged along a pathway such as a grain boundary).

Previous work on *spectral diffusion* in InGaN QDs (as discussed in Chapter 5) showed variations in exciton recombination peak energy due to transient QCSE shifts caused by temporally-varying locally-generated electric fields (originating from trapped carriers). These shifts in the exciton recombination energy had magnitudes of up to 1.45 meV (on a timescale

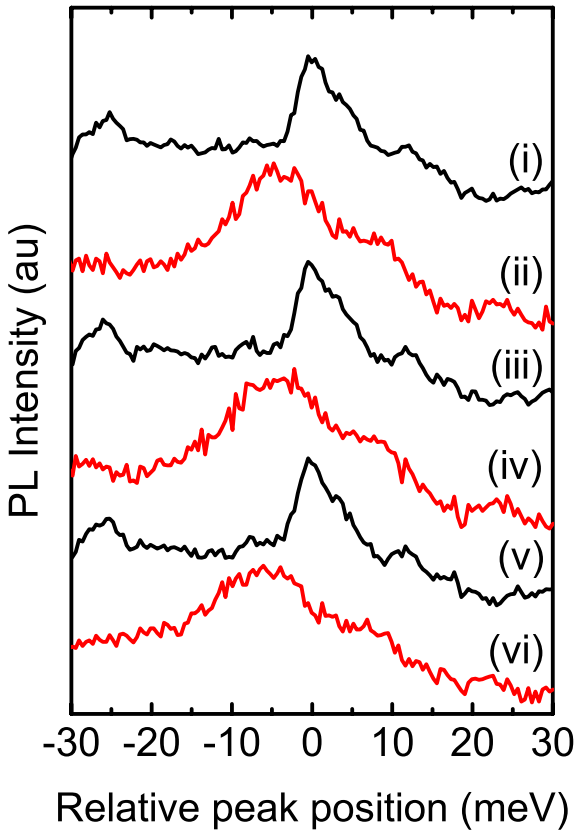


Figure 8.5: A series of six sequentially-recorded μ-PL spectra showing an optical transition in a single QD. The applied voltages were: (i) 0 V, (ii) 10 V, (iii) 0 V, (iv) 10 V, (v) 0 V and (vi) 10 V. The temperature was 4.2 K and the integration time was 10 s in each case.

of ∼1 hour). Such shifts of up to 1.45 meV in exciton energy are significantly smaller than the shifts generated by the external lateral electric field. Therefore, the contribution of the QCSE shifts associated with spectral diffusion to the shifts in exciton energies seen in this work are not considered to be significant. This means that neither ohmic heating effects nor spectral diffusion can explain the shifts seen in Figure 8.4(b).

The simulations of electric field carried out by Dr Rachel Oliver indicated that at some positions a significant component of electric field was generated in the direction perpendicular to the sample surface, in addition to the parallel component. The QD shown in Figure 8.4 may therefore be experiencing a component of external electric field parallel to its vertical internal electric field. However, since the lateral field is known to be much stronger than the vertical field at all positions, it is likely that the effect of the lateral component dominates.

8.5 Detailed analysis

The effect of the electric field upon the QD is shown in detail in Figure 8.6(a), which plots the relative peak intensity and the peak shift as a function of the applied voltage. At 10 V, there is a peak shift of 5.4 meV to lower energy compared to the zero-voltage case. This is in line with previous measurements on epitaxial arsenide-based III/V QDs and selenide-based II/VI QDs, which showed red-shifts in exciton recombination energies of up to 1.1 meV (1; 2; 4; 5; 6). Band tilting leads to a reduction in the bandgap and thus to a red-shift of the PL. The peak intensity is seen to drop from a relative value of 1.0 at 0 V to 0.4 at 10 V. This significant reduction in PL intensity is in accordance with observations made in other epitaxial QD systems (1; 2; 4; 5; 6). The application of the electric field results in

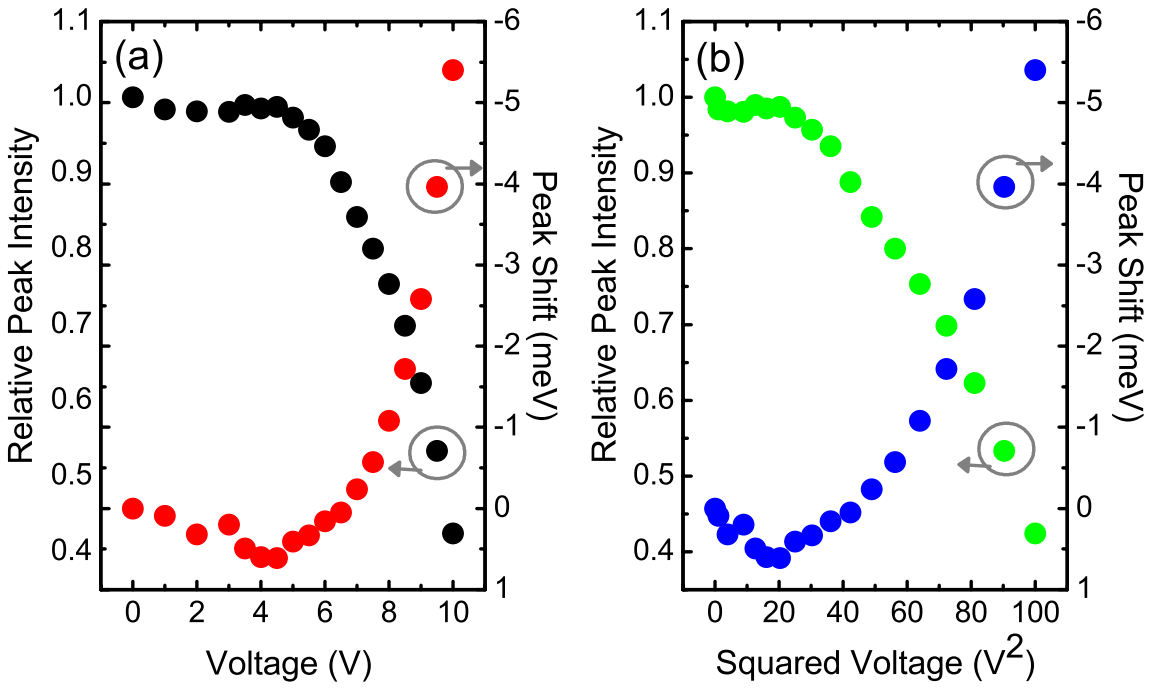


Figure 8.6: (a) Plots of relative peak intensity (black circles) and peak shift (red circles) as a function of applied voltage for the μ-PL spectra shown in Figure 8.4(b). (b) Plots of relative peak intensity (green circles) and peak shift (blue circles) as a function of the square of applied voltage for the μ-PL spectra shown in Figure 8.4(b).

a reduction of the oscillator strength because of the decreased electron-hole wavefunction overlap, causing the PL intensity to drop. Field-induced carrier tunnelling out of the QD also plays a role. Tunnelling is expected to cause linewidth broadening, and this is clearly seen in Figure 8.4(b) as the applied voltage increases.

The increase in the linewidth $\Delta\Gamma$ induced by applied electric field F can be described by the expression (5)

$$\Delta\Gamma = \frac{\pi\hbar^2}{2m^*a^2}\exp\left(-\frac{4\sqrt{2m^*}}{3\hbar}\frac{V_0^{3/2}}{eF}\right), \tag{8.1}$$

where a is the *characteristic dimension* of the QD; V_0 is the energy offset between the ground state of the electron in the QD and the lateral barrier; and m^* is the reduced electron mass, which may be estimated by assuming an indium content of 20% (9) and performing a linear

interpolation between the values of m^* for GaN ($0.20m_e$) and for InN ($0.07m_e$) (10), giving $0.174m_e$. Tunnelling of holes is neglected because the rate will be much less than for electrons due to their larger effective mass.

Figure 8.7(a) shows a plot of linewidth against calculated electric field strength for the QD shown in Figure 8.4. This plot was fitted with Equation 8.1, giving a *characteristic dimension*, a, of 2.1 nm. This value is a reasonable fit to average QD dimensions, as measured using AFM (9) (discussed in Section 2.3.4). The energy offset V_0 between the ground state of the electron and the lateral barrier was found from the same fit to be 9.5 meV. Such a shallow confinement potential is consistent with the nature of the QDs in this sample, which are believed to be indium-rich islands on a damaged two-dimensional layer.

It is known that applying an external electric field F to a single QD is expected to produce a shift $\Delta E(F)$ in the exciton recombination energy which consists of both linear and quadratic terms (4; 6). The shift may be expressed as

$$\Delta E(F) = \mu F - \alpha F^2, \tag{8.2}$$

where μ and α are respectively the components of the permanent dipole moment and of the polarizability in the direction of the electric field. Previous studies of the effect of lateral electric fields on GaAs QDs (1) and CdSe QDs (4; 6) have shown a purely quadratic dependence of the QCSE shift on field strength, with any linear contribution being negligible. This is because the lateral component of the permanent dipole moment is very small in both systems.

However, this is found not to be the case for the QDs in Sample B. Figure 8.6(b) plots the peak intensity and peak shift against the *square* of the applied voltage. A purely quadratic

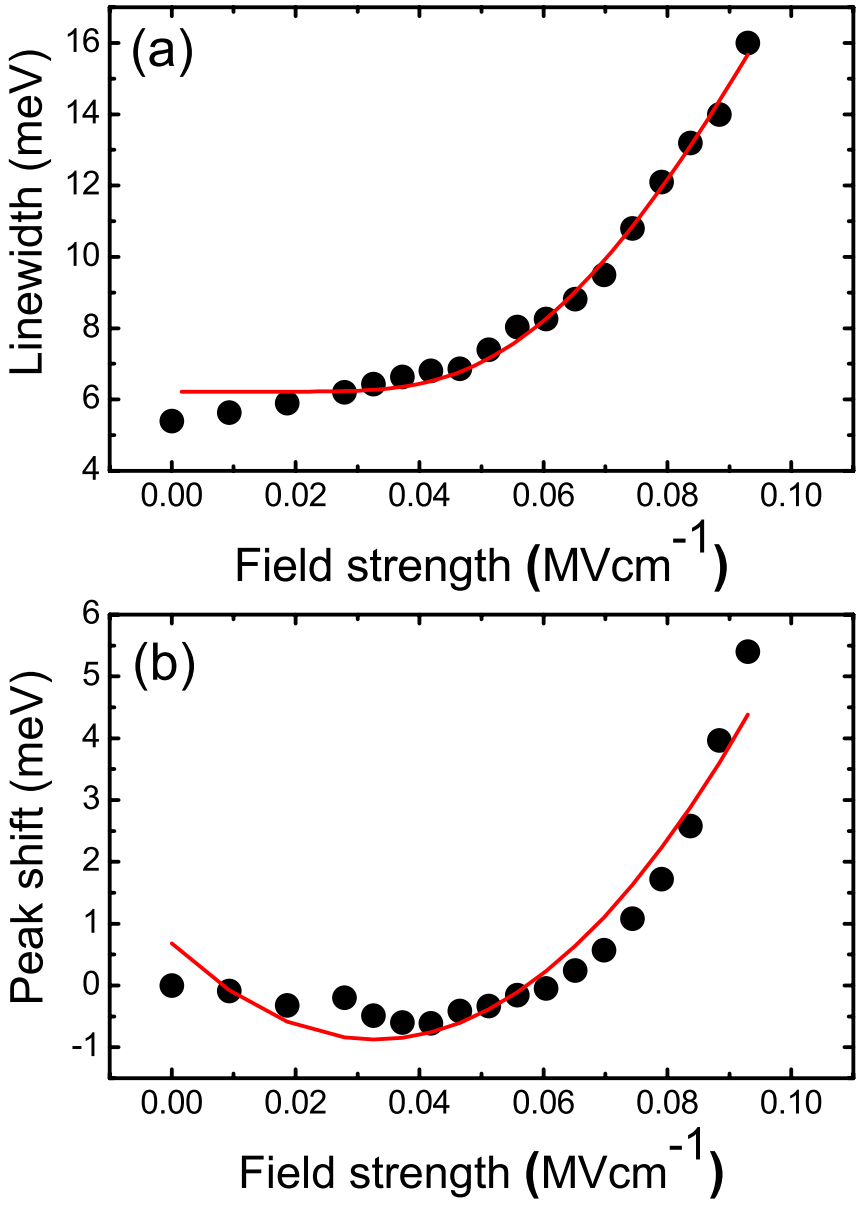


Figure 8.7: Plots of (a) linewidth and (b) peak shift (relative to the zero-field position) against calculated electric field strength for the QD shown in Figure 8.4. The solid red lines show the results of fitting (a) Equation 8.1 and (b) Equation 8.2.

relationship between the electric field strength and peak shift (resulting from the component of the dipole moment in the lateral direction being equal to zero) would produce a straight line trace on these axes. However, Figure 8.6(b) does not show a straight line trace. This indicates that a significant linear contribution to the QCSE shift (as defined by Equation 8.2) is present, suggesting that the permanent dipole moment in InGaN has a significant lateral component. This is quantified in Figure 8.7(b), which shows a plot of peak shift against calculated electric field strength for the InGaN QD in Figure 8.4. A fit was made to the plot using Equation 8.2, yielding a value of μ = -1.5×10^{-28} Cm for the lateral component of the permanent dipole moment.

8.6 Summary and conclusion

Electrical contacts on the surface of Sample B were prepared in order to allow the application of a lateral electric field of up to $\sim$ 0.17 MVcm^{-1} to single QDs. As found previously in other systems, increasing electric field resulted in a red-shift of the QD exciton recombination peak and a reduction in its intensity. Both these effects can be explained by the QCSE. Local ohmic heating effects and spectral diffusion contributions were ruled out. Quantitative considerations of linewidth broadening related to carrier tunnelling suggested that the QD under study had a *characteristic dimension* of 2.1 nm, and that the energy offset between the ground state of the electron and the lateral barrier was 9.5 meV. Further calculations involving the magnitude of the shift of the exciton recombination peak as a function of applied voltage showed that the value of the lateral component of the permanent dipole moment was μ = -1.5×10^{-28} Cm. This was in contrast to other QD systems, for which the lateral component of the permanent dipole moment was found by other workers to be

negligible.

References

[1] W. Heller, U. Bockelmann and G. Abstreiter, *Phys. Rev. B.* **57**, 6270 (1998).

[2] W. Heller, U. Bockelmann and G. Abstreiter, *Physica E* **2**, 623 (1998).

[3] S. Raymond, J. P. Reynolds, J. L. Merz, S. Fafard, Y. Feng and S. Charbonneau, *Phys. Rev. B* **58**, 13415 (1998).

[4] J. Seufert, M. Obert, M. Scheibner, N. A. Gippius, G. Bacher, A. Forchel, T. Passow, K. Leonardi and D. Hommel, *Appl. Phys. Lett.* **79**, 1033 (2001).

[5] J. Seufert, M. Obert, M. Rambach, G. Bacher, A. Forchel, T. Passow, K. Leonardi and D. Hommel, *Physica E* **13**, 147 (2002).

[6] G. Bacher, H. Schömig, J. Seufert, M. Rambach, A. Forchel, A. A. Maksimov, V. D. Kulakovskii, T. Passow, D. Hommel, C. R. Becker and L. W. Molenkamp, *Phys. Stat. Sol. (b)* **229**, 415 (2002).

[7] D. G. Hasko (private communication).

[8] C. Buchheim, A. T. Winzer, R. Goldhahn, G. Gobsch, O. Ambacher, A. Link, M. Eickhoff and M. Stutzmann, *Thin Sol. Films* **450**, 155 (2004).

[9] R. A. Oliver, G. A. D. Briggs, M. J. Kappers, C. J. Humphreys, J. H. Rice, J. D. Smith and R. A. Taylor, *Appl. Phys. Lett.* **83**, 755 (2003).

[10] I. Vurgaftman and J. R. Meyer, *J. Appl. Phys.* **94**, 3675 (2003).

Chapter 9

Conclusion and suggestions for further research

9.1 Implications for quantum information processing

This research described in this thesis has made several advances in understanding the potential of InGaN QDs for use in QIP.

The exciton recombination lifetime T_1 of single self-assembled epitaxially-grown InGaN QDs has been measured, as discussed in Chapter 5, and has been found to be long ($\sim$1–2 ns) compared to the duration of the ultrafast ($\sim$100 fs) laser pulses which would be used for gating operations in QIP. However, the lower limit which it has so far been possible to place on the exciton decoherence time T_2 (as inferred *indirectly* from linewidth measurements) has been found to be relatively short ($T_2 \geq$5 ps). If the decoherence time were really as short as $\sim$5 ps, this would give only a ratio of $\sim$50 of decoherence time to clock time, far from the $\sim 10^4 - 10^5$ ratio which is known to be required for successful implementation of QIP (as discussed in Chapter 4). However, the effect of spectral diffusion, discussed in Chapter 5,

may in fact be responsible for broadening the observed linewidths of the QD transitions. Thus it is possible that the decoherence time may in fact be much longer than ∼5 ps. A *direct* measurement of T_2 is required in order to determine whether this is the case. Thus a full assessment of the potential for using self-assembled InGaN QDs in QIP depends on the outcome of a direct measurement of the decoherence time T_2.

Measurements on single pyramidal, selectively-grown InGaN QDs (Chapter 6) demonstrated a high degree of coupling between the QDs and the WL, resulting in a much shorter exciton recombination lifetime (T_1 ∼0.4 ns) than in self-assembled InGaN QDs. Thus it appears that QDs of this type are unlikely to be of use in QIP since the increased QD–environment interaction may well result in an even shorter value of T_2 than for self-assembled QDs, although a direct measurement of T_2 is still required.

Time-integrated and time-resolved experiments on single self-assembled InGaN QDs at high excitation power densities (Chapter 7) were used to demonstrate the presence of biexciton states, which may have implications for the realization of simple biexciton-based quantum logic gates, such as that recently demonstrated in a GaAs QD (1). However, as discussed in Chapter 4, a quantum logic gate of this type is intrinsically unscalable to more qubits and researchers will need to consider other approaches if a large-scale quantum computer is to be constructed.

Finally, the use of externally-applied lateral electric fields to cause shifts in the exciton recombination energy (and emission intensity) of a self-assembled InGaN QD (Chapter 8) may have important QIP consequences, particularly for proposed schemes based on vertically-stacked pairs of QDs (discussed in more detail in Chapter 4). It may be possible to use the external electric field to shift the exciton transition energy in one QD into and out of

resonance with the transition energy in the other.

9.2 Further research

9.2.1 Quantum correlation spectroscopy

Since the single exciton and ground state levels in a QD constitute a two-level quantum system, it is expected that light emission from a single QD will display certain characteristic properties. In particular, if a photon is emitted at time $\tau = 0$, then it will not be possible for the QD to emit a second photon immediately afterwards as it is then necessarily in the ground state. The next photon can only be emitted after a certain waiting time. This 'dead time' between photon emission events means that the emitted light is statistically 'sub-poissonian'.

Such sub-poissonian behaviour can be described as *photon anti-bunching*, since emission of photons in rapid sequence (or 'bunches') is suppressed. Experimentally, photon anti-bunching has been previously observed in the light emitted by single atoms (2), ions (3) and molecules (4; 5). Observing such an effect in a QD provides strong evidence that the QD really does behave as an 'artificial atom', and this was achieved for a CdSe QD in 2000 (6) and for an InAs QD in 2002 (7). However, photon anti-bunching has not so far been demonstrated in the emission from an InGaN QD. This would be a useful extension to the work presented in this thesis.

In order to demonstrate photon anti-bunching behaviour, it is common to use a Hanbury-Brown and Twiss (HBT) interferometer (8), shown schematically in Figure 9.1(a). Light

from the QD (collected under laser excitation by a μ-PL system in the usual way) is directed onto a non-polarizing beamsplitter, which splits it into two beams of equal intensity. Identical detectors are used to detect photons sent into the two arms of the interferometer. In a photon anti-bunching experiment, a timer is started when a photon strikes one of the detectors, and is stopped when a second photon strikes the other. An electronic circuit measures the delay between the signals from the two detectors. This process is repeated many times so that the number of events can be plotted against the relative delay time between the two photons.

The experiment may be performed two distinct modes. In the case of CW laser excitation of the QD, photon anti-bunching behaviour is manifested as a reduction in the number of coincidences near zero delay time. A symmetric dip appears near zero delay in a graph of the number of coincidences plotted against delay time (as shown in Figure 9.1(b)). In the second type of experiment, pulsed laser excitation is used. In this case, regular spikes appear in a plot of coincidences against delay, separated by the repetition time of the laser pulses. Anti-bunching behaviour is shown as a reduction in the magnitude of the zero-delay peak relative to the other peaks (as shown in Figure 9.1(c)).

The author constructed an HBT interferometer for the purpose of performing photon anti-bunching measurements on single self-assembled InGaN QDs. A photograph showing the complete set-up used for HBT experiments is shown in Figure 9.2. The interferometer used a pair of PMTs equivalent to that described in Section 3.6.3, together with the same *Becker & Hickl* 'SPC-630' TCSPC module (installed in the card slot of a PC) as that used for time-resolved measurements on single QDs. One of the detector connections was extended using an additional 2 m length of cable in order to shift the zero-delay position to the centre of the temporal window under observation. The interferometer was enclosed in a light-proof

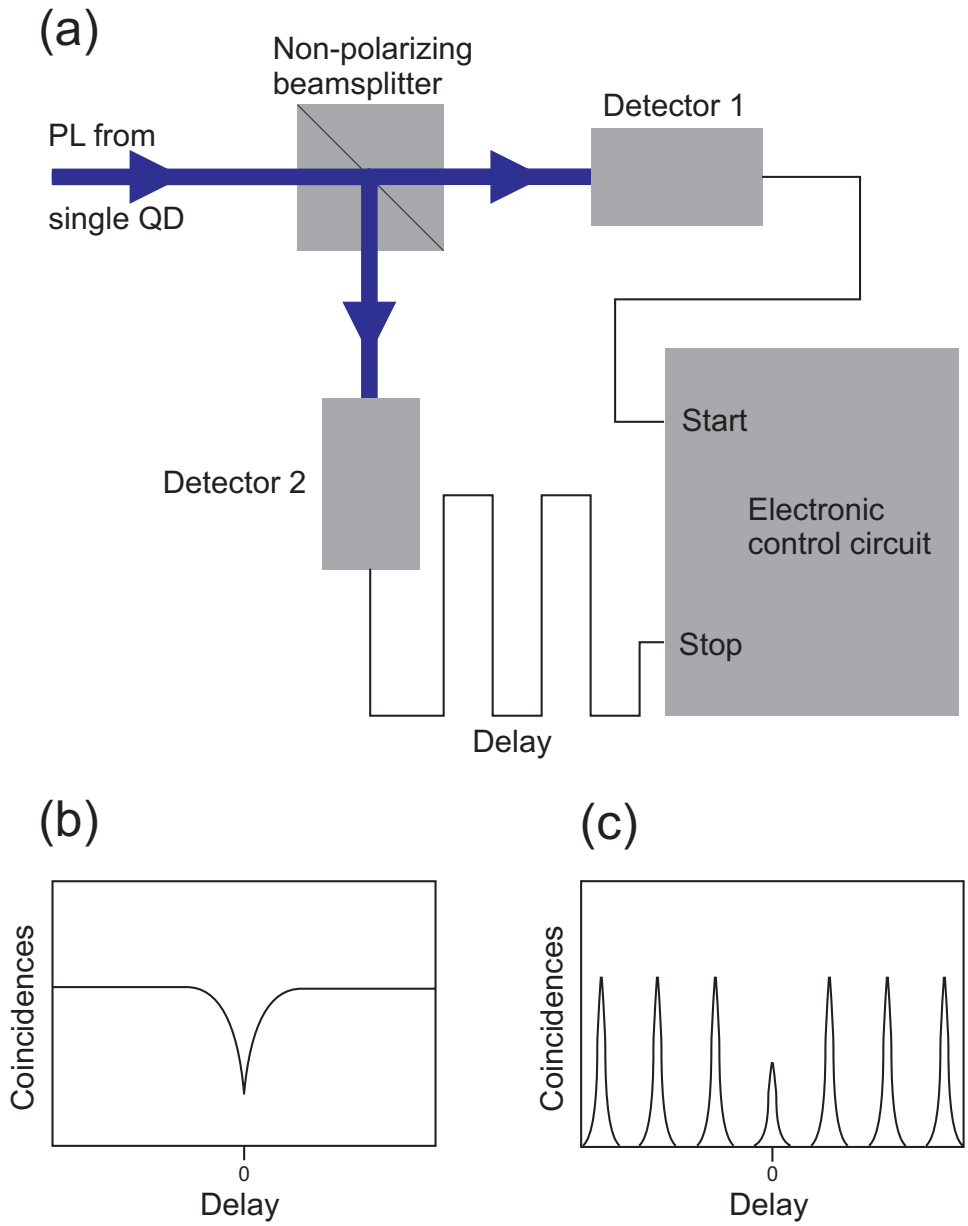


Figure 9.1: (a) A schematic diagram of the experimental arrangement used for performing the Hanbury-Brown Twiss experiment. Light incident on a beamsplitter is split into equal-intensity beams which pass down the two arms of the interferometer to two identical detectors. An electronic circuit starts a timer when a photon is incident on Detector 1, and stops it when a photon is incident on Detector 2. An additional length of cable may be inserted between one of the detectors and the counting circuit in order to move the zero-delay position to the centre of the temporal window. (b) Under CW excitation, photon anti-bunching behaviour is manifested as a dip in the number of coincidences near zero delay. (c) Under pulsed excitation, photon anti-bunching is manifested as a reduction in the magnitude of the zero-delay coincidence peak.

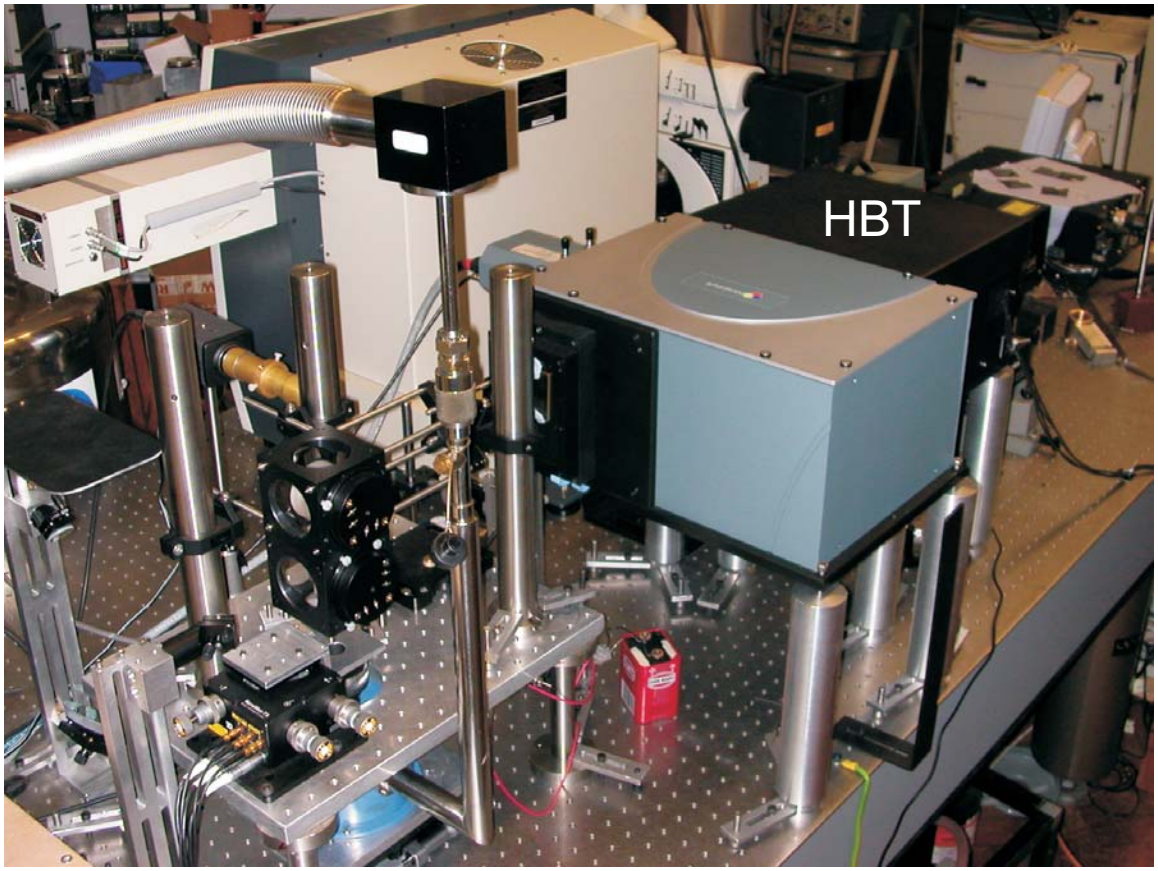


Figure 9.2: A photograph of the apparatus used for performing the Hanbury-Brown Twiss experiment. The high-resolution μ-PL system used for collecting light from the QD is seen on the left. The light then passed into the *Shamrock* spectrometer (the blue box) which was used to select the wavelength to be sent to the HBT interferometer (the black box behind the *Shamrock*). The interferometer consisted of a non-polarizing beamsplitter cube and a pair of identical PMTs controlled by a PC.

black box, sealed against the exit slit of the *Shamrock* spectrometer.

Unfortunately, it did not prove possible during the course of this work to successfully demonstrate photon anti-bunching behaviour in single InGaN QDs, since (as was eventually established) periodic intensity fluctuations associated with the multi-mode behaviour of the He-Cd laser used for CW excitation completely swamped the expected dip at zero delay time. The work should therefore be repeated using a truly CW (single-mode) laser for excitation, or in pulsed mode with a pulsed source (such as a Ti:Sapphire laser).

9.2.2 Principles of coherent control

It is clear from Section 9.1 that a means of directly measuring the decoherence time T_2 of excitons in single QDs is required in order to fully evaluate the suitability of self-assembled and selectively-grown InGaN QDs for QIP applications. One way of performing such a measurement is by using *coherent control* techniques.

Coherent control of carriers relies upon the fact that the effect of a sequence of light pulses on an optical transition varies strongly with the relative phase of the pulses, provided that the excited system stays coherent for a sufficiently long time. Consider a pair of identical laser pulses with a variable temporal separation which are incident on a semiconductor sample. The first pulse in the pair will create excitons with a well-defined phase, and the second pulse will either enhance or destroy these excitons (for constructive or destructive interference, respectively), according to the phase. The extent to which the excitons created by the first pulse are enhanced or destroyed by the second provides information about the extent to which the system has remained coherent during the interval between the pulses. This allows a value for the decoherence time to be deduced.

In 1995, investigations involving pairs of phase-locked ultrafast laser pulses with variable temporal separation incident upon GaAs QWs were reported (9). Coherent control of carrier dynamics was demonstrated and the decoherence of the system was studied. These early reflectivity-based measurements were followed in 1997 by experimental work based on direct measurements of PL intensity in GaAs QWs (10). In 1998, coherent control of a GaAs QD was demonstrated (11), permitting direct measurement of the exciton decoherence time. However, coherent control techniques have not yet been used to investigate InGaN QDs.

9.2.3 Experimental implementation of coherent control

A typical means of generating pairs of identical optical pulses with a well-defined and variable temporal separation is to pass single laser pulses through a Mach-Zehnder interferometer. Consider a pulse entering such a device. The pulse is divided into two equal-intensity components by a beamsplitter, and these pass down the two arms of the interferometer. If the optical path lengths traversed by the light in the two arms of the interferometer are slightly different, then a small delay will be induced for light passing down one arm compared to light in the other arm. When the two components are recombined and exit the interferometer, the original single pulse has been converted into a pair of pulses with a fixed temporal separation.

It is possible to achieve a variable delay by slightly altering the length of one of the arms, for example by mounting the mirror or retro-reflector which defines its endpoint on a micrometer-controlled translation stage.

Since even small changes in the relative optical path lengths of the two arms will affect the temporal separation of the two pulses, the interferometer will be highly sensitive to vibrations. This means that, in practice, it must be *stabilized* so that the relative path lengths of the two arms do not change except when desired by the experimenter.

The author constructed an *actively-stabilized* Mach-Zehnder interferometer for use in future coherent control experiments on single InGaN QDs. The system was built according to a design developed by Dr Andrew Ramsey (who at the time was working at the University of Cambridge) (12). Dr Ramsey's interferometer was itself based on the design of an earlier device used in pioneering coherent control experiments (9).

The author's interferometer was actively stabilized using interference fringes formed by a CW He-Ne laser. The optical layout of the device is shown schematically in Figure 9.3, and a photograph is shown in Figure 9.4. Photodiodes were used to sample the intensity of the He-Ne fringe pattern at two points, and the signals were sent to a PC. Any disturbance to the system caused by vibrations would change the fringe pattern, and the PC would calculate and apply a correction so that the path difference between the two arms of the interferometer remained 'locked'.

We shall now consider the operation of the active stabilization mechanism in more detail. Ignoring for the moment the high-power pulsed beam (shown in blue), consider only the low-intensity CW He-Ne beam used for stabilization. The He-Ne laser which was chosen was a fixed-polarization device (such that the direction of the plane of polarization did not change with time). A half waveplate was used to rotate the direction of polarization of the beam such that, when it was incident on the polarizing beamsplitter, equal intensities (with orthogonal polarizations) passed down the two arms of the interferometer. One arm contained a retro-reflector mounted on a micrometer translation stage (for coarse control of the delay), while the other contained a mirror mounted on a piezoelectric transducer (for active stabilization and for fine control of the delay). The beams from the two arms were recombined at a second beamsplitter.

A quarter waveplate oriented at 45° converted the two linearly-polarized recombined light beams to circularly-polarized, allowing the beams from the two arms of the interferometer to interfere. A fringe pattern was generated using a linear polarizer, and was expanded with a lens. The fringe pattern was sampled by two of the four sections of a quadrant photodiode, separated by ∼1 mm (using a quadrant photodiode rather than two separate photodiodes

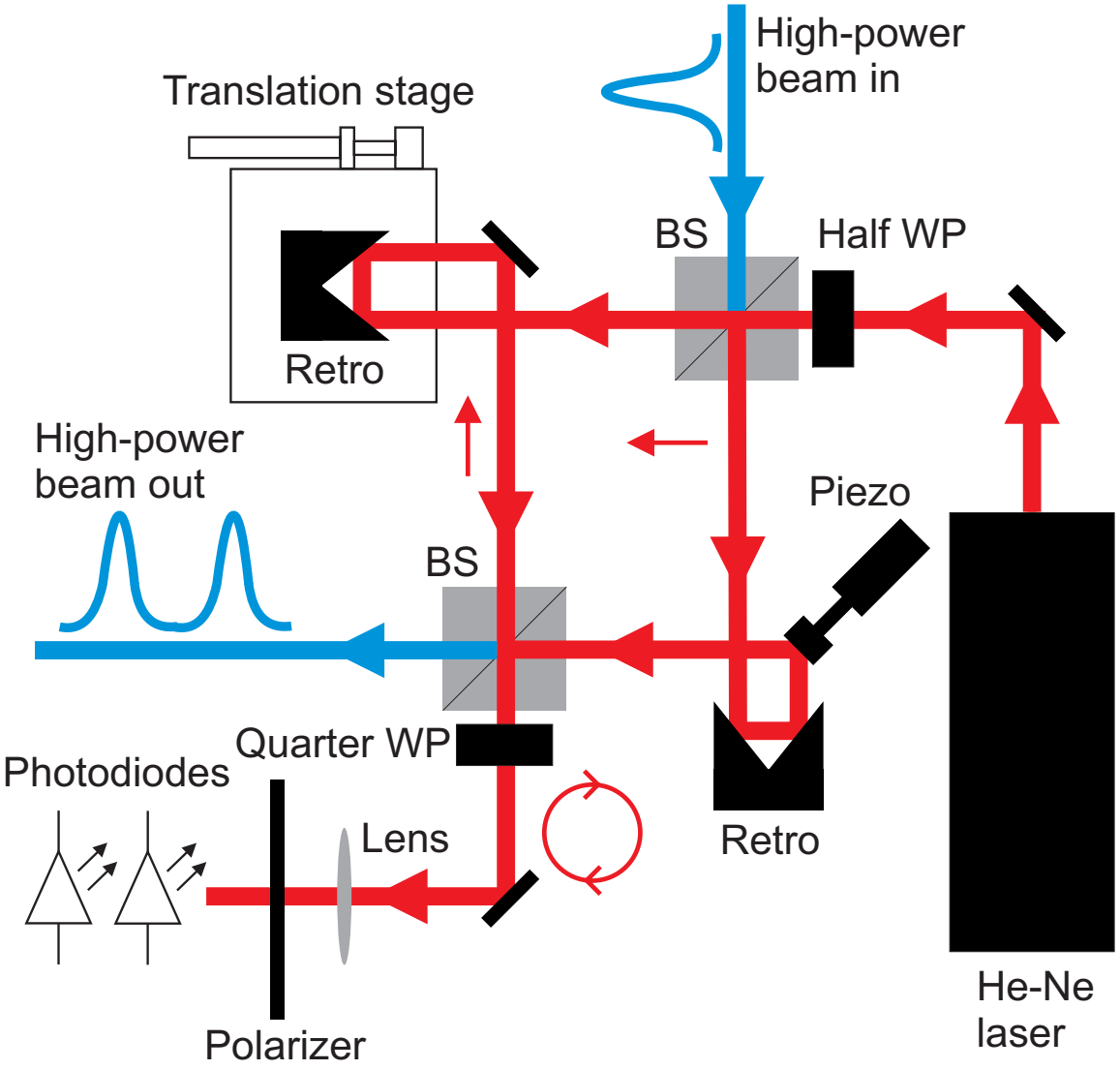


Figure 9.3: A schematic diagram of the actively-stabilized Mach-Zehnder interferometer which was constructed for future coherent control measurements. The system shows the waveplates (WP), beamsplitters (BS) and retro-reflectors. A low-power CW He-Ne beam generated a fringe pattern which was sampled by two photodiodes. Vibrations caused changes in the fringe pattern, allowing the PC to calculate and apply a correction to stabilize the interferometer. The high-power pulsed beam entered the interferometer at right-angles to the He-Ne beam.

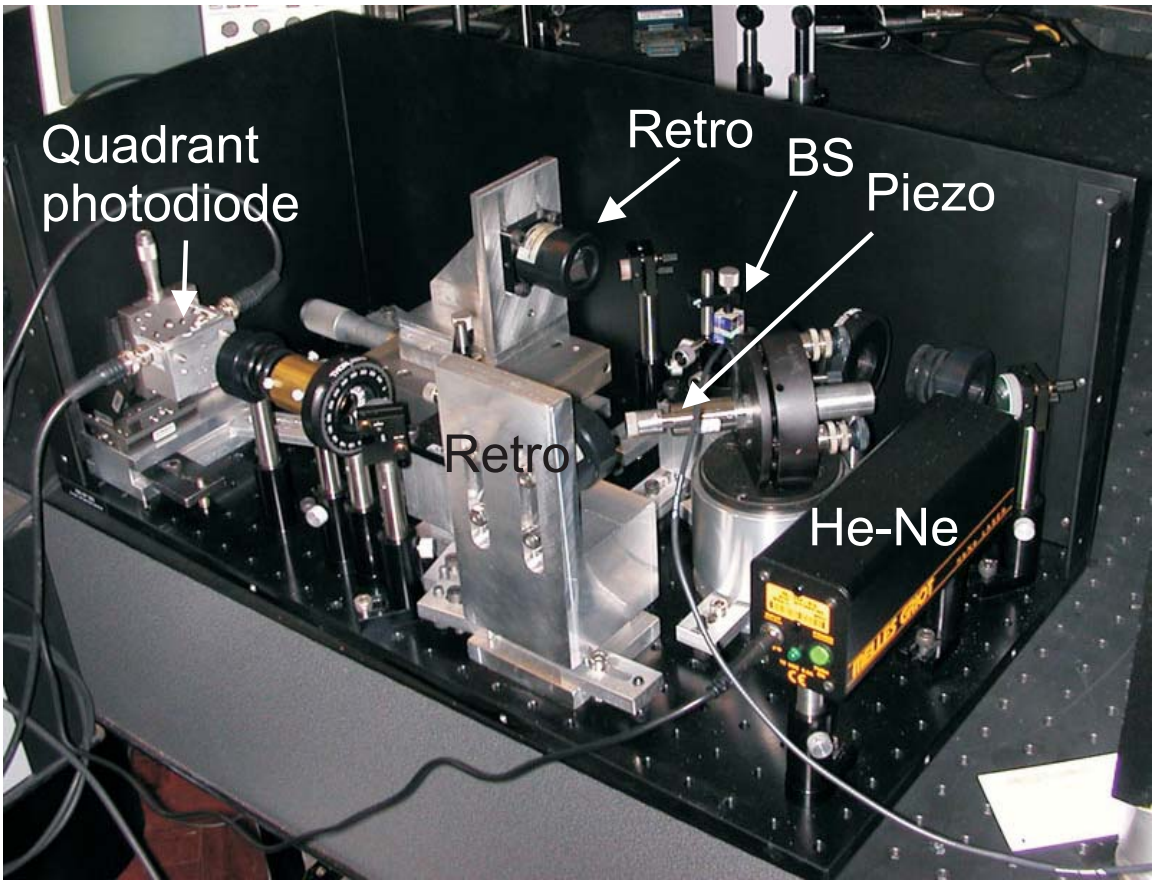


Figure 9.4: A photograph of the actively-stabilized Mach-Zehnder interferometer constructed by the author for coherent control measurements. In this view, one of the two L-shaped side panels and the lid (used to protect the interferometer from air currents) have been removed so that the optical layout can be seen. The He-Ne laser is seen on the right. One of the two beamsplitters (BS) can be seen and both of the retro-reflectors (one of them mounted on a micrometer-controlled translation stage) are visible. The piezo-mounted mirror (used for actively stabilizing the system) is seen in the centre. The quadrant photodiode (located behind a metal mask) used for sampling the He-Ne fringe pattern is seen to the left on its *xyz* translation stage mounting. The two BNC cables carry the photodiode signals to the electronics.

provided improved mechanical stability). A metal mask was placed in front of the photodiode to ensure that only the desired quadrants were illuminated.

The signals from the two illuminated photodiode quadrants were directed to the readout electronics. These were constructed by the author in accordance with circuit diagrams provided by Dr Andrew Ramsey. The electronics converted the photodiode outputs from current to voltage, filtered out high frequencies (since these could not be corrected by the active stabilization system) and then routed the signals to the PC.

The PC was equipped with a dedicated slot-in card to control the interferometer. This was a *Microstar Laboratories* Data Acquisition Processor 'DAP3216a', based on a 486DX processor. The DAP card ran a programme written by Dr Andrew Ramsey, which calculated the feedback signal required to correct for deviations of the system caused by vibrations and sent a correction signal to drive the piezo-electric mirror mount.

The user could control the active stabilization system via a user interface programme (also written by Dr Andrew Ramsey) running on the PC , based on HP-VEE 4.01 software. The feedback could be turned on and off, and the user could specify the PID parameters in order to optimize the interferometer performance. The DAP card sent output to the user interface allowing the quality of stabilization to be monitored, as the excursions of the system from perfect stability were continuously plotted in real time.

In tests, the active stabilization system was found to be able to keep the system 'locked' for indefinite periods, to better than $0.05\lambda_{\mathrm{HeNe}}$ (full width of excursions) under normal operating conditions.

Although no experiments were actually carried out using the interferometer, for coherent

control experiments a high-power pulsed beam (from a Ti:Sapphire laser) would enter the interferometer at right angles to the He-Ne beam (as shown in Figure 9.3), and also exit at right-angles to the He-Ne beam. The stabilization system would dramatically reduce fluctuations in relative path length caused by vibrations. Moreover, in addition to the coarse control of delay offered by the micrometer translation stage, fine control could be achieved using the piezo-mounted mirror. The user interface for controlling the active stabilization system allowed the user to make precisely-controlled changes (as fractions of an He-Ne laser interference fringe) to the optical path difference between the two arms.

It is intended that future experimental work will make use of the interferometer for coherent control measurements. The response of a single InGaN QD to pairs of closely-spaced laser pulses will be monitored as a function of the temporal delay between the two pulses in each pair. This will allow definite values for T_2 to be experimentally deduced.

References

[1] X. Li, Y. Wu, D. Steel, D. Gammon, T. H. Stievater, D. S. Katzer, D. Park, C. Piermarocchi and L. J. Sham, *Science* **301**, 809 (2003).

[2] H. J. Kimble, M. Dagenais and L. Mandel, *Phys. Rev. Lett.* **39**, 691 (1977).

[3] F. Diedrich and H. Walther, *Phys. Rev. Lett.* **58**, 203 (1987).

[4] Th. Basché, W. E. Moerner, M. Orrit and H. Talon, *Phys. Rev. Lett.* **69**, 1516 (1992).

[5] L. Fleury, J.-M. Segura, G. Zumofen, B. Hecht and U. P. Wild, *Phys. Rev. Lett.* **84**, 1148 (2000).

[6] P. Michler, A. Imamoğlu, M. D. Mason, P. J. Carson, G. F. Strouse and S. K. Buratto, *Nature* **406**, 968 (2000).

[7] V. Zwiller, P. Jonsson, H. Blom, S. Jeppesen, M.-E. Pistol, L. Samuelson, A. A. Katznelson, E. Yu. Kotelnikov, V. Evtikhiev and G. Björk, *Phys. Rev. A* **66**, 053814 (2002).

[8] R. Hanbury-Brown and R. Q. Twiss, *Nature* **179**, 27 (1956).

[9] A. P. Heberle, J. J. Baumberg and K. Köhler, *Phys. Rev. Lett.* **75**, 2598 (1995).

[10] X. Marie, P. Le Jeune, T. Amand, M. Brousseau, J. Barrau, M. Paillard and R. Planel, *Phys. Rev. Lett.* **79**, 3222 (1997).

[11] N. H. Bonadeo, J. Erland, D. Gammon, D. Park, D. S. Katzer and D. G. Steel, *Science* **282**, 1473 (1998).

[12] A. Ramsey, PhD Thesis, University of Cambridge (2003).

Appendix A

First Matlab programme

This appendix contains the text of the MATLAB programme DIFFUSION which was used to automatically calculate the spectral position, intensity and FWHM of an exciton recombination peak in a series of consecutively-recorded μ-PL spectra. Lines of text following the '%' symbol are comments which are not part of the programme. These have been shown in blue for clarity.

This programme was written by the author.

```
%calculates peak position, intensity and FWHM; uses smoothing

data=0;                     %"data" is a single row array which
contains all the data as read from the file
d=0;                        %"d" is an array with the same dimensions
as the data in the original file
peakheight=0;               %"peakheight" is an integer which keeps
track of the maximum signal across the window
peakpixelposition=0;        %"peakpixelposition" is an integer which
keeps track of the pixel position of the peak
results=0;                  %"results" is the matrix in which the
results of the calculation are stored
guessposition=0;            %"guessposition" is the estimated
position of the peak
Ncol=301;                   %the number of columns in the original
data file
Nrow=1024;                  %the number of rows in the original
data file
cosmic=1000;                %the value above which any signal is
```

```
assumed to be a cosmic ray
File_N='C:Documents and Settings\Jim Robinson\My Documents\Physics\Data\
05jun03\05jun004.asc';      %the name of the file to be studied
fid=fopen(File_N,'rt');     %opens the file
data=fscanf(fid,'%32f');    %sets up "data" as a single row containing
all the data from the file

guessposition=input('Please enter estimated peak position, in pixels ');

for i=1:Nrow
   for j=1:Ncol
     d(i,j)=data(Ncol*(i-1)+j);    %sets up "d" as a matrix equivalent to the
original data file
     if d(i,j)> cosmic             %sets element to zero if it is
found to be a cosmic ray
       d(i,j)=0;
     end
   end
end


%start of smoothing routine

for i=3:1022           %this part carries out 5-point smoothing of the
original data and stores results in the matrix "smoothed_d"
   for j=2:Ncol
     smoothed_d(i,j)=(d(i-2,j)+d(i-1,j)+d(i,j)+d(i+1,j)+d(i+2,j))/5;
%averages with the two adjacent points on each side
   end
end

for i=3:1022                        %this part feeds the results of
the smoothing operation back into the original matrix "d"
   for j=2:Ncol                      %it therefore ensures that the
matrix used in the next part has the correct dimensions
     d(i,j)=smoothed_d(i,j);
   end
end
```

```
%end of smoothing routine


for j=2:Ncol
peakpixelposition=0;                %resets the pixel position marker
to zero
peakheight=0;                       %resets the peak height marker
to zero

summation=0;                        %this routine calculates
a baseline based on the average across the top hat function
for n=380:580
   summation=summation+d(n,j);
end
   for i=guessposition-15:guessposition+15
     if d(i,j)> peakheight      %determines the position of the peak
       peakheight=d(i,j);
       peakpixelposition=i;
     end
   end

   results(j-1,1)=j-1;                      %sets the marker counter
in the matrix "results"
   results(j-1,2)=peakpixelposition;        %stores the peak position
result at the appropriate place in the matrix "results"
   results(j-1,3)=peakheight;               %stores the peak height
at the appropriate place in the matrix "results"


   absheight=(peakheight-summation/201);
   sqdiff=10^6;
   for i=peakpixelposition:peakpixelposition+15   %calculates the
1st half width in a range within 15 pixels of the peak (positive)
     if (d(i,j)-summation/201-absheight/2)^2 < sqdiff
       sqdiff=(d(i,j)-summation/201-absheight/2)^2;
       halfwidth1=i-peakpixelposition;
     end
   end
```

```
   sqdiff=10^6;
   for i=peakpixelposition-15:peakpixelposition   %calculates the
2nd half width in a range within 15 pixels of the peak (negative)
     if (d(i,j)-summation/201-absheight/2)^2 < sqdiff
       sqdiff=(d(i,j)-summation/201-absheight/2)^2;
       halfwidth2=peakpixelposition-i;
     end
   end

   results(j-1,4)=halfwidth1+halfwidth2;

   guessposition=peakpixelposition;   %uses the previous peak
position as the new guess for the peak position
end


save output05jun004peak1fwhm results -ascii          %writes the
matrix "results" to the ASCII file "output"
```

Appendix B

Second Matlab programme

This appendix contains the text of the MATLAB programme CORRELATE which was used to calculate the autocorrelation function. This programme was used to determine whether there was any periodicity in the temporal fluctuations in the peak position and FWHM caused by spectral diffusion. Lines of text following the '%' symbol are comments which are not part of the programme. These have been shown in blue for clarity.

This programme was written by the author.

```
%calculates the autocorrelation function; "diffusion" must be
run first

smoothresults=0;
scaledresults=0;
resultscorr=0;

for e=1:Ncol-21                              %this part carries out
smoothing using 21-point averaging
   twonepoint=0;
   for f=e:e+20
     twonepoint=twonepoint+results(f,2);  %uses matrix "results"
as calculated by the programme "diffusion";
   end                                        %therefore, "diffusion"
must be run first
   smoothresults(e+10,1)=e+10;
   smoothresults(e+10,2)=twonepoint/21;
end
```

```
save smoothed10jun002 smoothresults -ascii %saves the smoothed
curve to the file "smoothed"


for g=11:Ncol-11
    scaledresults(g,1)=g;  %subtract line of best fit from smoothed
curve
  scaledresults(g,2)=smoothresults(g,2)-3.18244*g+0.07382*g^2-6.55925
*10^-4*g^3+2.49326*10^-6*g^4-3.381*10^-9*g^5;
end                        %line of best fit calculated using Origin:
must be entered manually each time

save scaled10jun002 scaledresults -ascii  %saves the scaled
smoothed curve to the file "scaled"

delta_t=0;
correlation=0;
counter=0;
traceone=0;
tracetwo=0;
resultscorr=0;

for delta_t=0:5*Ncol/6-11   %calculates the correlation over
the specified range of delta_t
    correlation=0;

    for counter=11:Ncol/6
      traceone=scaledresults(counter,2);
      tracetwo=scaledresults(counter+delta_t,2);
      correlation=correlation+traceone*tracetwo;
    end

    resultscorr(delta_t+1,1)=delta_t;
    resultscorr(delta_t+1,2)=correlation;

end

save resultscorr10jun002 resultscorr -ascii   %saves the
correlation results to file
```